Measurements of impurity concentrations and transport in the Lithium Tokamak Experiment

Dennis Patrick Boyle

A Dissertation
Presented to the Faculty
of Princeton University
in Candidacy for the Degree
of Doctor of Philosophy

Recommended for Acceptance
by the Department of Astrophysical Sciences
Program in Plasma Physics
Advisers: Robert Kaita and Richard Majeski

September 2016

Abstract

This thesis presents new measurements of core impurity concentrations and transport in plasmas with lithium coatings on all-metal plasma facing components (PFCs) in the Lithium Tokamak Experiment (LTX). LTX is a modest-sized spherical tokamak uniquely capable of operating with large area solid and/or liquid lithium coatings essentially surrounding the entire plasma (as opposed to just the divertor or limiter region in other devices).

Lithium (Li) wall-coatings have improved plasma performance and confinement in several tokamaks with carbon (C) PFCs, including the National Spherical Torus Experiment (NSTX). In NSTX, contamination of the core plasma with Li impurities was very low ($< 0.1\%$) despite extensive divertor coatings. Low Li levels in NSTX were found to be largely due to neoclassical forces from the high level of C impurities. Studying impurity levels and transport with Li coatings on stainless steel surfaces in LTX is relevant to future devices (including future enhancements to NSTX-Upgrade) with all-metal PFCs.

The new measurements in this thesis were enabled by a refurbished Thomson scattering system and improved impurity spectroscopy, primarily using a novel visible spectrometer monitoring several Li, C, and oxygen (O) emission lines. A simple model was used to account for impurities in unmeasured charge states, assuming constant density in the plasma core and constant concentration in the edge. In discharges with solid Li coatings, volume averaged impurity concentrations were low but non-negligible, with $\sim 2 - 4\%$ Li, $\sim 0.6 - 2\%$ C, $\sim 0.4 - 0.7\%$ O, and $Z_{eff} < 1.2$.

Transport was assessed using the TRANSP, NCLASS, and MIST codes. Collisions with the main H ions dominated the neoclassical impurity transport, unlike in NSTX, where collisions with C dominated. Furthermore, neoclassical transport coefficients calculated with NCLASS were similar across all impurity species and differed no more than a factor of two, in contrast to NSTX where they differed by an order of

magnitude. However, time-independent simulations with MIST indicated that unlike NSTX, neoclassical theory did not fully capture the impurity transport and anomalous transport likely played a significant role in determining impurity profiles.

Acknowledgements

This dissertation would not have been possible without support from many people over the years. It would take an entire additional dissertation to properly acknowledge everyone and their contributions, but please know I am forever grateful for all you have taught me, done for me, and shared with me.

Thank you to my formal and informal advisers, Bob Kaita, Dick Majeski, Ron Bell, Filippo Scotti, and Rajesh Maingi; fellow LTX graduate students and postdocs, Matt Lucia, Craig Jacobson, John Schmitt, Dan Lundberg, Laura Berzak-Hopkins, Erik Granstedt, Jack Hare; the LTX technical and engineering staff, Jim Taylor, Tom Kozub, and Enrique Merino; graduate program administrators Beth Leman and Barbara Sarfaty; collaborators Chris Hansen, Shige Kubota, Ted Biewer, Travis Gray, Kevin Tritz, Joel Clementson, Peter Beiersdorfer, Klaus Widmann, and Jaan Lepson; PPPL staff Ben LeBlanc, Greg Tchilinguirian, Tommy Holoman, Dave Moser, and John Trafalski; advisers and colleagues on past projects, Mike Mauel, Darren Garnier, and the LDX team; my NUF advisor Charles Skinner and everyone in Science Ed; Thomas Pedersen and the CNT graduate students at Columbia; my professors, teachers, and teaching assistants throughout my education; other friends at PPPL, fellow graduate students, the Tokabats softball team, my officemate Vasily Geyko, and my high school and college friends.

Finally, thank you to my family, Mom and Ed, Dad, my grandparents, my uncles, aunts, cousins, and in-laws, and most of all, my wonderful wife Joelle and our daughter Clara.

To my wife, Joelle.

Contents

List of Figures

Chapter 1

Introduction

The ultimate purpose of this work is to make incremental but important progress towards understanding a modest-sized experiment that explores a less mainstream but potentially revolutionary approach to solving a crucial problem in the development of practical nuclear fusion energy. This first chapter will discuss the need for additional energy sources and advantages of fusion, and present background on how the basic fusion reaction works, how fusion reactors can confine million degree plasmas to harness this energy, and the fundamental challenges that must be overcome. This chapter will continue with a brief introduction to the specific issue of selecting and engineering the materials in a reactor to meet the extremely demanding challenge of withstanding a thermonuclear fusion plasma, and highlight certain advantages of using a liquid metal to enable robust, novel solutions to these challenges. As understanding impurity behavior motivates much of this work, this chapter will discuss more specifically how these materials can contaminate the plasma and the various issues of how impurities can affect the fusion plasma. The use of lithium as a first wall material will also be discussed. Lithium can address many material issues as a liquid metal, and due to its unique place in the periodic table, potentially both reduce harmful effects of impurities and improve plasma confinement. Finally, this

chapter will lay out the objectives of this work in understanding impurity transport with lithium coatings in an all-metal wall tokamak.

Chapter 2 will provide background on the Lithium Tokamak Experiment, and the specific experiments performed there for this work, Chapter 3 will discuss the Thomson Scattering diagnostic used to measure electron density and temperature, Chapter 4 will discuss spectroscopic measurements of impurity density profiles, Chapter 5 will discuss and analyze an integrated plasma model of a repeated discharge, Chapter 6 will discuss and analyze impurity transport calculations, and Chapter 7 will summarize results and future work.

1.1 Fusion

1.1.1 Energy and the need for fusion

Energy has been and likely will continue to be a major factor in improving human well being [27, 28]. However, current energy sources all have significant limitations, especially for a future world with much higher energy consumption. Fossil fuels are limited by the need to greatly reduce or even eliminate pollutants, especially greenhouse gas emissions driving global climate change. Even with efficient pollution controls and carbon capture, global reserves face an ultimate limit. Hydroelectric and geothermal power are limited by geography, and can have significant local impacts. Tremendous strides have been made in making solar and wind power more affordable but even if intermittency issues can be solved, land use will remain an inherent limitation. Nuclear fission can provide baseload power without emitting greenhouse gases, but risks and fears of catastrophic accidents and nuclear weapons proliferation is generally making it unattractive, especially in light of high capital costs. Additionally, widespread future use will be limited by supplies of enrichable uranium and storage

of radioactive wastes without use of advanced fuel cycles (which generally increase proliferation risks).

Nuclear fusion energy is a potential solution to all of these problems, and likely to provide future societies with energy practically limitless by todays standards [27]. Its only fuels are the hydrogen found in seawater and lithium in the earths crust, and its only wastes would be inert helium gas and the reactor buildings themselves, which would have to be sealed off for a few decades after decommissioning because their structural materials would temporarily become moderately radioactive. With current reactor designs the plants would be no larger than present nuclear plants, with similar capital costs but no risks of weapons proliferation, or catastrophic meltdown and other accidents requiring evacuation and decontamination. Future designs could be much more compact and less expensive and enable revolutionary changes in energy use and our economy.

1.1.2 Nuclear fusion reactions

The principle of nuclear fusion is simple and well understood; it is what powers the sun and other stars and created all of the chemical elements beyond hydrogen that comprise us, our world, and the universe. Nuclear fusion occurs when two nuclei come together close enough to interact via the nuclear strong force and produce a new larger nucleus. For most fusion reactions producing nuclei lighter than iron, the reaction releases energy due to tighter overall nuclear binding of the fusion products. Because nuclear bonds are much stronger than chemical bonds, much more energy is released and a nuclear (fusion or fission) power plant would require much less fuel than an equivalent fossil fuel plant.

However, in order to bring nuclei close enough to fuse, the electric repulsion between their positive charges must be overcome by their kinetic energy. Generally this is achieved by heating the nuclei to millions of degrees, and then holding them in place

long enough to fuse. This is the main challenge of harnessing nuclear fusion energy, and why it has taken 50 years of research, and probably several more decades in the future to produce power commercially. Once fusion begins, the energy released can further heat the fuel, sustaining the reaction. At temperatures in which fusion can occur, the fuel becomes a plasma, an ionized gas in which neutral atoms are broken apart into electrically charged ions and electrons. Due to the high temperatures, as well as the inherent electrical nature of plasmas, temperatures are typically measured in electron-volts (eV), equal to 11,600 K.

The most widely considered fusion reaction for energy production uses the deuterium (D) and tritium (T) isotopes of hydrogen in the reaction $D + T \rightarrow He + n + 17.6$ MeV. Due to the relatively weak binding of the incoming tritium nucleus, and the tight binding of the outgoing helium nucleus (also known as an alpha particle), this reaction has a large energy gain. This is favorable in and of itself and also because it increases quantum tunneling through the repulsive barrier, which is already as low as possible as both nuclei are singly charged. Thus, D-T fusion has the largest fusion cross section and reactivity for temperatures less than ~ 400 keV [37].

Other fusion fuel cycles have advantages in not producing neutrons (which are unconfined by magnetic fields and thus carry energy out of the plasma and necessitate massive shielding of the reactor) and/or not requiring tritium (which is radioactive and thus both somewhat hazardous and not found in nature) but would require such a large improvement in plasma confinement that they are not presently feasible.

Fortunately, the neutron "problem" also provides a solution to the tritium problem, enabling breeding of tritium by nuclear fission of lithium through the reactions $^6Li + n \rightarrow T + He + 4.8$ MeV and $^7Li + n \rightarrow T + He + n - 2.5$ MeV, which also generate additional net power. To increase the breeding ratio such that each D-T

4

reaction produces more than one triton, neutron multipliers may be added, further increasing energy output. [1]

1.1.3   Nuclear fusion reactors

As stated previously, the major challenge of harnessing fusion energy is the difficulty of simultaneously heating a plasma to millions of degrees and confining it long enough for it to fuse. In stars, the initial heating and the confining force are produced by immense gravitational pressure. In a hydrogen bomb, x-rays from a nuclear fission primary heat the fuel and also compress it to such a high density that the chain reaction occurs before the fuel can blow itself apart. This concept, called inertial confinement fusion, is also being explored for energy generation using lasers, wires with large electric currents, or particle beams to heat and compress the fuel.

The most heavily researched method for creating fusion energy, with the best understood path to viability, is magnetic confinement fusion. This approach takes advantage of the electrically charged nature of the plasma state in which fusion occurs in order to confine and heat the fuel. Plasma ions and electrons are bound to magnetic field lines and even at the high energies in fusion plasmas will orbit them in tight spirals. The most developed magnetic configurations use toroidal magnetic fields so that the field lines circle infinitely without impacting a material surface.

Specifically, the most studied and successful magnetic configuration is the tokamak [106], which confines plasma in a mostly axisymmetric toroidal field, as well as a poloidal field generated by a toroidal current flowing in the plasma itself. The poloidal field stabilizes the plasma such that any vertical drifts are cancelled on average, while the current helps heat the plasma resistively. As plasmas get hotter, however,

---

[1]In fact, there are proposals to surround a fusion plant with fissionable fuel. Using the fusion plant as a neutron source allows a subcritical fission reactor without possibility of a runaway chain reaction causing a meltdown, and with the ability to burn up radioactive wastes to reduce storage/disposal issues. It could also be possible to reduce proliferation risks caused by enrichment and reprocessing. [51]

particles collide less and resistivity drops, meaning additional heating is needed to achieve fusion temperatures. The high energy alpha particles created in the fusion reaction itself can provide most or all of this heating power[2], but auxiliary heating methods are typically employed, primarily high-energy neutral beams and/or radio-frequency waves resonant with plasma ions and/or electrons. These methods can also help drive the plasma current, which can be created, but not indefinitely sustained, through induction by a central transformer.

1.1.4   Basic challenges of fusion energy

One of the main challenges in creating a viable fusion power plant is confining heat in the plasma long enough for the ions to undergo fusion. Confinement in tokamaks is largely understood, but many significant gaps remain. There is a known, irreducible level of heat transport caused by collisions between particles, as well as an enhancement of this transport caused by the curved toroidal and poloidal magnetic fields. These so-called neoclassical losses can be minimized by optimization of the magnetic fields, but are ultimately limited by magnet technology. Similarly, radiative losses from synchrotron and bremsstrahlung radiation are to some extent unavoidable and increase with temperature. Keeping out impurities can reduce radiative losses, especially line radiation from impurities. In practice, additional loss mechanisms often play a larger role. Macroinstabilities can cause large scale movements in the plasma fluid and rapid losses of large amounts of plasma energy. Avoiding macroinstabilities puts limits on the magnitude of plasma pressure and current, as well as their gradients. The above loss mechanisms are generally understood, though still areas of active research. In contrast, there is less complete understanding of microinstabilities

---

[2]While a self heated plasma is in a sense a chain reaction, it is generally not subject to the same type of runaway chain reaction possible in nuclear fission. It is typically run at peak reactivity, not just above the point at which the chain reaction can occur; increased output would degrade confinement and self-limit; it has minutes and grams worth of fuel, not years and tons; reducing or turning off the auxiliary heating or magnetic fields would immediately reduce and stop the reaction.

that cause local transport, often resulting in turbulence that can greatly reduce confinement. Transport at the plasma edge is especially complex and difficult to fully understand due to the plasma undergoing large variations in parameters in a small region governed by a large number of interacting physical processes, including unique magnetic and electric fields, stability and transport mechanisms separate from the core plasma, and interactions with neutrals, sheaths, and material surfaces [96].

1.2   Materials in fusion devices

Besides the major challenge of preventing heat from escaping the plasma, the other major challenge of fusion is how to make the walls of the confinement device compatible with the plasma. The walls of the device, and all other materials exposed to the plasma, are called plasma-facing components, or PFCs. The conditions faced by the PFCs in a tokamak are most similar to being near the surface of the sun or a spacecraft re-entering Earth's atmosphere at several times the speed of sound [96]. PFCs must survive these extreme conditions for years without replacement due to melting, cracking, erosion, redeposition, tritium retention, or dust generation, or else a fusion plant would have to be stopped for maintenance too often to be cost effective. Furthermore, even under constant bombardment, PFCs cannot contaminate the plasma with too many impurities that cause extra heat loss and reduce fusion performance.

The topic of plasma-surface interactions (PSI) covers many effects caused by the large fluxes of particles and heat impinging on PFCs. These fluxes, while high in steady state, can increase by factors of 100 during repeated transient events such as edge-localized modes (ELMs) [109]. In addition, PFCs must withstand large neutron fluxes, causing up to 100 displacements of each atom in the crystal structure of the material [30], and should not produce any especially harmful radioisotopes when exposed to such a flux.

In nearly all past, present, and planned future fusion devices, solid PFCs were and are used. However, liquid metal PFCs have also been proposed, as they could provide solutions to many of the challenges facing fusion devices [1, 17]. First, they are inherently robust, as they have no physical structure to break or degrade under neutron bombardment, and erosion can be immediately replaced by flowing the liquid metal. This is in contrast to solid materials that would have to be very thick to withstand years of erosion and avoid costly shutdown and maintenance periods. Furthermore, solids can be severely damaged by transient events like ELMs and disruptions, while a liquid might simply evaporate and then be easily flowed back. Liquid metal PFCs can also avoid shutdowns and in-vessel maintenance due to tritium retention, as tritium retained in the liquid metal can more easily be extracted outside of the vessel.

Liquid metals can also enable novel solutions to other materials challenges, separating to some extent the PSI, heat, and neutron issues. It could be possible to handle the massive heat loads of a fusion reactor using the liquid metal PFC itself, either flowing it rapidly to extract heat [1] or allowing it to evaporate and condense [31], or even re-radiate the heat [47]. By allowing the liquid metal to handle the PSI issues, and possibly the heat loads, many more options could be available for a substrate holding a liquid metal PFC than a solid PFC.

1.3 Impurities in fusion plasmas

In addition to the requirement that the PFC material be able to handle contact with the plasma without excessive damage, it is also necessary that the plasma not suffer too much contamination from contact with the PFC. In fusion plasmas, PFC material that enters the plasma by physical and/or chemical sputtering is quickly reduced to its constituent atoms and ionized. Impurities can also enter from leaks in the vacuum system and residual gases and compounds on the PFCs, or be deliberately introduced

in experiments. These impurity ions have a wide range of (mostly bad) effects on the plasma, diluting the fuel and increasing radiated power, electrical resistivity, and collisonality. These effects increase as the amount of impurities increase, and also as the impurity ion charge Z increases. As thermonuclear fusion plasmas can ionize very strongly bound electrons, for low-Z and medium-Z elements the ion charge will become the nuclear charge.

One of the simplest effects impurities have is diluting the reactive D-T fusion fuel with non-reactive particles. Fusion devices are limited in how much plasma pressure they can confine, and this pressure is not used efficiently when confining non-reactive impurities. Worse still, impurities also contribute their electrons (which are also non-reactive) so that dilution increases with Z. Even in the absence of external impurities, D-T fusion produces He ions which must be exhausted to prevent negative effects, mainly fuel dilution.

Another (mostly) negative effect of impurities is increasing radiated power, whereby thermal energy in the plasma is lost as electromagnetic emission. The main types of radiative losses are atomic line transitions, bremsstrahlung, and synchrotron emission. Line emission is due to atomic transitions of bound electrons in impurity atoms, and has a complex dependence on impurity charge (approximately as Z^4), electron temperature, and electron density [19]. Higher Z impurities such as W do not become fully ionized and emit very strongly, such that even 0.01% W impurity would be a major concern for a fusion device [106]. However, low Z impurities will be fully ionized in thermonuclear plasmas, and will only emit line radiation in the narrow, cooler edge region. In certain device designs this edge line emission can be beneficial, exhausting heat through isotropic radiation that can be spread over the entire first wall area rather than the intense heat fluxes that can occur at the narrow divertor strike point [49].

Bremsstrahlung losses are mainly due to deceleration of electrons by interactions with ions and approximately follow the relation $P_{brem} \propto n_e^2 \sqrt{T_e} Z_{eff}$ with electron density n_e, temperature T_e, and effective plasma Z due to impurities $Z_{eff} = \sum_{ion} n_j Z_j^2 / n_e$ [42]. Thus even fully stripped impurities increase radiative losses with a quadratic dependence on Z. Synchrotron radiation is mainly emitted by the electrons orbiting field lines, and increases with magnetic field strength and electron temperature [106].

Impurities also increase the frequency of collisions in the plasma, as their higher Z causes stronger electrostatic interactions between interacting particles with collision rates ν scaling approximately $\sim Z_{eff}^2$. More collisions means more transport that flattens gradients and generally reduces confinement. Plasma resistivity also increases with more collisions, scaling approximately $\sim Z_{eff}$, which has a variety of effects on overall performance. In a tokamak that depends on plasma current for stability and confinement, more current drive is needed, either by faster flux consumption or enhanced auxiliary current drive. The specific structure of the impurity profile is also important to the stability of the plasma through its effects on resistivity and currents in MHD stability. In fact, increased Z_{eff} may improve peeling-ballooning stability in certain circumstances, allowing improved performance without ELMs [93]. The effects of impurities on resistivity, currents, and ohmic heating at magnetic islands, as well as radiated power, may also be crucial to the Greenwald density limit, with higher Z impurities generally worse [29]. Impurity radiation and resistivity also have important implications for initial breakdown, burn through, and ohmic heating [77].

While PFCs in early fusion devices were originally chosen for survivability, using materials like stainless steel and tungsten, they suffered large amounts of high-Z impurities entering the plasma [24]. This motivated the switch to low-Z PFCs like carbon, and also the switch from limiters to divertors in order to further insulate the core plasma from the PFCs [73]. Divertors were successful enough that high-Z PFCs like W are and will be used in many new and planned devices [81, 71].

While low-Z impurities are generally less harmful once in the plasma, high-Z materials have the saving grace that they physically sputter much less, and thus enter the plasma in much lower quantities [5]. This is a major reason that W is considered the most viable PFC by the general fusion community, as it is eroded much less quickly than C. Many complicated effects are involved in determining the total impurity source at the PFC, though physical and chemical sputtering are generally most important. The level of impurities in the plasma is also dependent on the degree to which sputtered atoms penetrate to the core plasma. Impurities with low first-ionization potentials are more likely to be ionized within a single gyro-radius of the wall and thus redeposit promptly, never interacting with the core plasma. Different impurities are also affected differently by forces in the scrape-off layer (SOL) and the core plasma. In order to avoid continuous accumulation of impurities in extended discharges, a number of tokamak operating regimes with good energy confinement but enhanced (especially for high-Z impurities) particle transport have been studied, including ELMy H-mode [109], RMP (Resonant Magnetic Perturbation) H-mode [22], (Quiescent) QH-mode [34], and I-mode [74].

1.4 Lithium as a material in fusion devices

Lithium, as a low-Z, easily liquefied metal, presents an intriguing choice as a PFC material [65]. It is in fact the lowest Z possible material, so that much higher quantities on Li can be tolerated in a fusion plasma before having deleterious effects [106]. An alkali metal, it also has a very low first ionization potential, meaning Li impurities are more likely to ionize within a gyro-radius of the wall and promptly redeposit rather than entering the plasma. It is also very reactive chemically and can act as a getter for higher-Z residual gases. With a melting point of 180 °C, it can be studied in experiments without needing excessively high temperatures.

There are some properties of lithium that raise concerns of unacceptably large ingress of lithium into the plasma. Lithium has a fairly low boiling point, such that it reaches high vapor pressure at lower temperatures than other possible liquid metals. It also has a high sputtering yield, which is further enhanced at increased surface temperature. Gettering can be a double-edged sword, as it can concentrate the other, more harmful residual gases at the PFC surface, potentially making them more available to the plasma. There is a possibility it can even chemically leach impurities from below the surface of the substrate.

Success in previous experiments gives reason to believe these negative factors are outweighed by the positives. Test stand experiments have also shown that influxes at high surface temperatures many not be as high as expected [2], and Li sputtering could actually be reduced if the edge plasma is sufficiently hot [55]. There are also concepts that make use of the evaporation of Li to handle high heat fluxes [47, 31].

The key property of Li that separates it from other potential liquid metals is that its strong chemical reactivity means that it can chemically bond hydrogen fuel escaping the plasma, reducing plasma recycling [4]. Recycling occurs when hot plasma hydrogen ions impact the PFC and either return as cold neutral atoms or displace a bound hydrogen atom which enters as a cold neutral. In most materials, the hydrogen recycling coefficient, defined as the flux of hydrogen neutrals into the plasma divided by the flux of hydrogen ions into the PFC, is unity in steady state. This means there is a high density of neutral hydrogen at the PFC acting as the dominant fueling source, making it difficult to control the density profile or even the total plasma density. The cold neutrals can strongly affect the plasma temperature boundary condition, with high thermal losses due to collisions and charge exchange. This means there must be a large temperature gradient between the cold edge and the hot thermonuclear core, which acts as a drive for instabilities that cause additional thermal losses. The

neutrals also cause a drag force opposing plasma rotation, reducing the stabilizing effect of rotation.

The benefits of reducing impurities and recycling have been demonstrated in many experiments using Li wall-coatings in tokamaks. TFTR introduced Li wall-conditioning on graphite PFCs in an effort to control density and impurities, but it also improved performance with the "super shot" regime, with large increases in energy confinement time τ_E, fusion gain Q, and fusion triple product $nT\tau_E$ [69]. CDX-U introduced Li on stainless steel PFCs mainly as a technology demonstration of liquid Li handling, but it resulted in a large increase in τ_E and reduced recycling and resistivity, with less loop voltage required to maintain the plasma current [68]. However, diagnostic capabilities for these CDX-U experiments was limited, and impurity transport studies in CDX-U [95, 94] were performed before the introduction of Li, so a complete understanding of the effects of Li was not possible.

In NSTX, Li coatings on C PFCs led to increased confinement and rotation [70]. Surprisingly, there was very little core Li contamination, with concentrations remaining $< 0.1\%$ even with 1.3 kg of Li applied to the walls and a much higher sputtering yield for Li than C [82, 89, 90]. Furthermore, C impurities substantially increased after Li coatings led to suppression of ELMs and improved overall confinement, leading to accumulation of C in the core up to $\sim 10\%$ concentration. Using profile measurements and modeling with codes including TRANSP, NCLASS, and MIST, it was determined that the C impurity accumulates and pushes out Li largely due to standard neoclassical transport, though effects at the wall and in the SOL are important as well [90].

These theories and experimental results motivated the Lithium Tokamak Experiment, constructed to study the effect on plasma performance of nearly complete coverage of PFCs with solid and/or liquid Li. LTX is a modest-sized spherical tokamak based on many of the CDX-U components, including the vacuum vessel, toroidal field

coils, and central solenoid. It adds 4 stainless steel lined shell segments that surround $\sim 80\%$ of the plasma area and can be heated to ~ 350 °C for liquid Li experiments. LTX has shown major improvements in performance due to solid and liquid lithium wall coatings [87, 88].

1.5   Dissertation objectives

The issues discussed thus far motivate the work in this dissertation. Harnessing fusion power as an energy source would have tremendous benefits, and finding a suitable first-wall material is a major challenge. Lithium, as a liquid metal PFC, has great potential to enable solutions to many of the problems caused by damage to the wall, impurities reducing plasma performance, and enhanced losses due to plasma recycling. Specifically, this work aims to study impurity transport with lithium wall-coatings in LTX, a spherical tokamak with all-metal PFCs. Many of the questions this work endeavors to answer were raised by impurity transport studies in NSTX [90], and considering how impurity transport might change in a device with all-metal PFCs.

The first main objective of this dissertation is to measure impurity densities and concentrations in LTX. Details of the experimental device, the diagnostic set, and the experiments in which impurities were measured are given in chapter 2. Chapter 3 discusses the LTX Thomson scattering (TS) diagnostic, which was refurbished and improved in the course of this work to better measure electron density and temperature profiles. Impurity emission profiles were measured using the novel High-throughput, Accurate-wavelength, Lens-based (HAL) spectrometer , described in chapter 4, and used the TS measurements and ADAS database for analysis. These measurements enabled determination of the impurity density profiles, and determination of the effects of these impurities on the plasma via radiated power and resistivity.

These measurements will give insight into several important questions about impurities in discharges with Li-coatings on all metal PFCs. What is the effect of almost fully surrounding the plasma with Li-coated PFCs? Does Li build up to high levels when there is no bulk C, and presumably less of the C impurities that pushed out Li in NSTX? Does C still accumulate at all without bulk C components? Does the strong affinity of Li for O bring too much O into the discharge? Are other impurities - for example from the substrate material - a concern?

It should be noted that this work does not address the source terms for these impurities, or predict levels in future devices by extrapolation. This work also does not significantly address the low recycling aspects of lithium PFCs, as recycling was not well diagnosed in these experiments.

The second main objective of this dissertation is to develop a basic initial understanding of impurity transport in LTX especially as it relates to the topic of Li coatings on metal PFCs. Are there similar dynamics to NSTX with C PFCs, where Li is pushed out by C, or perhaps in this case, where Li pushes out other impurities? Is impurity transport in LTX neoclassical, as seen in other spherical tokamaks, including NSTX? Do results from the large, diverted, NBI heated NSTX with Li on C PFCs extend to the smaller, limited, ohmically heated LTX with Li on metal PFCs? Understanding impurity transport is an important issue as it is closely linked to ion thermal transport, and neoclassical transport is the irreducible minimum in a toroidal device.

In order to assess the impurity transport, a full plasma model was constructed using TRANSP to integrate several LTX diagnostics, including the Thomson scattering and impurity spectroscopy profile measurements. The TRANSP model is described in chapter 5. Next, in chapter 6, this model and the NCLASS and MIST codes were used to assess the impurity transport in LTX and answer some of the above questions.

Finally, in chapter 7, these results and their implications are discussed, as well as the path forward in future work at LTX.

Chapter 2

The Lithium Tokamak Experiment

The Lithium Tokamak Experiment is a modest-sized spherical tokamak designed to study the low-recycling regime through the use of close-fitting, lithium-coated, heatable shell quadrants surrounding the plasma volume [67]. LTX research also seeks to develop technology and procedures for safely and effectively handling, applying, maintaining, and monitoring solid and liquid lithium coatings in a fusion device. LTX has used several methods to apply Li coatings, and a recurring theme in describing the LTX device and its capabilities is the great flexibility in studying a wide variety of surface and plasma conditions [87, 88, 103, 58]. Furthermore, the wall conditions greatly affect the plasma, and vice versa. Diagnostics on LTX include numerous spectroscopic diagnostics for measuring various impurity species. This chapter provides a general overview of the experimental device and its diagnostics, excluding the Thomson scattering (chapter 3) and Doppler spectroscopy (chapter 4) systems. This chapter also describes the series of plasma discharges studied throughout this work.

2.1 The LTX Device

The LTX facility is based in large part on components from the CDX-U facility, with the same vacuum vessel, toroidal field (TF) coils, and central Ohmic heating (OH)
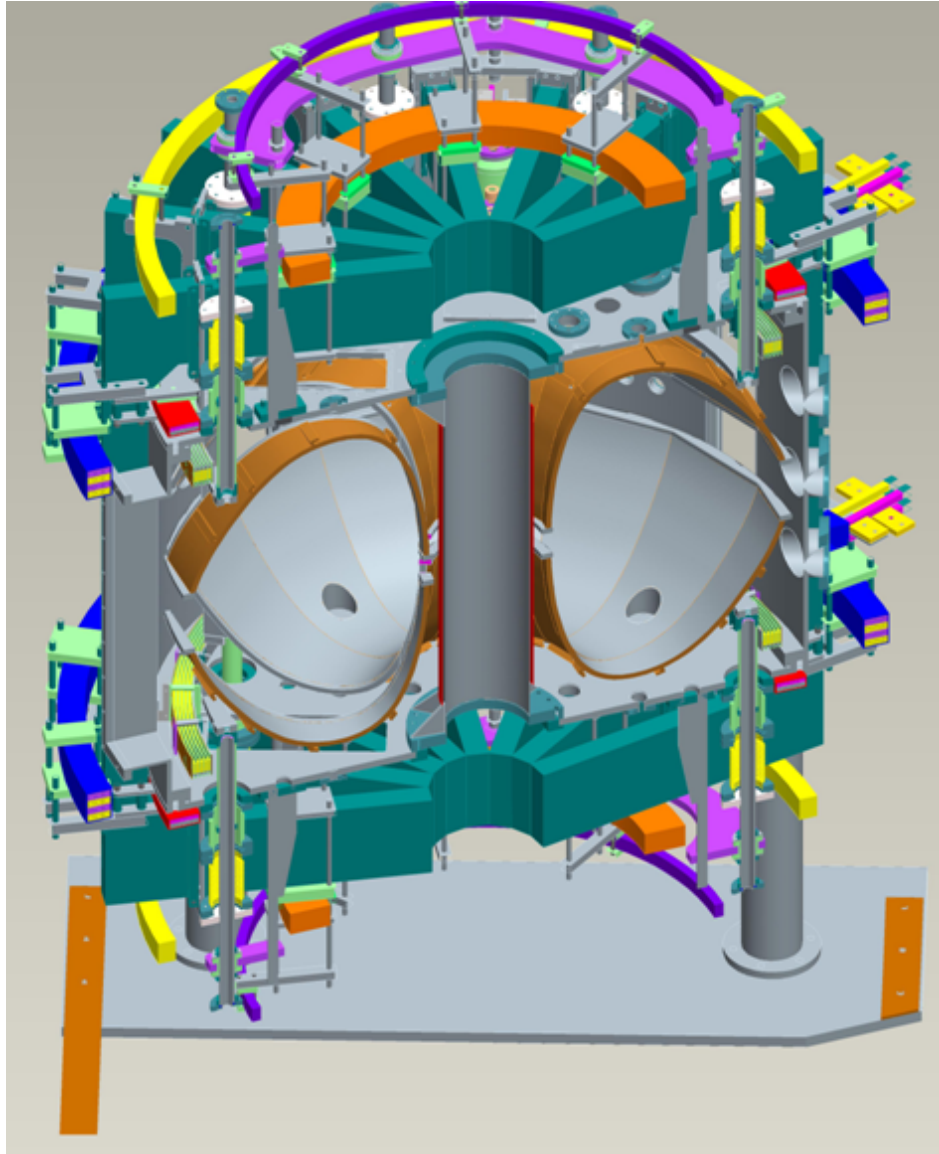
Figure 2.1: Cutaway 3D CAD model of LTX

solenoid. The vacuum vessel is a stainless steel cylinder with height 0.9 m and inner diameter 1.4 m [76].

2.1.1 The LTX magnetic coil set

The LTX coil set consists of 16 rectangular toroidal field coils, with demountable outer conductors and 128 total central conductors potted within the central solenoid. The central solenoid is 74 turns of 1/2" square copper with a 1/4" diameter circular cooling channel, and is actively water cooled during operations. The external field from the OH solenoid is canceled by 2 pairs of compensation coils.

There are 6 sets of vertical field coils, shown in Figure 2.1 and described in [11, 45]. The coils are driven by a combination of programmable power supplies and capacitor banks. The OH is driven by a programmable 330 kJ, 900 V max capacitor bank. Discharging of the capacitors can be duty-cycle modulated by 28 insulated-gate bipolar transistors (IGBTs) in an H-bridge configuration, up to a current of 28 kA and a frequency of 2 kHz. The IGBTs are controlled by a National Instruments (NI) field-programmable gate array (FPGA) with a NI LabView software interface. The TF and the main vertical field coils are driven by Robicon programmable power supplies. The TF supply is limited by its maximum voltage of 500 V, corresponding to a current of ~ 2.7 kA and field of ~ 0.17 T at the nominal magnetic axis ($R_0 = 0.4$ m).

In all cases the programming and timing of the supplies is prescribed before each discharge and selected based on educated trial-and-error, as feedback control is not presently available in LTX. In the course of developing and optimizing discharges, as well as upgrading and reconfiguring power supplies, a variety of different coil programming settings has been explored. Varying the timing and currents of the various power supplies and capacitor banks for the field coils allows exploration of effects of discharge duration, current, position, shaping, and other important parameters, and
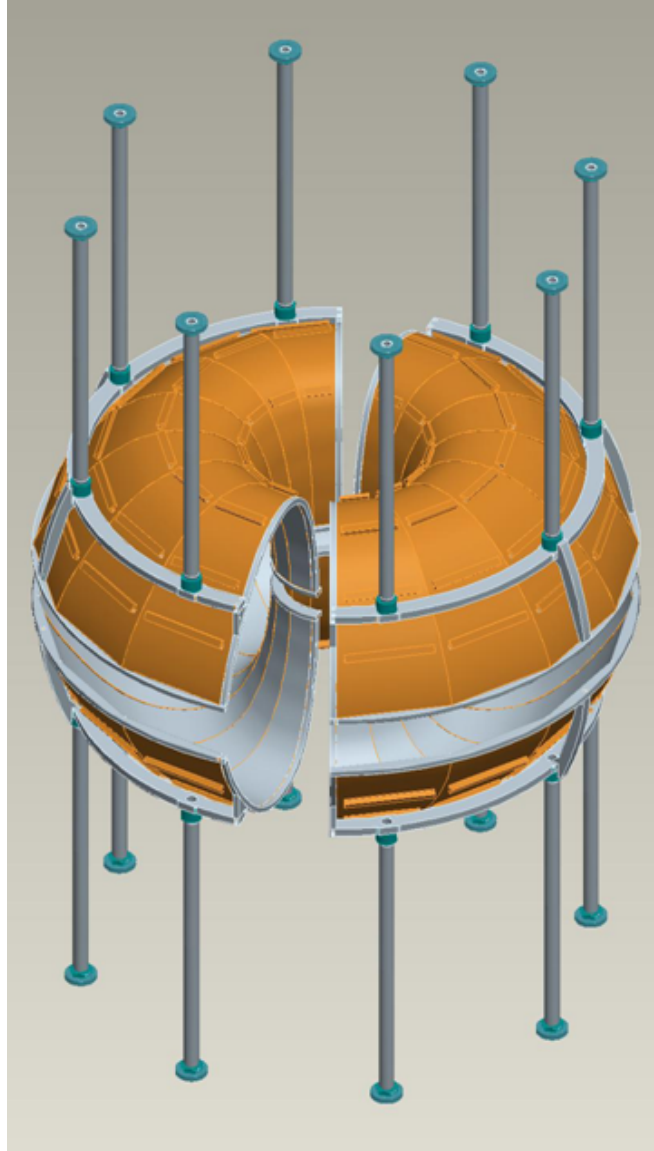
Figure 2.2: 3D CAD model of LTX shell

has created a large database of experiments performed with varying plasma parame-
ters.

2.1.2 The LTX shell and vacuum conditioning

The most significant difference between CDX-U and LTX is the addition of a conduct-
ing, heatable plasma-facing toroidal shell inside the vacuum vessel, shown in Figure
2.2. The shell defines LTX and its mission to study plasma-surface interactions and

the low-recycling regime with lithium coatings. The shell has poloidal breaks at the inner and outer midplane and toroidal breaks on the east and west sides of device, and is thus made of 4 quadrants labeled upper/lower and north/south. The shape of the shell is designed to be conformal to a plasma with major radius $R_0 = 0.4$ m, minor radius $a = 0.26$ m, elongation $\kappa = 1.6$, and triangularity $\delta = 0.4$. The shell is made of 3/8" oxygen-free high-conductivity copper, with an 1/16" 304 stainless steel liner explosively bonded to the inside surface facing the plasma. The high thermal conductivity of the thick copper keeps the temperature spatially uniform, and the high electrical conductivity of the copper aids in passive stabilization of the plasma, though formation of large eddy currents also complicate breakdown and magnetic measurements. The stainless steel liner provides a lithium compatible plasma facing component (PFC), and nickel plating on the outside (facing away from the plasma) protects the copper from inadvertent Li exposure. 32 resistive heaters with up to 30 kW of total power and 32 thermocouples are attached to the outside of the shell, and have been operated up to a temperature of ~ 350 °C. The system was designed for operation up to 500 °C, but due to uncertainty about heat loads on the center stack, was limited in the present work to short periods at ~ 350 °C (small sections of the shell approach 500 °C during Li evaporation) or steady state operation near 270 °C.

The condition of the plasma-facing shell, which also acts as the limiter for the confined plasma, has a large impact on the performance on the plasma. A wide variety of surface conditions has been explored in LTX, creating a large data set for understanding the material surface and its effects on the plasma. Discharges run against the bare stainless steel liner had generally poor performance [11], and performance without coatings was only somewhat improved by basic vacuum conditioning techniques like baking and glow discharge cleaning [59]. Several different baking procedures have been used, with variation in temperature, duration, use of centerstack cooling, and combination with other conditioning techniques. Initial baking proce-

dures heated only the shell but now include heating the vacuum vessel by circulating hot water through copper tubing attached to the outside. Extensive baking, and vessel cooling using the same copper tubing, also improved vacuum conditions even while the shell was heated to high temperatures. Glow discharge cleaning was also varied in duration, gas pressure, and choice of gas, with He, Ne, and Ar all used. Vacuum conditions were also improved by addition of an auxiliary turbopump and a getter pump to supplement the primary turbopump and cryopump. Careful preparation of in-vacuum components was especially important for those added after the main vessel was well-conditioned. The variations in surface conditions in the LTX data set also includes effects of air leaks that persisted after pumpdown or that arose after thermal or mechanical cycling but were eventually found and sealed. Pump failures or accidental valve openings also allowed pump oil or ambient air to enter the vacuum chamber on a few occasions. Time is also an important consideration in conditioning, as newly introduced components slowly release adsorbed gases and residual gases redeposit on conditioned surfaces.

2.1.3 Lithium conditioning in LTX

The multitude of surface conditions in LTX created by the various vacuum techniques is made even more complex by the application of several different Li conditioning techniques [59]. Li is a very effective getter, especially when it coats the ~ 4 m^2 shell surfaces, and greatly reduces residual water, oxygen, and hydrocarbons. However, these compounds can accumulate on the surface of the Li coatings, further enhancing the dependence of surface conditions on vacuum conditions, temperature, and time. Alternately, heating and glow discharge cleaning can remove these compounds and redeposit lithium. In addition to depositing Li in different ways, the different Li conditioning techniques vary in how they affect the existing Li coatings. They variously

22

involve installing, re-installing, and heating in-vacuum components that may outgas, as well as introduction of inert working gases with trace quantities of impurities.

Li coatings greatly improved performance from their very first application in LTX [61], and have improved performance more as techniques have improved [103, 88]. Initially, Li was applied by evaporation of several grams of lithium from heated ceramic crucibles into the helium-filled vacuum vessel at the beginning of a run day [61]. A similar system using a formed strip of tungsten as both heating element and Li reservoir in a shallow indentation was also used without helium, evaporating solely in the upward direction.

Another method for application of lithium replaced the ceramic crucibles with heated tungsten crucibles with formed spouts on the bottom and tungsten weights on top of the lithium [45, 88, 59]. The weights forced Li to drip out of the bottom once it was liquefied, falling into the heated lower shell segments and forming a pool in the bottom. The lower shell segments have dams at the ends to retain a pool of liquid lithium, and it was hoped that the liquid lithium would wet to the lower shell surfaces and create a thin coating over a wide area. However, the lithium formed compact pools instead as wetting was inhibited by a combination of surface impurities and insufficient shell temperature. The pools themselves became covered with impurities, changing from a shiny liquid metal surface to a duller gray. Experiments with these small pools as the sole area coated in recently-applied lithium (liquid or solid) did not achieve high performance [66, 59].

In order to produce Li coatings over a larger area, electron beams were used to further heat and evaporate the Li pools. This technique was first pioneered in CDX-U [68] and has proven to be a highly effective method to produce Li coatings, enabling many experiments including in LTX the first successful operation of a tokamak almost completely surrounded by liquid Li surfaces [88]. The Li pools were created in the bottom of the shell as described above. Electron guns consisting of a tungsten filament

23

and anode and cathode plates were mounted on bellows drives at the top of the vacuum vessel and inserted through cutouts in the upper shell segments. The electron guns were biased 4-5 kV and the filaments heated with ~ 20 A, allowing up to ~ 400 mA of electron current to be extracted for a beam power of $\sim$ 1-1.5 kW. The beam was confined and steered onto the Li pool using a combination of the vertical field and toroidal field coils driven by DC power supplies. The beam was monitored with an in-vessel mirror mounted on a differentially pumped Wilson seal. The system is described more fully in [59].

When the beam struck the impurity covered Li pool or shell surface, it emitted a blue glow, likely due to ionizing oxygen. When the Li pool was fully liquefied by pre-heating the shell before beam heating, the dull impurity surface layer initially remained. The combination of the guide magnetic fields and the electron beam heating and current induced thermoelectric magnetohydrodynamic (TEMHD) forces in the liquid Li pool, causing the pool to rotate rapidly [48]. The combination of additional direct heating and stirring caused the impurity layer to break up and dissolve, restoring a clean shiny lithium surface with a pink glow from ionized Li. The beam heating was typically applied for 5-15 minutes at the beginning of a run day, evaporating Li fairly uniformly over the shell surface. Thermocouples on the outside of the bottom shell segments directly below the Li pools were used to monitor the temperature, which rose to ~ 500 °C from an initial temperature of ~ 300 °C. Depending on the experimental plan, the upper shell segments could be heated or not during and/or after evaporation, and experiments could begin within 30 minutes with the shell still hot or wait until later in the day or even the next morning until they had cooled. For initial experiments, only the beam on the south side of LTX was available, so only the south shell segments were coated (as the central solenoid blocked line-of-sight evaporation from one side to the other). A second beam was later added for full Li

coverage and could be operated simultaneously, due to symmetry of the beams, Li pools, and guide fields.

One of the main purposes of research with Li coatings in LTX is their potential to reduce recycling of hydrogen on the PFCs, which produces a high density of cold edge neutrals that provide the primary fueling source in most tokamaks. However, reducing this fueling source does little to improve plasma performance if it is replaced by a similar fueling source, such as an undirected edge gas puff. Core fueling techniques such as neutral beam injection or cryogenic pellet injection were not available in the present work on LTX. Prior research on LTX [61] showed that low field side fueling with a close-coupled supersonic gas injector and a molecular cluster injector could be quite efficient fueling sources that allowed LTX to take advantage of the reduced recycling from Li. Furthermore, even a fairly standard low field side gas puffing source was shown to be reasonably efficient when collimated and closely coupled to the plasma. Work on other devices [23, 64, 100] showed higher efficiency from gas puffing on the high field side (HFS), which led to installation of such a system in LTX [45]. The HFS puffer on LTX has a relatively long distance between the puffing valve and the exit nozzle, which prevents a short puff with fast temporal response, but should not significantly affect fueling efficiency. The nozzle is still closely coupled spatially to the plasma, and the good performance of discharges fueled with this method led to its use for the great majority of recent experiments. However, the slow time response of the gas shutoff prevented a direct estimate of fueling efficiency. In addition to testing a variety of fueling techniques, many different settings of puff timing and duration have been used in LTX experiments. Varying the fueling most directly affects plasma density, which in turn affects the entire discharge through changes in temperature, pressure, resistivity, total current, ohmic heating, and collisionality.

Taken all together, a very large parameter space was available for exploration in LTX, and indeed a large data set of experiments has been assembled with significant

variations in coil programming, fueling techniques, and vacuum, surface, and lithium conditions. The plasma itself acts to change surface conditions, with dependence on number, duration, and performance of discharges, location of the limiting surface, manner of discharge termination, amount and location of fueling.

These closely coupled, complex systems have potential to provide powerful insights into many important problems in fusion research, but also make for a potentially complicated analysis. The scope of this work is therefore restricted to a single plasma condition. An extensive data set was collected over a single day of experiments under fairly constant conditions to optimize the accuracy of the diagnostic measurements. The analysis tools and framework developed for this data set, however, can be extended to understanding the wide variety of conditions explored in LTX.

2.2   Diagnostics

Just as LTX has been designed to explore a wide variety of experimental conditions, an extensive set of diagnostics has been developed to measure many different plasma parameters. Many have been added and upgraded since the first LTX experiments, while some have been removed. A brief overview of some key systems follows. The Thomson scattering and visible impurity spectroscopy systems are described in detail in Chapters 3 and 4, respectively.

2.2.1   Magnetic diagnostics and reconstructions

Some of the most fundamental plasma diagnostics are the various magnetic sensors installed on LTX [12, 11, 13, 88]. Plasma current is measured with a Rogowski coil in a re-entrant stainless steel formed bellows mounted on the inside of the vacuum vessel surrounding the shells. The signals from the Rogowski loop and the other magnetic diagnostics are integrated with differential integrator circuits and digitized

at 100 kHz with D-tAcq digitizers. A toroidal loop is similarly mounted in-vessel in rigid stainless steel tubing to measure plasma diamagnetism. A compensation coil is mounted below the vacuum vessel (but within the TF coils) to null out the contribution from the toroidal field coils. The signals are combined electronically before being integrated and digitized. Arrays of poloidal flux loops are mounted on the center stack and on the outside of the shell, both on the high and low field sides. The midplane center-stack-mounted poloidal loop is not integrated and measures the loop voltage induced by the ohmic solenoid. Arrays of compact, multi-axis pickup coils are mounted in re-entrant tubes that extend into one of the toroidal breaks between the shell segments [88]. Saddle coils are also mounted in the same gap between the shell segments. Finally, Rogowski coils around the transmission lines from the power supplies to the coils are used to measure coil currents.

The various digitizers used in LTX, including those used for the magnetics, store their data in an MDSplus database [26] in a tree structure. Some of the signals, like plasma current, can be used almost directly from the tree, requiring only simple baseline subtraction and a calibration factor for use in simple analyses. MATLAB tools are available to condition the magnetic signals to reduce noise and pickup, subtract integrator offset and drift, and apply calibrations for use with additional analysis. MATLAB tools also are available to estimate plasma stored energy and the basic plasma geometry including the last closed flux surface.

Magnetic equilibrium reconstructions have been challenging in LTX due to 3D eddy currents in the shell. Previous LTX reconstructions [11, 32] used LRDFIT (LR circuit model with Data FITting capabilities) [75], a 2D reconstruction code. As an axisymmetric code, a modified shell conductivity was necessary to produce reasonable LRDFIT equilibria [11]. Due to the large effort needed to generate magnetic equilibria, previous LTX analysis [45] used LRDFIT reconstructions from a shot sequence similar, but not identical to the one being analyzed, or used the CHEASE [62, 63]

code to make model equilibria constrained only by global parameters like plasma current and toroidal field and prescribed geometric parameters. Another LTX study [88] calculated the magnetic boundary using flux loop measurements and a cylindrical model.

Most recently, a collaboration with University of Washington has enabled use of the PSI-TRI [36, 35] code, which captures the eddy current behavior using a dominant eigenmode method. Throughout several reconstructed discharges, the eddy current effects agree reasonably well with a 3D eddy current analysis using VALEN [14]. The free-boundary equilibria also agree throughout the discharges with direct calculation of the boundary from flux loops. Additional constraints, such as pressure profile measurements can be incorporated into the analysis.

2.2.2   Microwave diagnostics

Through a collaboration with UCLA, LTX has a 1 mm microwave interferometer for measurements of the line-integrated electron density. Previously used on NSTX, this system is in a Michelson configuration following the design of [83] and reflects the microwaves off a stainless steel mirror mounted at the midplane on the center stack. In early LTX experiments, this system was mounted with a vertical path through the plasma at the nominal major radius, while a different, vertically scannable 2 mm system reflected off the center stack at the midplane [61, 25]. After hardware problems with the 2 mm system, the 1 mm was moved to the midplane and has provided reliable measurements throughout the most recent experimental campaign. In the present 1 mm system, the output of the phase comparator has an effective frequency resolution < 200 kHz and is digitized with a 3 MHz Joerger CAMAC mounted digitizer. Like the plasma current, the digitized signal stored in the MDSplus tree typically requires only baseline subtraction and simple calibration factor for basic analysis. However,

the signal often suffers from fringe jumps, especially during disruptive events, so some IDL and Python scripts were written to correct the signals when necessary.

In addition to operating the 1 mm interferometer, UCLA collaborators have also installed a profile reflectometery system. The system is based on microwave hardware previously used on NSTX [54] and uses two frequency-modulated continuous-wave reflectometer channels, with frequency ranges of 13-20 and 20-32 GHz. Density profile and fluctuation measurements from $2 - 13 \times 10^{-12}$ cm^3 (with ordinary-mode waves) are made every 8 μs. The signals are digitized at 100 MHz and produce a radar image of the reflected signal, which is analyzed using the POLAN (POLynomial ANalysis) method [101].

2.2.3 Plasma radiation diagnostics

In order to measure plasma radiated power, an unfiltered 20-channel AXUV20-ELM diode array was originally installed to serve as a multichannel bolometer [32]. The signals are amplified with a two-stage trans-impedence pre-amplifier designed in [102]. However, the array was installed in a vertical orientation on a radial view and could not view the outer part of the plasma, making the diagnostic of limited utility for actually determining radiated power profiles by inverting the line-integrated measurements [45]. Due to the small size and low aspect ratio of LTX, as well as view obstructions from the shell and gate valves, full profile measurements are generally difficult for any LTX diagnostic. The bolometer array is currently undergoing an upgrade to re-entrant viewing and has not been available for the most recent experiments, including those described here.

Alongside the unfiltered bolometer array, LTX also has an identical AXUV 20-diode array filtered for the Lyman-α hydrogen emission line at 121.6 nm in order to measure hydrogen recycling. An additional 20-diode Lyman-α array was installed on a tangential view. As with the bolometer, these arrays were being upgraded to ad-

dress limited spatial coverage and were not available for the most recent experiments. H/D-α filtered line scan cameras were also used to measure hydrogen recycling in earlier configurations of LTX, but are no longer compatible with available viewports. Python tools are available for applying calibrations and basic analysis of the bolometer, Lyman-α, and H/D-α array measurements, though 2D modeling with DEGAS2 was found to be necessary to actually calculate plasma recycling [32].

As part of the collaboration with ORNL, LTX has an array of filterscopes that monitor visible line emission along 3 different sightlines at a total of 11 different wavelengths with a frequency of 100 kHz [32]. The filterscopes monitor Li I-III, C II, O II, H/D-α, -β, and -γ, and a visible bremsstrahlung channel at 527 nm, with views in the radial midplane and lower shells. These measurements provide information about recycling, edge impurity sources, and plasma impurity levels. Presently they are mainly useful qualitatively as quantitative interpretation would require significant analysis effort. Python codes to aid in quantitative analysis are available due to earlier work and were developed somewhat further during this work. The same 3 views used for the filterscopes are also instrumented with Ocean Optics HR2000+ miniature spectrometers with a wavelength range of 390-590 nm and 600 Hz sampling rate [32]. However, these spectrometers were not operational for most of the recent campaign.

Due to collaborations with Lawrence Livermore National Laboratory (LLNL) and Johns Hopkins University (JHU), LTX has also used several extreme ultraviolet spectrometers to measure emission from higher impurity charge states. The LLNL Long-Wavelength Extreme Ultraviolet Spectrometer (LoWEUS) was installed on a radial midplane view and could be adjusted to monitor wavelengths between 3-40 nm [57]. Typically, it measured line emission across the 10-30 nm range with ~ 0.03 nm full-width at half maximum (FWHM) resolution of lines, acquiring a single spectrum constituting an average over the entire discharge. LoWEUS provided a valuable survey of Li II-III, C IV, and O IV-VI emission [66]. Existing Python software for

automated wavelength calibration and line identification has been heavily modified and upgraded during the course of the present work.

The JHU Transmission Grating Imaging Spectrometer (TGIS) covers $\sim$ 5-70 nm with $\sim$ 1 nm FWHM line resolution and has capabilities for both spatial and time resolution [103]. However, it was installed on a tangential port where it could only view the core plasma, and set to only acquire a single spectrum per discharge in order to increase signal to noise and simplify analysis. It provided generally similar information to LoWEUS, covering a wider wavelength range though its lower resolution could make discrimination of nearby lines difficult. A study of Li/O line ratios from TGIS measurements in experiments with solid and liquid Li [103] used measurements from the HAL spectrometer ([9], Section 4.2) to address questions related to spatial and time resolution. TGIS was removed from LTX before the experiment in this work and is now installed on NSTX-U.

The LLNL HI-resolution Grazing-incidence Grating Spectrometer (HIGGS) is essentially a larger version of LoWEUS and can also measure emission within the 10-30 nm range, but with FWHM line resolution of 0.003-0.006 nm so that it could be used for ion temperature measurements [107]. However, the improved resolution restricts it to a narrower wavelength range in a single spectrum. After initial tests with a large, slow camera similar to that on LoWEUS, HIGGS was upgraded with a smaller, faster camera similar to that on TGIS, and operated with 10 ms frame times. Visual Basic software for automatic data acquisition and storage to MDSplus, originally developed for the visible Doppler spectroscopy system (Chapter 4), was also adapted for LoWEUS and HIGGS.

LTX has a Vision Research Phantom V210 monochrome fast camera to record videos of plasma emission, typically at frame rates of 1-10 kHz though higher rates are possible at reduced resolution. The camera views the plasma through a midplane tangential viewport that covers approximately the inner 3/4 of the plasma volume.

It has typically been operated with a H/D-α filter [61], though recently it has been used most often without a filter.

2.2.4 Plasma boundary and material surface diagnostics

LTX has several triple-tipped Langmuir probes at different locations [60]. A pair of probes are mounted on the center stack in the shell gap 15 cm above and below the midplane and flush with the shells. Another pair of probes are inserted through penetrations in the lower shells on bellows drives that can move them above and below the shell surface. Finally, a probe is installed on the outboard midplane on a bellows drive that can insert the probe to a major radius $R = 63.5$ cm. The probes are connected to electronics formerly used on NSTX [46] and can be operated as triple probes or swept single probes. As triple probes they measure n_e, T_e, floating potential, and ion saturation current at 250 kHz while as single probes they measure the entire $I - V$ characteristic at 2 kHz.

Important information about the vacuum, surface, and lithium conditions is measured with standard ionization gauges and residual gas analyzers (RGAs), as well as with the thermocouples on the shells and elsewhere inside and outside the vacuum vessel [60]. Fast ion gauges have also been installed to monitor neutral pressure on the fast timescales of the discharges. The usefulness of these various diagnostics has been further enhanced by creating scripts to log the vacuum gauges and making full use of commercial logging software for the RGAs and LabView logging software for the thermocouples. The various diagnostic signals can be correlated to each other and to plasma discharges and vacuum, surface, and lithium conditioning techniques. Still, these measurements only provide an indirect picture of the surface and lithium conditions.

In order to directly measure surface conditions, the Materials Analysis and Particle Probe (MAPP) was installed on LTX [58, 60, 59]. Originally developed for

use on NSTX in collaboration with Purdue University [99], and now University of Illinois at Urbana-Champaign, it allows four material samples to be inserted into a vacuum chamber and exposed to conditioning techniques and/or plasma discharges, then retracted for analysis. Analysis techniques used on LTX were primarily x-ray photoelectron spectroscopy (XPS) and thermal desorption spectroscopy (TDS). The probe head also included two single tip Langmuir probes for measuring plasma parameters near the samples. An ion source also enabled Ar sputter cleaning and H dosing of the samples, and low energy ion scattering spectroscopy (LEISS) and direct recoil spectroscopy (DRS) are under development in MAPP. On LTX, MAPP was used to study the effects on surface conditions of vacuum preparation, baking, glow discharge cleaning, lithium evaporation, and exposure to plasma and residual gases. However, it was removed from LTX before the final experiments discussed in this work and is now installed on NSTX-U.

2.3   LTX discharges for impurity study

This study is based on a series of 55 essentially identical plasma discharges produced on April 29, 2015. The experiments were performed with hydrogen plasmas and solid Li coatings on approximately room temperature shell surfaces the day after an evaporation. While experiments under many different conditions have been performed (see section 2.1.2), this was the most extensive data set under nearly constant conditions.

As described in section 2.1.3, Li coatings were produced by pre-heating both lower shell segments to $\sim 300\,°C$ and further heating each Li pool with a ~ 1.5 kW electron beam for ~ 20 minutes, resulting in an estimated ~ 150-200 mg or ~ 75-100 nm (following the estimation in [60], assuming uniform thickness) of freshly evaporated Li. Even in the improved LTX vacuum conditions this coating was covered in oxides
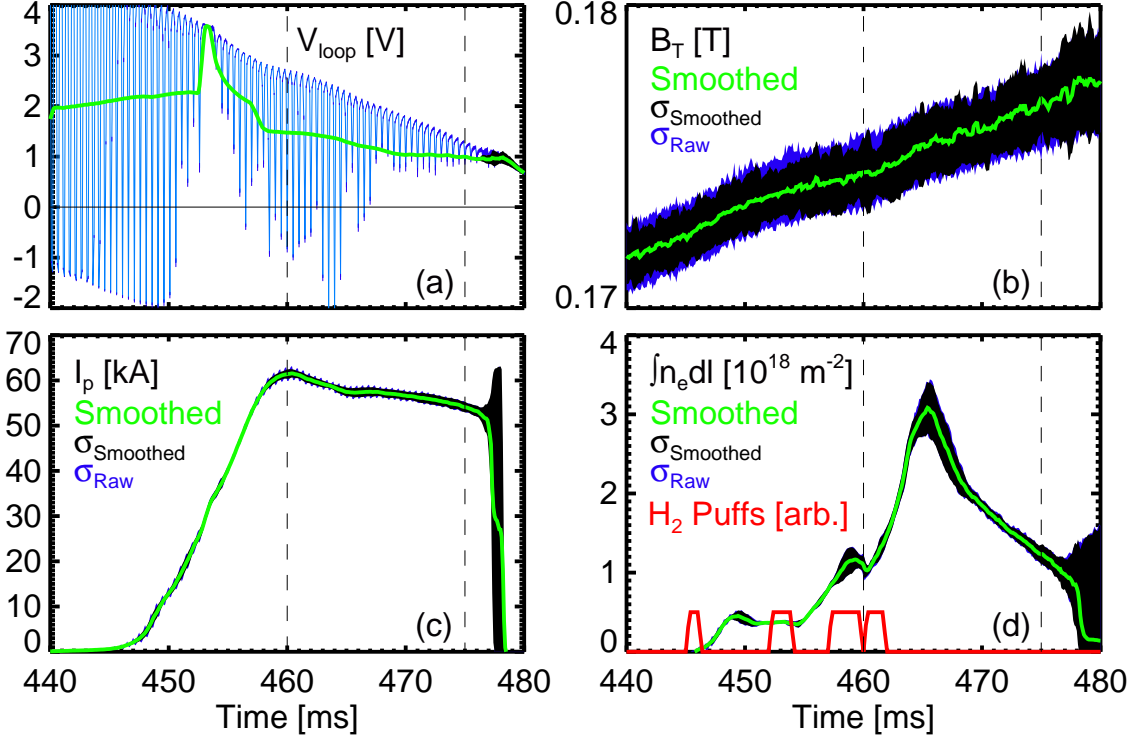
Figure 2.3: Waveforms of (a) loop voltage V_{loop}, (b) toroidal field B_T, (c) plasma current I_p, and (d) line-integrated density $\int n_e d\ell$. The green line is the median over the 55 discharges of the time-smoothed waveforms, the black band is the standard deviation of the smoothed waveforms, and the blue band is the standard deviation of the raw waveforms. The gas puffing is overlaid in (d) as a red line. The median smoothed waveforms were used as inputs to TRANSP in Chapter 5 from 460-475 ms, as indicated by the vertical dashed lines.

within minutes, but as demonstrated in previous experiments plasma performance would remain good for days or even weeks [60].

As will be described in section 3.1, the Thomson scattering laser only fired once per discharge and thus time resolved measurements required repeated shots to scan the Thomson measurement time. Furthermore, repeated shots allowed changing the wavelength of the HAL spectrometer in order to measure different impurity species, as will be described in section 4.2. Finally, averaging the spectra from multiple repeated shots allowed reduction of statistical uncertainties in both the TS and HAL analyses.

Of course, in order for an analysis based on multiple repeated discharges to be valid, they must be fairly reproducible. Waveforms in Figure 2.3 show that the 55 discharges were quite reproducible with respect to global parameters such as plasma current and line-integrated density, as well as key inputs of loop voltage and toroidal field. Only small variations were seen throughout the day of operation. Breakdown occurred at $\sim$ 445 ms, followed by a rapid current ramp to a peak $\sim$ 65 kA at $\sim$ 460 ms, which then slightly decayed over the next $\sim$ 20 ms before an abrupt drop.

These discharges represent an improvement in several aspects of plasma performance over previous LTX discharges, largely due to improved programming of coil currents and fueling. New software had recently been developed to control the IG-BTs modulating the discharge of the capacitor bank, allowing increased bank voltage, longer discharges, and more constant plasma current. The toroidal field power supplies were also run in voltage control mode (as opposed to current control), allowing a modest increase in current and thus toroidal field, though with a small sacrifice in reproducibility as the coil conductivity decreased throughout the day due to resistive heating. The fueling was also adjusted, with reduced fueling early in the discharge (which generally leads to a higher peak plasma current) followed by a large gas puff near the current peak. The large gas puff both boosts spectroscopic signals, improving measurement quality, and allows study of the plasma as the density decays without additional fueling, which is of interest for understanding the low-recycling properties of the Li coatings.

Chapter 3

Thomson Scattering

Thomson scattering (TS) is the elastic scattering of an electromagnetic wave incident on a charged particle, with the effect being far stronger for electrons than ions due to their lower mass. As the scattered light is Doppler shifted by the motion of the electrons, the broadened spectrum of the scattered light is directly related to the velocity distribution of the electrons (and thus temperature T_e). At densities achievable in tokamaks (including LTX), this scattering is incoherent, thus directly proportional to both the intensity of incident light and the number of scattering electrons (and thus for a fixed scattering volume, electron density n_e). The complete non-relativistic formula is given in Equation 3.1 and is derived in [45, 16]

$$N_{pe} = \frac{N_i G \eta T n_e r_e^2 L \Delta\Omega \Delta\lambda}{\lambda_i \sin{(\theta/2)}} \sqrt{\frac{m_e c^2}{8\pi T_e}} \exp{(-\frac{(\lambda - \lambda_i)^2 m_e c^2}{8\lambda_i^2 T_e \sin^2{(\theta/2)}})} \tag{3.1}$$

where N_i is the number of incident photons, G is the detector gain, η is the detector quantum efficiency, T is the systems optical transmission, n_e is the electron density, r_e is the classical electron radius, L is the length of the laser beam imaged, $\Delta\Omega$ is the solid angle of collection, $\Delta\lambda$ is the wavelength band, m_e is the electron mass, λ_i is the wavelength of incident light, and θ is the scattering angle.

Thomson scattering is a very important diagnostic because n_e and T_e (and their gradients) are among the most fundamental parameters for understanding a fusion device. In a quasineutral plasma in thermal equilibrium and with known impurity concentrations, these measurements can determine the fusion power, plasma pressure, resistivity, and collision rate. In a modest-sized ohmic tokamak like LTX, $T_i < T_e$ and must be measured separately. Impurity concentrations must also be determined, though n_e and T_e measurements are necessary for determining emission rates of impurities for spectroscopic measurements of impurity concentrations, as described in Chapter 4. So while Thomson scattering cannot completely characterize the LTX plasma, it measures some of the dominant parameters determining MHD equilibrium and stability, stored energy, collisionality, transport, and confinement time.

This chapter describes the LTX TS system, the steps taken in this work to re-align (under vacuum), reinforce, and recalibrate the hardware, and to improve the analysis software.

3.1 The LTX Thomson scattering system

In general, a Thomson scattering system consists of a high-power laser, optics to collect the scattered laser light, and some type of spectrometer and detectors to resolve and measure the intensity and Doppler broadening of the light [44]. Because the cross section for scattering is so small ($\sim 10^{-28}$ m^2), the laser must be very powerful, and the optics, spectrometer, and detector must be very sensitive and efficient. In addition, tremendous care must be taken to reduce the effects of background light from plasma emission, stray laser light, and other sources of noise that can easily overwhelm the small measured signal.

LTX uses a 4-stage Q-switched ruby laser that emits a 15-20 J beam of light at 694.3 nm in a single pulse with a full-width at half-maximum (FWHM) $\sim$35 ns in
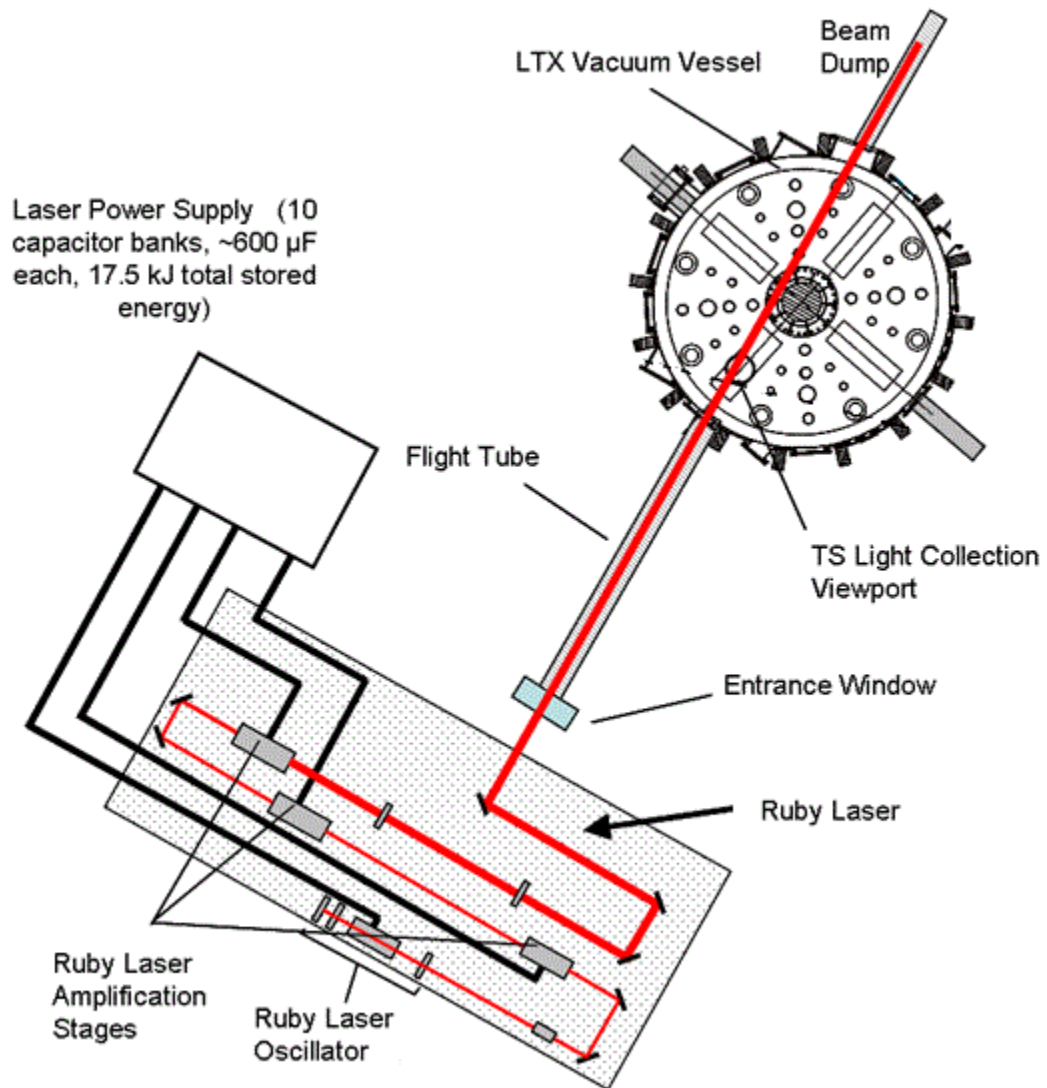
Figure 3.1: Overhead layout of LTX showing the Thomson scattering laser system and laser path. Figure and caption modified from [97].

duration. Many components of the laser were used in earlier experiments on PBX-M [56], though it was significantly enhanced for use on LTX [97, 45]. The layout of the LTX Thomson scattering system is shown in Figure 3.1. The laser is built on an optical table and kept within a light-tight enclosure in the LTX test cell, in which it is fired, amplified, focused, and finally aimed into the LTX vessel. The laser energy is monitored with a ED-500 Gentec Joulemeter. The laser system also includes two 2.5 mW continuous wave He-Ne lasers approximately co-linear with the ruby laser and useful for alignment of the system. After the final steering mirror in the enclosure, the beam passes through a vacuum window, an entrance flight tube, and a toroidal shell gap before coming into focus along a near-radial midplane path in the LTX plasma volume. The beam passes near the center stack and exits through another flight tube and vacuum window into a beam dump made of pieces of blue absorbing glass angled to minimize reflections. Like nearly all vacuum hardware attached to LTX, the flight tubes are mounted on the vessel behind gate valves, which allow removal for maintenance without venting the main vessel. Furthermore, the flight tube gate valves are operated pneumatically by a control box that can automatically close the valves if the vessel pressure rises suddenly, for example if the high laser power fractures a vacuum window.

The scattered light is collected by custom five-element f/3.8 lens set mounted above a vacuum window in the toroidal shell gap midway between the nominal magnetic axis and the outboard edge. A diagram and a photo of the collection optics are shown in Figures 3.2 and 3.3. The window is installed on a gate valve to allow cleaning in case of lithium deposition, with an in-vessel shutter to prevent deposition in the first place. The optics focus light scattered nearly perpendicularly from the laser beam onto 16 high-throughput 800 μm optical fibers that carry the light to the spectrometer. The sightlines from the fibers cover the outer radial midplane from the nominal axis ($R_0 \sim R_{TS} \sim 40$ cm) to near the nominal edge ($R_{edge} \sim 66$ cm,
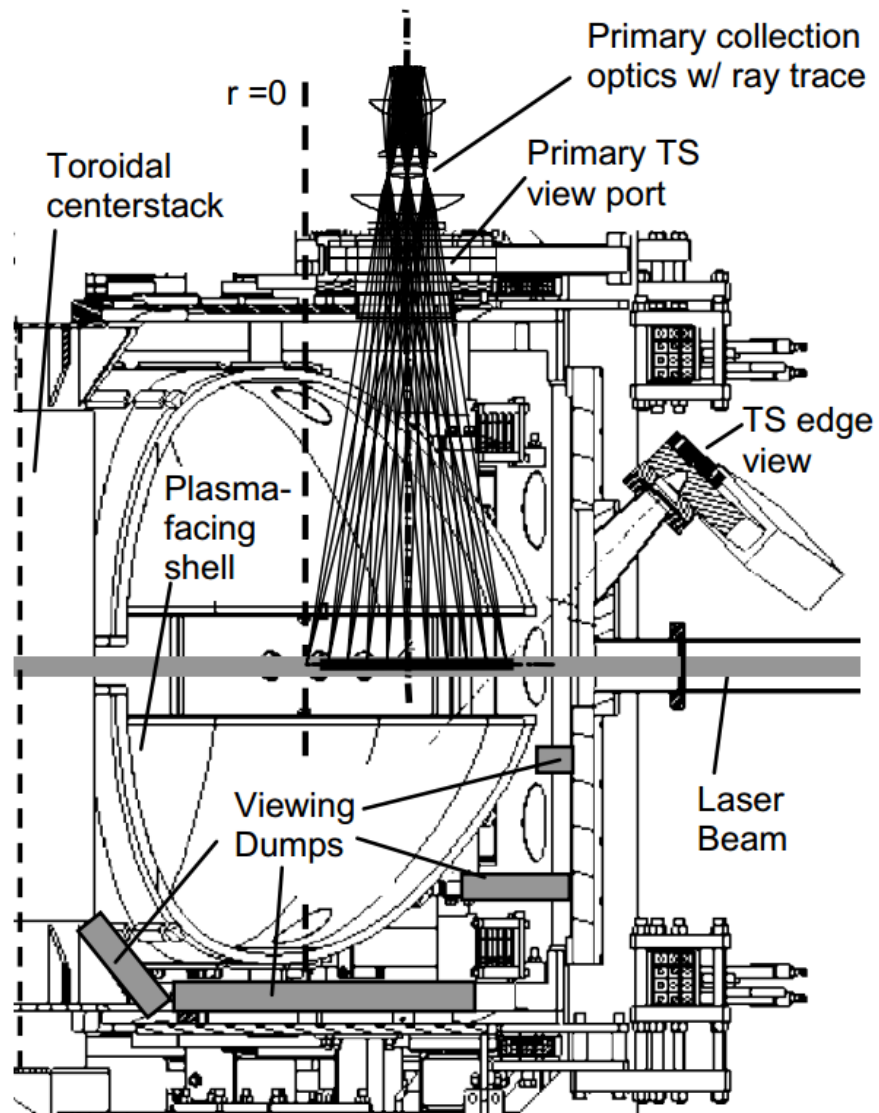
Figure 3.2: Side view LTX cross section showing the TS collection optics and ray trace of scattered light from the laser beam through the primary collection optics. Figure and caption reproduced from [97].
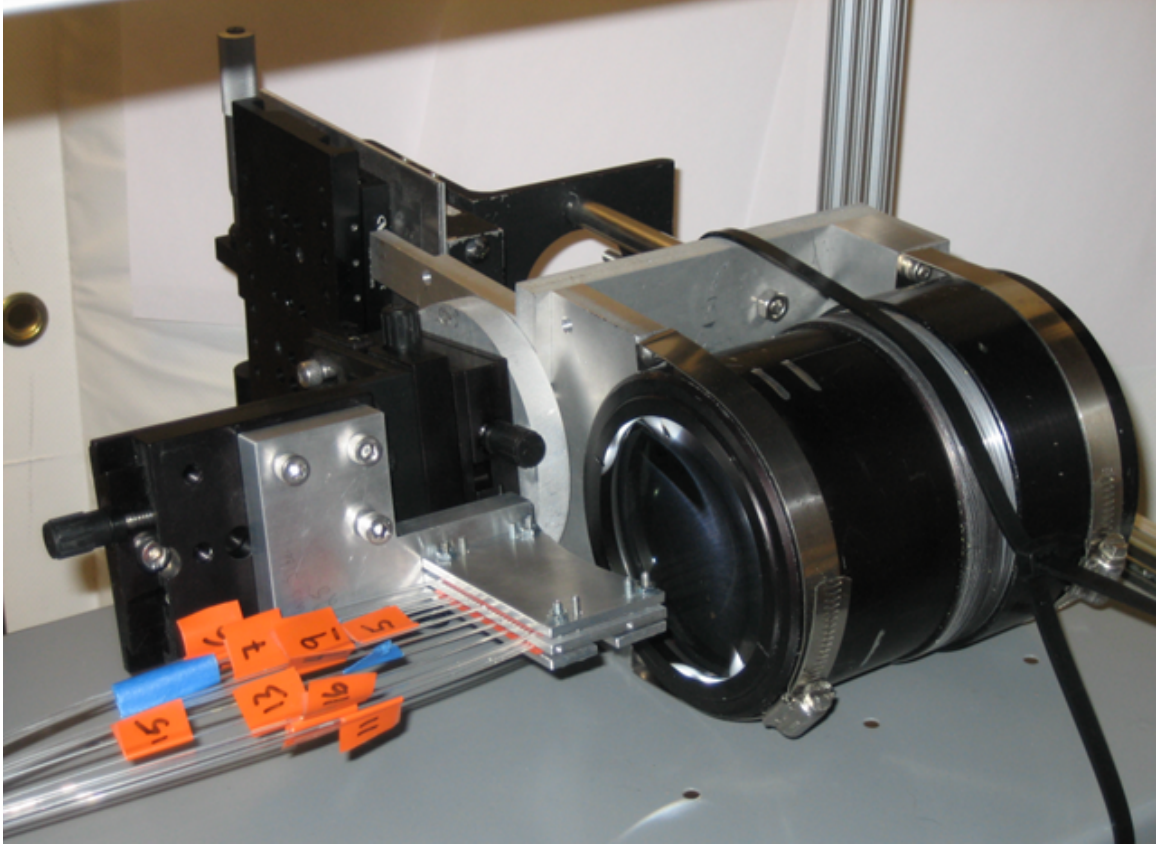
Figure 3.3: TS collection optics and fibers, removed from the vessel for a calibration. Reproduced from [45].

$R_{TS} \sim 64$ cm) with spot sizes of 0.5 cm and resolution 1-3 cm, and terminate on viewing dumps made of stacked razor blades to reduce reflections. The position, size, and scattering angle of the collection volumes was determined during a machine vent by back-illuminating the fiber optics from the spectrometer side and measuring the bright spots projected onto a long ruler inserted along the laser beam path [45].

The ends of the optical fibers are held in a single vertical column in a reconfigurable fiber holder that attaches (and detaches) to the spectrometer. The spectrometer is a f/1.8 Kaiser Holospec VPT System previously used on CDX-U [78, 79], though reconfigured for LTX to use a low-dispersion (rather than high-dispersion) holographic transmission grating so that higher temperatures can be measured. Light from the fibers passes through two Kaiser Optical Systems notch filters to block scattered

Figure 3.4: An image of the interior of the spectrometer. A metal cover has been removed for the photo. The fiber holder is normally connected to the right side of the spectrometer. Figure and caption reproduced from [45].

laser light and H-alpha emission from the plasma before a 800 μm entrance slit. The spectrometer uses a 85 mm f/1.8 entrance lens and a 58 mm f/1.2 exit lens to demagnify the image, increasing signal to noise and the wavelength range ($\sim$550-760 nm) of the detector. 11 fibers can be imaged on the detector, and the highest and lowest fibers imaged on the detector are significantly vignetted. Illuminating the optics with a monochromatic light source produces an image on the detector of the vertical column of fibers, with the horizontal position of the image depending on the wavelength. Light from a broadband source is dispersed horizontally according to wavelength, forming horizontal bands on the detector. The vertical separation

between the band for each fiber is due to the fibers' separation in the fiber holder, and the vertical extent of the band corresponds to the height of the image of the fiber.

The detector is a Princeton Instruments PI-MAX Intensified CCD (ICCD) camera with a 512x512 array of 19x19 μm pixels. It has a Gen IV intensifier with effective quantum efficiency $\sim 15\%$ [79] and can gate light at a ratio of $\sim 10^6 : 1$ with a 2 ns gate width. Timing is controlled with a Stanford Research Systems Digital Delay Generator (DG-535) with 5 ps precision and 50 ps maximum jitter. In these experiments a 100 ns exposure was used to ensure scattered light was collected from the entire (~ 35 ns FWHM) laser pulse, and to allow for jitter in the laser timing. As "salt-and-pepper" noise due to hard x-rays was frequently seen on various cameras in and around the LTX test cell, including the TS camera, iron blocks and lead sheets were placed between the TS camera and LTX.

3.2 Re-alignment of the TS system

While this system was operated successfully on LTX in 2011-2012, in 2013 the camera malfunctioned and circuitry within the camera had to be repaired [45]. After re-installation, the camera operated normally but it was later found that the system was not recording scattered light, but only stray and plasma light. A change in timing due to the repair was initially suspected. The camera is controlled by a PC in the LTX control room running WinSpec software, and a GPIB/fiber link was added to allow WinSpec to control the timing as well. In order to automate data acquisition, Visual Basic software originally written for the HAL spectrometer (Section 4.2) was adapted for the TS system to control the camera through WinSpec and write the data to the MDSplus tree. These improvements greatly simplified examination of the timing issue, which was found not to be causing the problem. The next suspect was a polarizer placed on the viewing window under the collection optics, which would
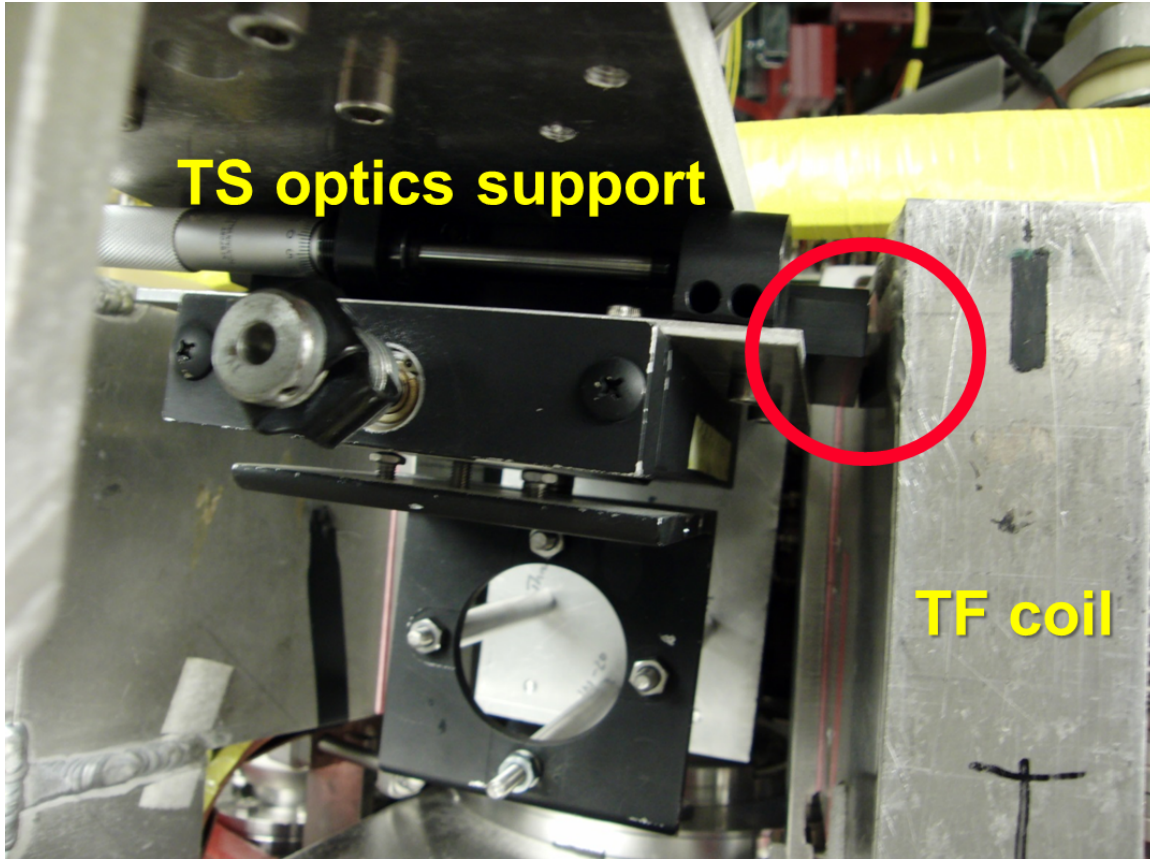
Figure 3.5: TS optics assembly in contact with toroidal field coil before re-alignment.

reduce the generally unpolarized stray and background light by ~50% while only slightly affecting the polarized scattered light. On the off chance that the polarizer was in the wrong orientation and blocking the scattered light, it was removed. This did not fix the problem, but the polarizer was found to be water damaged and was not re-installed.

Finally, it was determined that the viewing optics were out of alignment with the laser beam and would need to be re-aligned. Most likely, this was due to lack of rigidity in the support structure for the viewing optics, which were mounted on a translation stage at the end of an arm protruding from a vertical post anchored to the floor. While various support rods kept the structure fairly rigid in most directions, the horizontal motion of the optics was only held rigid by a pair of guy wires. While this could have been effective in principle, in practice one of the guy wires was attached to

wood paneling that came loose after being under tension from the wire. Both wires were positioned such that they were prone to being bumped when work needed to be done on top of the machine. In fact, the support structure had shifted to be in physical contact with one of the toroidal field coils, as seen in Figure 3.5with the guy wires no longer keeping the support a few mm away from the coil. A few attempts to put the system back into alignment by wedging materials of varying thickness between the support and the coil did not succeed in realignment of the system that was sufficient to measure scattered light.

Rather than re-align a system that was not mechanically robust, a decision was made to redesign and reinforce the support structure for the optics. Furthermore, the support structures for the laser entrance and exit flight tubes were lightweight Unistrut and easily bumped out of position, potentially allowing the laser beam to be clipped by an unintended surface, creating excess stray light. Thus, rigid structures for the flight tubes were built from 80/20 aluminum and anchored to the floor. A triangular brace was added to the vertical post from the floor to prevent horizontal motion of the optics, which were fixed in place close to their existing position but away from the TF coils. The vertical post also was bolted to a new vertical post attached to the ceiling I-beam for additional stiffness.

Once the system was reinforced, it was necessary to re-align the laser to the viewing sightlines. Normally, a laser alignment would be performed during a machine vent. Notably, this realignment had to be performed without breaking vacuum, otherwise a lengthy Li cleanup and vacuum conditioning process would have been required. An in-vessel target was constructed so that the He-Ne alignment laser and back-illuminated optical fibers could project light onto the same 45° angled target, and the laser could be adjusted until both light beams coincided. The target was built from aluminum and screwed into the threaded end of a long 1/4" stainless steel rod, which was fed through a differentially-pumped Wilson seal mounted on a 2-D tilt
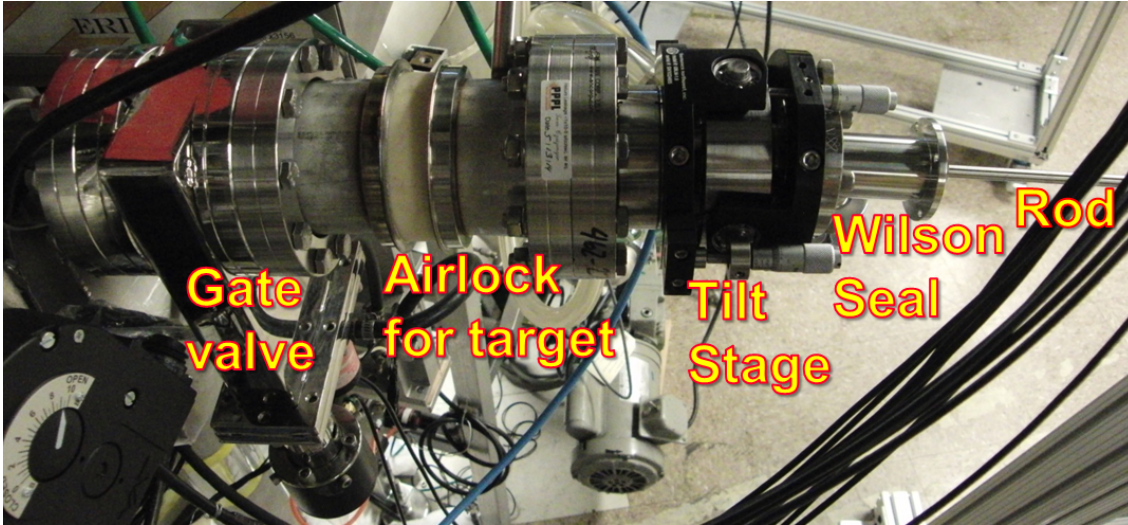
Figure 3.6: Re-alignment target assembly installed on vessel (top), and support rod on shell (bottom).
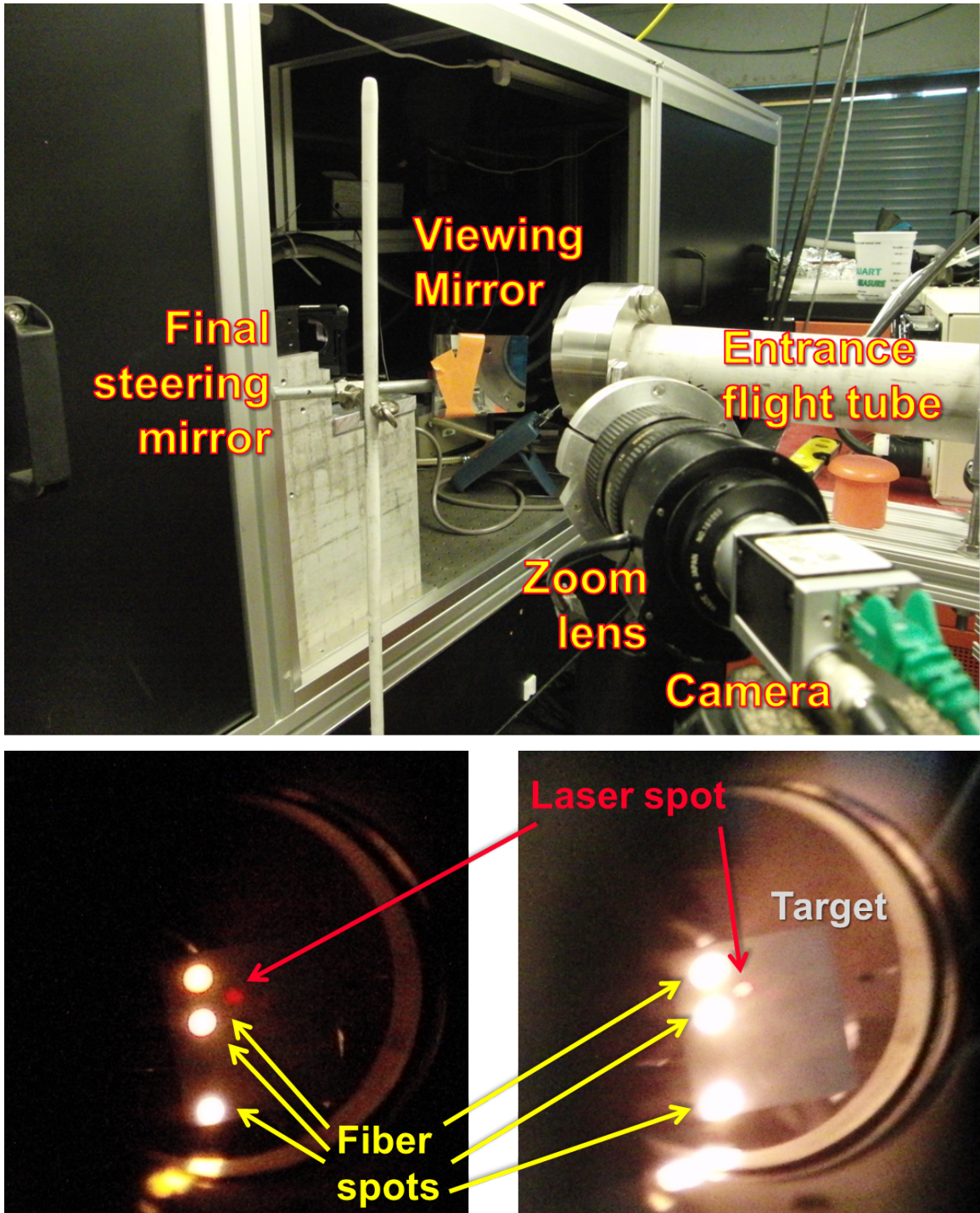
Figure 3.7: Camera and mirror for viewing re-alignment target; final steering mirror also visible in enclosure (top). Fiber and laser spots on target (bottom).

stage (Figure 3.6, top). The target apparatus was then mounted on the laser exit gate valve in place of the exit flight tube, so that the target could be inserted along the path of the laser beam. In order to counteract the sagging of the long, thin rod, an additional support rod was inserted perpendicular to it (Figure 3.6, bottom). The support was also built from aluminum with a ramp to slide up and rest on the inboard lip of the lower south shell quadrant, and had a rounded Teflon top so the target rod could slide easily over it. The support was also screwed into the threaded end of a 1/4" stainless steel rod fed through a differentially-pumped Wilson seal, mounted on a 1-D tilt stage with only up-and-down motion. A mirror was placed between the laser enclosure and the entrance flight tube so that a Basler GigE camera with a zoom lens could view the laser and fiber spots on the target (Figure 3.7). Using the micrometer-adjustable translation and rotation stages of the final steering mirror, the laser was aligned to best coincide with the farthest inboard and farthest outboard sightlines. The alignment target and support were then removed and the exit flight tube put back in place.

As the HeNe laser was not precisely aligned with the ruby laser, the final alignment was determined by filling the vessel with argon so Rayleigh scattering measurements could be made. This required removal of the ruby filter that would otherwise block the unshifted scattered light and reduction of the intensifier gain to avoid saturation of the detector. Raman scattering from a diatomic gas like nitrogen would have allowed the ruby filter to remain and reduce the effect of stray laser light, but was not possible as the nitrogen would contaminate the Li coatings in the vessel.

The best alignment was determined by adjusting the angle and translation of the final mirror and finding the settings that gave the strongest scattered light signal over all the sightlines. The best alignment was found with the mirror translated to the end of its travel in one direction, indicating a better alignment would be possible with

further translation. However, it was decided to see if useful plasma measurements could be made before making additional modifications.

While there did appear to be measurable amounts of Thomson scattered light collected on the detector, signal levels were low, indicating imperfect alignment. Furthermore, high levels of stray light were making it past the ruby filter and appearing on the detector, complicating analysis and further reducing signal to noise. Extensive efforts to reduce reflections in the system were undertaken. Some clipping of the laser spot was observed in tests with burn paper, so baffles in the flight tubes with apertures that may not have been large enough were removed. An aperture was added in the laser table after the final amplification stage to block unwanted light around the periphery of the beam. Burn paper was placed throughout the laser table to detect stray light, and absorbing material was placed anywhere the burn paper or alignment lasers indicated stray light could fall. Black burn paper was used to cover the exit of the laser table and entrance of the beam dump and exposed to a laser pulse. The burned sections were then cut away, leaving apertures only big enough for the beam.

After these efforts to reduce stray light proved insufficient, it was suspected that the collection sightlines were terminating on a reflective surface such as the shell rather than the dark viewing dumps below the shell gap. This was confirmed by back illuminating the optical fibers, as most of the spots indeed fell on the shell or one of the shell flux loops (Figure 3.8). This also explained why the laser could not be perfectly aligned, as the sightlines were too far from their original positions. Furthermore, the extreme adjustment to the laser path to compensate may have led to the beam being clipped slightly by edge of the port where it exited. To remedy this, the in-vessel target was re-installed, and the alignment procedure was repeated, with the additional step of repositioning the viewing optics so that the sightlines terminated on the viewing dump and the laser was not clipped by the exit port. The support structure had sufficient degrees of freedom to realign the optics, though
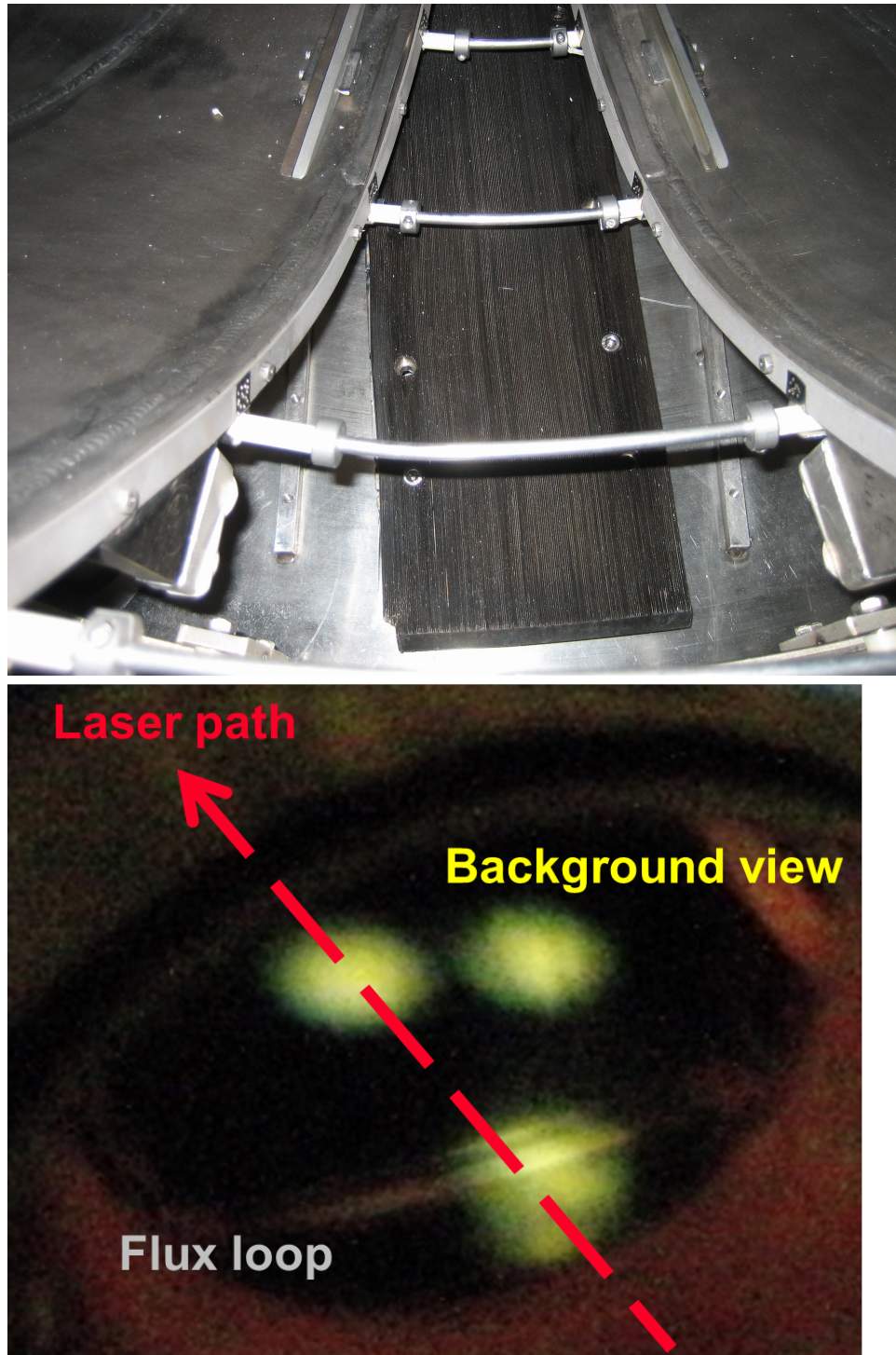
Figure 3.8: TS viewing dump and flux loops in lower shell gap at installation (top), and viewed through the TS edge view port using a mirror (bottom), with illuminated fibers projecting spots on the dump and one partly intercepting a flux loop. A TS background fiber viewing to the side of the laser path is also illuminated.

some minor modifications were necessary to make them correspond to an intuitive, orthogonal basis. Also, it had earlier been determined that the HeNe laser injected into the system before the first amplifier stage was, in fact, very well aligned with the ruby laser, though its spot was much dimmer than the less well aligned HeNe laser injected before the third amplification stage. Thus, by using the dimmer but better aligned laser for alignment with the viewing optics using the in-vessel target, it was not necessary to further improve the alignment with Rayleigh scattering in an argon-filled vacuum chamber. Stray light was greatly reduced and TS measurements were able to be made, though significant stray light remained in some of the channels.

3.3 Recalibration of the TS system

When the LTX TS system was developed, software was written in IDL to analyze the data and is described in detail in [45]. The software converted the camera images to calibrated spectra for each fiber, and then fit each spectrum with the Thomson scattering function to determine n_e and T_e, taking into account background plasma light, stray laser light, the effects of the notch filters and spectrometer optics. In this work, significant modifications were made to improve both the calibrations used in the analysis and the analysis software itself.

In order to convert the measured detector counts into a number of Thomson scattered photons, the TS system was absolutely calibrated using a LabSphere URS-600 Uniform Radiance Standard, of which the absolute output luminosity is known. When the TS camera was repaired, however, the earlier calibrations were no longer preserved. Recalibrating the full system would have meant removing the optics from the vessel and then re-installing and re-aligning them, which was not considered practical. Instead, the earlier calibration was transferred to the repaired camera by detaching the fiber holder and shining the LabSphere directly into the spectrometer

before and after the camera repair. It was found that the detector was shifted by approximately 5 pixels horizontally and 24 pixels vertically [45].

The pixel-to-wavelength calibration of the detector was also redone after the camera repair using a H lamp and fitting the spectrum to a simple function assuming constant dispersion and constant circular image curvature [45]. In spectra from LTX plasma line emission, however, there were small discrepancies between the measured wavelengths and their known values. This discrepancy did not have a significant direct impact on measurements of density and temperature, but was important for properly subtracting off plasma line emission and stray laser light. In order to most accurately calibrate the wavelength, spectra from numerous plasma discharges (without firing the laser) were averaged to increase signal to noise and make use of the several emission lines in the spectrum. The dispersion and curvature were determined more accurately by fitting to a function that fully incorporated the geometry of the spectrometer [8] and allowed for small deviations in the position of each optical fiber in the holder. This calibration gave a much tighter fit to the data and more precise determination of the wavelength of plasma emission lines. An accurate wavelength calibration is most important for fitting low T_e spectra with less broadening away from the laser line.

Another important calibration for subtracting off line emission and stray laser light was the instrument function describing the apparent broadening of line emission due to the optical elements of the spectrometer. In the original analysis, this was characterized with a top-hat function convolved with a Gaussian, with parameters chosen based on the slit width and fits to calibration lamp spectra, respectively [45]. This was sufficient for removing the instrumental broadening from the larger temperature broadening being measured, but did not fully match the plasma emission lines that were being fit and subtracted off. During the laser alignment using Rayleigh scattering in the argon-filled vacuum vessel, a large number of measurements were

taken of the single narrow laser line. The broadening of the laser line was solely due to the instrument function, and averages of the numerous measurements gave spectra for each fiber with high signal to noise and no competing lines. The broadened lines could be well fit with 2 to 4 summed Gaussian functions, but ultimately the averaged spectra themselves were taken as discrete numerical representations of the instrument functions.

3.4   Improved analysis of TS data

In addition to the improved calibrations, the analysis software was improved in several ways. One improvement was using a more complete approximation to the Thomson scattering function (Equation 3.2) that included relativistic effects [92] rather than assuming a non-relativistic Gaussian function (Equation 3.1). This was a minor improvement given $T_e < 300$ eV, but straightforward to apply.

$$N_{pe} = N_i G \eta T n_e r_e^2 L \Delta\Omega\Delta\lambda \frac{c(\alpha)}{A(\epsilon,\theta)} \exp[-2\alpha B(\epsilon,\theta)] \tag{3.2}$$

$$A(\epsilon,\theta) = (1+\epsilon)^2 \sqrt{2(1-\cos\theta)(1+\epsilon)+\epsilon^2} \tag{3.3}$$

$$B(\epsilon,\theta) = \sqrt{1+\epsilon^2/[2(1-\cos\theta)(1+\epsilon)]} - 1 \tag{3.4}$$

$$c(\alpha) = \sqrt{\alpha/\pi}(1 - \frac{15}{16}\alpha^{-1} + \frac{345}{512}\alpha^{-2} - ...) \tag{3.5}$$

$$2\alpha = m_e c^2/T_e \tag{3.6}$$

$$\epsilon = (\lambda/\lambda_i) - 1 \tag{3.7}$$

Another minor improvement was in the method of binning pixels. As the images of the fibers on the detector were several pixels tall, it was necessary to sum the pixels vertically to give a simple function of intensity versus wavelength. This summation was complicated by the curvature of the image due the short focal length of the

spectrometer, which means vertically adjacent pixels do not have the same central wavelength. Previously, an array of equally spaced wavelength bins was created and then all of the pixels in the image were binned according to their central wavelength. As the wavelength bin width (1 nm) was not an integer multiple of a pixel width (0.42 nm), this meant some bins included more pixels than others. While suitable averaging meant this did not cause any large discrepancies, it did cause small variations in line broadening and meant some bins differently sampled the vertical variations in intensity and line broadening. Furthermore, the bins used were 2-3 pixels wide, causing unnecessary additional line broadening. While binning the pixels together horizontally improved signal to noise, this was unlikely to improve the fits, which already took into account the statistical noise. A new binning method was therefore written that would shift the rows horizontally to minimize the effect of curvature prior to binning each column. Therefore each bin was a single pixel wide, avoiding broadening spectral lines more than necessary.

Improving the way plasma line emission and stray laser light were subtracted out was another important modification to the analysis. In earlier experiments, stray laser light was not a significant problem and could be ignored, as the part of the spectrum near the notch filter at the ruby wavelength was excluded from the analysis anyway [45]. In the new measurements, stray light was significant in several channels, and contaminated the measured spectrum beyond the excluded region around the ruby notch filter due to the wide instrument function. The improved calibration for the instrument function (and to a lesser extent the improved binning method) made it possible to fit and subtract the stray light sufficiently well that reliable fits were again possible. The stray laser light was fit and subtracted before the absolute calibration was applied to the raw spectrum, as the absolute calibration in the regions near the notch filters was distorted by the interaction of the filters and the instrument function.
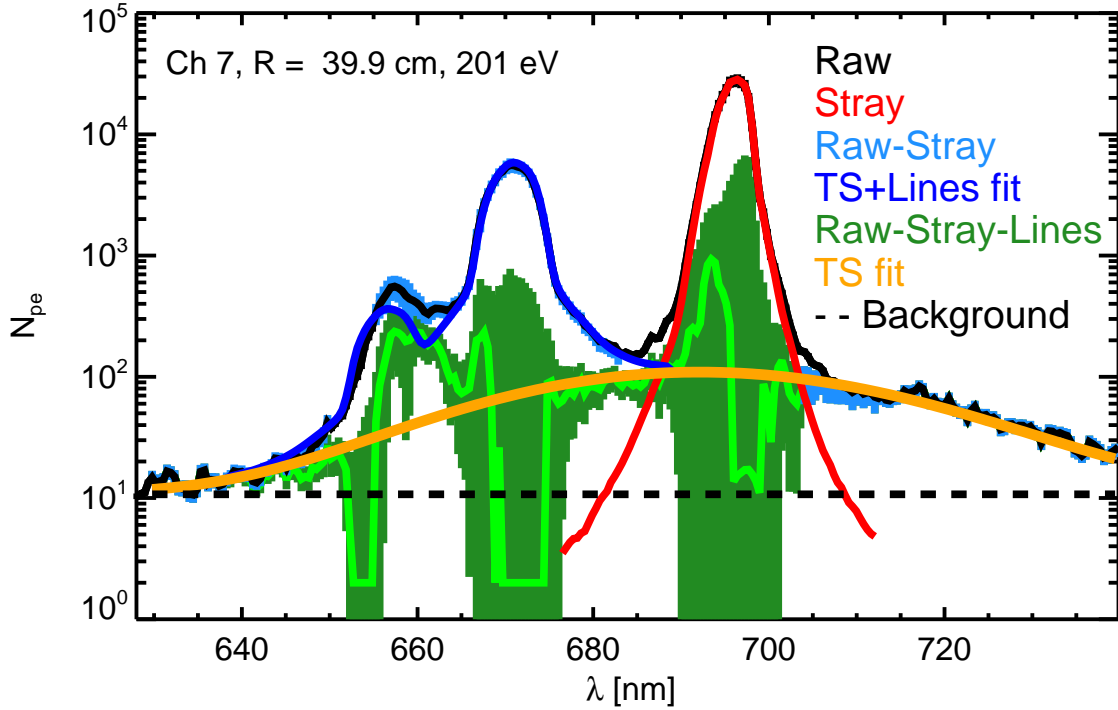
Figure 3.9: Thomson scattering spectrum with fits from the innermost view for 8 averaged shots with average t = 469.75 ms. The binned, calibrated spectrum is shown in black, the fit to the stray laser light is shown in red, the stray light subrtracted spectrum and error bars are shown in light blue, the fit to the Thomson scattered and plasma line emission spectra after stray laser light subtraction are shown in blue, the stray light and line emission subtracted spectrum and error bars are shown in green, the fit to the TS spectrum is shown in orange, and the constant offsets from the fits are shown as a black dashed line.

In the previous analysis [45], the Li I line at 670 nm was fit simultaneously with the TS spectrum, though the region immediately around the peak of the line (where the TS signal was small relative to the photon noise in the line emission) was excluded from the analysis. This exclusion allowed the fit to best match the "wings" of the line, where the intensity of the TS light was comparable to the line emission, and was necessary due to the shortcomings of the instrument function as described in section 3.3. By using a better calibration for the instrument function and a better binning method that avoided additional distortions, it was possible in the new analysis to fit the Li I line emission well without excluding the region around the peak. As before,

the Li I line was fit simultaneously with the TS spectrum, and parts of the spectral regions within the notch filters were excluded from the fit.

Another important improvement to the analysis was the use of averaged spectra from multiple repeated discharges to increase signal-to-noise and give more robust fits. As the noise in the measurements is largely governed by Poisson statistics, the signal-to-noise ratio increased by the square root of the number of averaged discharges. In the experiments described in section 2.3, the same TS measurement time was used for 3-5 discharges, and the raw CCD images of the spectra were averaged before analysis. Still more improvement was achieved by averaging spectra for each time point with their nearest neighbors in time, with the effect of smoothing the data in time. The time for the averaged measurements were set at the weighted average of the times used.

3.5   Processing of the TS profiles

As a result of the previously described improvements, the analysis routines produced generally reliable fits, though some additional processing was needed to ensure the TS profiles were well-behaved for the analyses in the rest of this work. The TS fitting routines automatically marked data as invalid if T_e was not within 5-500 eV or had error > 60%. For the measurements and analysis in this work, additional criteria were used to exclude unreliable data. The vignetted channel at the bottom of the CCD still appeared to have a calibration error, as it consistently showed lower density than its neighbors in the plasma core. The three farthest outboard channels only met the basic validity criteria at a few time points, and in some of those showed improbable (or even implausibly large) increases in T_e and/or n_e with increasing radius. These points were excluded entirely from the analyses in the rest of this work. The fourth most outboard channel was generally reasonable except for a few implausibly large

increases in T_e, which were excluded. Finally, points with $T_e > 300$ eV were excluded as they had large uncertainty and only occurred near the edge. Note that even in the core, $T_e < 250$ eV.

As in the previous LTX TS analysis, uncertainty weighted smoothing splines were used to interpolate and smooth the TS profiles [85]. In this work, the (almost entirely low-field side) valid TS data points were first mapped across the magnetic axis using equilibrium reconstructions (Section 2.2.1). To keep the profiles well-behaved, an additional point at $R = 66$ cm was included with $n_e = 10^{10}$ cm^{-3}, $T_e = 10$ eV, and uncertainties equal to the farthest outboard valid point. These values were also enforced as minimum values for the smoothed profiles. Uncertainties in the spline fits were calculated with a Monte-Carlo method varying the profiles within their error bars. For compatibility with other measurements, the spline-smoothed TS profiles were linearly interpolated in time to a uniform timebase using an uncertainty weighted average. For measurement Y with uncertainty σ_Y, first the interpolated uncertainty σ_y was found by interpolating $1/\sigma_Y^2$ and taking the inverse square root. The interpolated measurement y was found by interpolating Y/σ_Y^2 and multiplying by σ_y^2.

One difficulty of the earlier TS analysis was that the LabSphere absolute calibrations did not completely match calibrations with Rayleigh and Raman scattering, nor did TS measurements of the n_e profiles completely match the more robust line-integrated density measurements from the 2 mm interferometer [45]. Furthermore, only two discharges had both interferometer measurements and TS profiles, and the cross calibration factor calculated from each discharge differed 15% from their mean. In the present analysis, there was also a discrepancy between the TS n_e profiles and the 1 mm interferometer line densities. The interferometer (section 2.2.2) has been making reliable measurements throughout the most recent experimental campaign, including all of the discharges described in section 2.3. As described in Section 2.3, the median of the line-integrated density measurements for all the discharges was
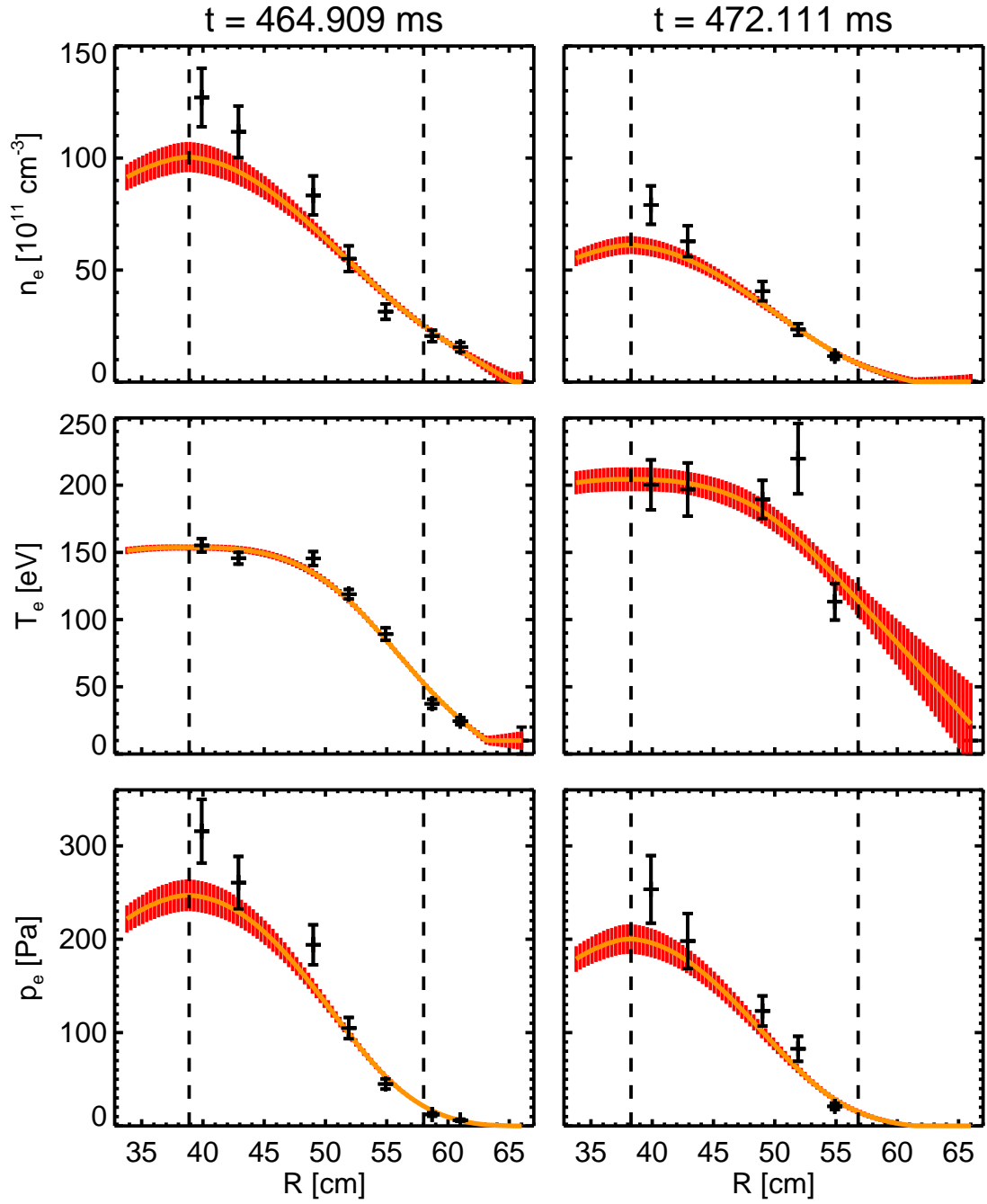
Figure 3.10: TS n_e, T_e, and p_e profiles (black) and smoothing spline fits (red) during the peak of the gas puff (left) and after fueling ceased (right). The magnetic axis and LCFS from magnetic reconstructions are shown as vertical dashed lines. Note the flattening of the T_e profile after fueling ceased with high temperatures all the way to the reconstructed edge, suggestive of low-recycling as discussed in section 5.1.
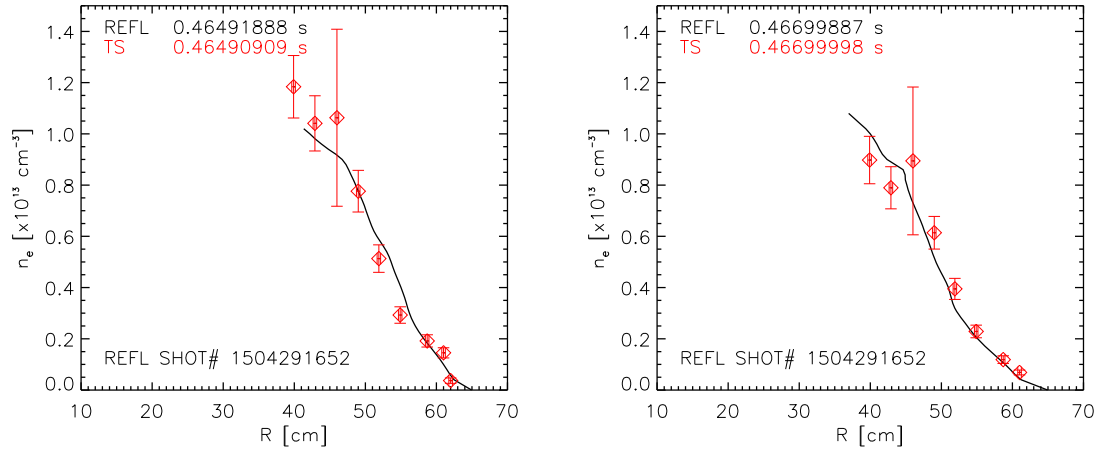
Figure 3.11: n_e profiles from reflectometer (black curve, reflectometer discussed in section 2.2.2) and TS (red diamonds, corrected with interferometer) show good matches.

calculated, then boxcar smoothed and downsampled to the same uniform timebase as the interpolated TS profiles. In order to cross-calibrate the TS measurements, the interpolated TS density profiles were numerically line-integrated and re-normalized to the smoothed median interferometer waveform. The normalization factor was quite stable within a standard deviation of 13%. Furthermore, the TS n_e profiles, when adjusted to match the interferometer, also gave an excellent match to profiles from the reflectometer, as shown in Figure 3.11.

Chapter 4

Impurity spectroscopy

Impurity spectroscopy measures line emission from impurity ions and uses its intensity to determine the amounts of impurities in the plasma [44]. Visible light is collected by lenses and transmitted by optical fibers to a spectrometer (in this work, one with novel design) and recorded by a detector. With proper calibration of the spectroscopic system, the measurements can be analyzed to calculate the line emission profiles. By combining the emission profiles with electron density and temperature measurements, as well as known emission rates, density profiles of the various impurity species can be determined. This is the key measurement in fulfilling the objectives of this work, determining the levels of impurities in a tokamak with full Li coatings on metal PFCs and understanding the impurity transport.

4.1   Impurity line emission

Line emission is produced when an electron, bound to an atom, is excited to a higher quantum energy level and then relaxes, emitting a photon that carries energy equivalent to the difference between the excited and relaxed states. The possible energy levels and the transition rate of the excited electron to the various possible lower energy states is determined by atomic structure and ionization state of the atom. In

LTX plasmas, the ionization state is largely determined by collisions with free plasma electrons that have enough energy to eject bound electrons from the atom. As the electron density and temperature increase from the edge to the core plasma, these collisions become more frequent and more able to provide the higher energies necessary to bring impurities to high ionization states. In many larger, hotter tokamaks, impurities are fully ionized in the core and no longer have bound electrons to produce line emission, so impurity spectroscopy requires charge exchange (typically with neutral hydrogen atoms from beam injection) and/or recombination processes to allow the ions to capture electrons for charge exchange recombination spectroscopy (CHERS). In LTX, impurity ions with bound electrons exist throughout the plasma volume, and spectroscopic measurements can be made without a neutral beam. However, the non-localized nature of this emission presents additional challenges in analysis, as will be described in section 4.4.

While atoms can be excited by various means, in LTX plasmas they are typically excited by the same electron impact collisional process that causes ionization, except the collisions have lower energy and do not remove bound electrons. The probability of an electron in a given atom being excited to a given energy level and then emitting a photon with a given energy per unit time has a complex dependence on the atomic species, its initial ionization state, and the density and temperature of the plasma electrons. These probability rates, called photoemissivity coefficients (PECs), have been calculated for a wide variety of possible atomic transitions over large ranges of n_e and T_e and stored in databases, such as ADAS [98]. By using the ADAS database and the TS profiles to calculate the PECs of their atomic transitions, the densities of various impurities can be determined from measurements of their line emission.

The photons carry important information about the impurity ions, and with some basic assumptions, the main ion species as well. The average velocity of the impurities produces a Doppler shift in the wavelength of the line emission, while the

temperature causes Doppler broadening of the line. Doppler spectroscopy is based on spectrally resolving line emission from plasma ions in order to measure their velocity and temperature. Emission from an ion moving toward (away from) the collection optics will be shifted to shorter (longer) wavelength; thus the spectral emissivity is directly related to the ion velocity distribution function. The mean wavelength shift of the emission gives the fluid velocity of the ion species, while the width of the line gives the ion temperature.

With a light impurity species like lithium, it is usually valid to assume the main ion species has the same average velocity $v = v_H = v_{Li}$ and temperature $T_i = T_H = T_{Li}$. From the absolute intensity of the line emission, plus n_e, T_e, and the ADAS coefficients, the impurity density n_{Li} can be determined. For multiple impurity species each with charge Z_Z, the main ion density is given by $n_H = n_e - \sum_Z Z_Z n_Z$, ion pressure $p_i = n_i T_i = (n_H + \sum_Z n_Z) T_i$, and total pressure $p = n_e T_e + n_i T_i$. With these measurements and a magnetic equilibrium reconstruction, force balance on a single species (the impurity) gives the radial electric field $E_r = -(v \times B)_r + p'_{Li}/Z_{Li} e n_{Li} = v_{tor} B_{pol} - v_{pol} B_{tor} + p'_{Li}/Z_{Li} e n_{Li}$.

4.2 The LTX spectroscopy system

An impurity spectroscopy system consists of collection optics, a spectrometer, and a detector. A TS system is based on the same basic components, but Thomson scattered light is only collected from the small volume where the laser beam and a viewing sightline intersect, and each sightline provides an independent local measurement. In a properly design CHERS system the collected emission is mostly localized to the intersection of the neutral beam and a viewing sightline, though the sightline also collects background emission over a large portion of the plasma radius. In a passive system as used on LTX, no single sightline can provide an independent local

measurement, but measurements from an array of sightlines can be tomographically inverted to calculate profiles of local emissivity [7].

LTX has two optical arrays, one on radially viewing ports above and below the vertical midplane, sensitive to poloidal rotation, and the other on a tangentially viewing port at the midplane sensitive to toroidal rotation. The poloidal array has 6 up-down symmetric pairs of views installed on 4 ports using individual Ocean Optics 74-ACR Acromat compact collimating lenses for each view, shown in Figure 4.1. These same lenses were used in the initial LTX toroidal and poloidal arrays, which respectively had 6 tangential views and 5 up-down symmetric pairs of vertical views [33]. Both systems were upgraded in the course of this work, though the analysis is based solely on the toroidal array, which requires only an assumption of axisymmetry for inversion.

The present LTX toroidal array is based on hardware from the Edge Rotation Diagnostic, originally developed for NSTX [15]. The toroidal array uses a single 85 mm f/1.8 Nikkor commercial camera lens to image light onto fifteen 600 μm diameter, 15 m long, 0.37 NA plastic-clad silica fibers, shown in Figure 4.2. In order to maximize radial coverage, a new front mounting plate was designed to place the lens at the far edge of the vacuum window. The toroidal array was also moved to the BC midplane tangential port between the B and C toroidal field coils. The axis of the port is tangent at larger major radius than the port used for the initial toroidal array. This allowed radial coverage from a major radius of $34 < R < 58$ cm, corresponding to nominal normalized minor radius $-0.24 < r/a < 0.68$, shown in Figure 4.1. At their tangency radii, the sightlines are $\sim$0.6 cm in diameter and have $\sim$1 cm spatial resolution nearest the plasma edge and $\sim$2 cm in the core. The bare ends of the fibers are held in a curved fiber holder, while the other ends are SMA-terminated and connect to patch panels in a diagnostic room outside of the test cell. The patch panels give the system
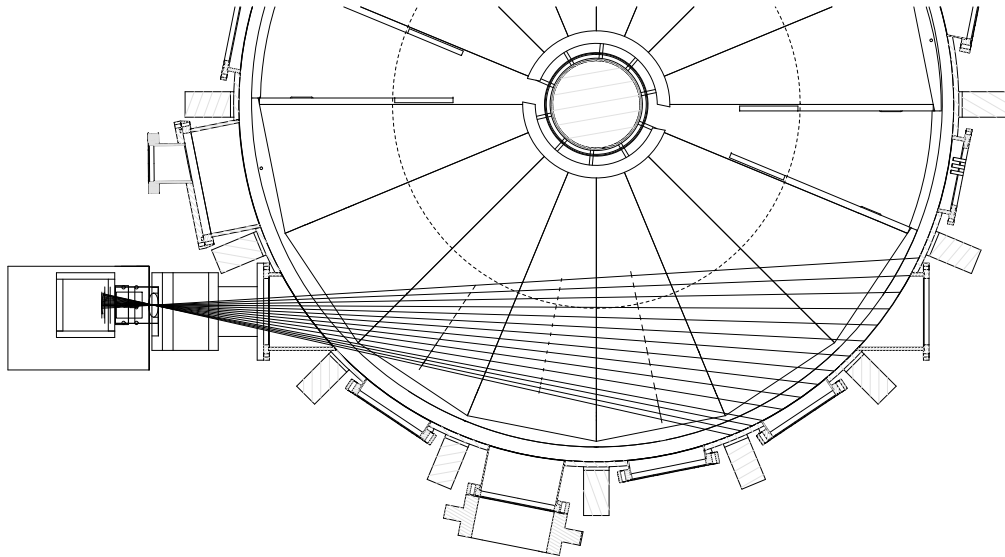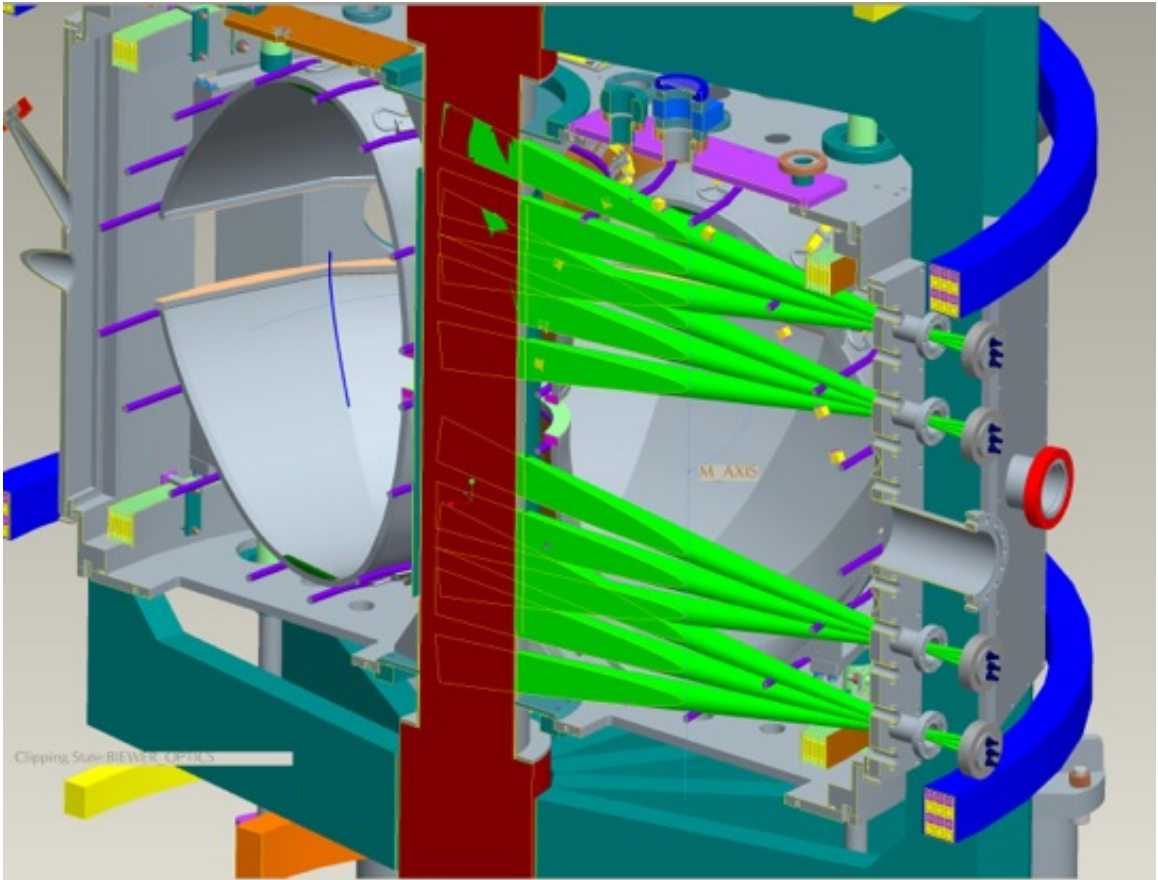
Figure 4.1: CAD models of poloidal views (top) and toroidal views (bottom). In the bottom figure, the dotted circle shows the nominal magnetic axis $R_0 = 40$ cm.
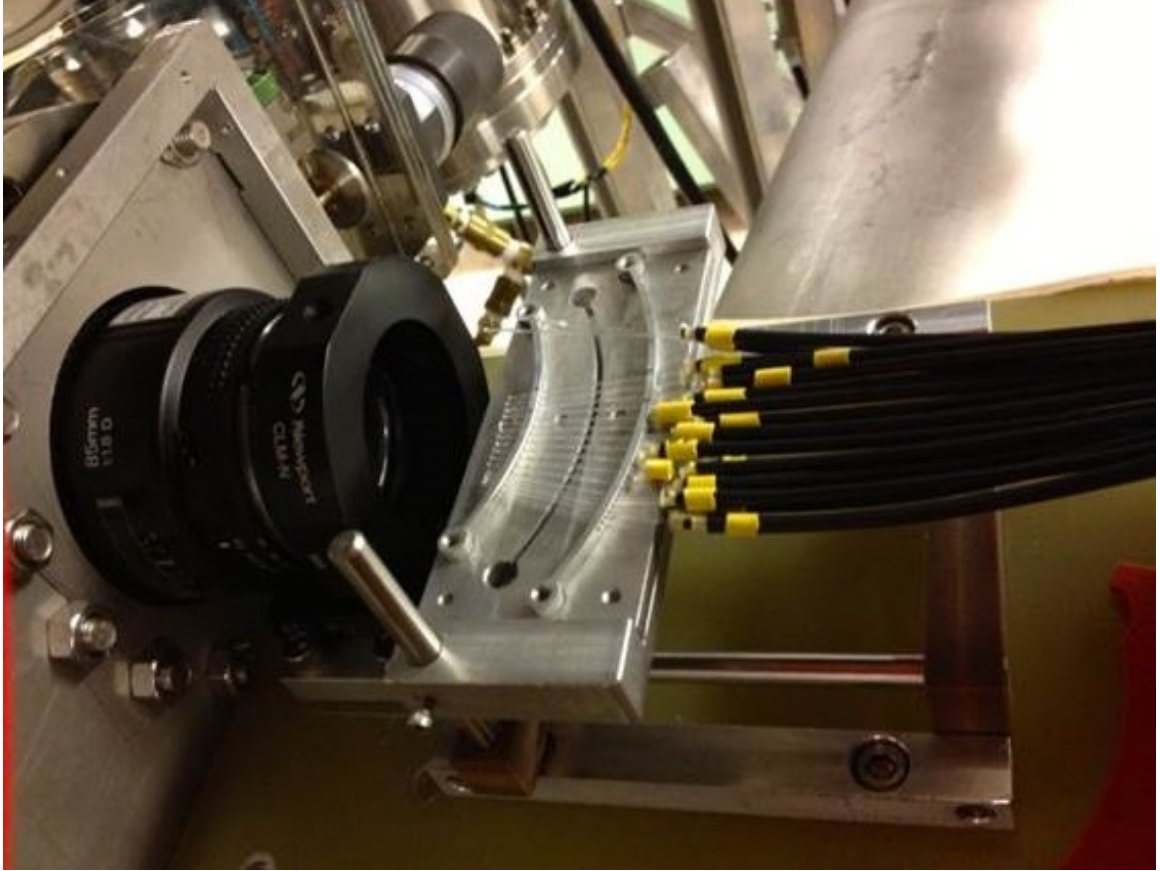
Figure 4.2: Toroidal collection optics, based on NSTX Edge Rotation Diagnostic [15].

flexibility in the ability to easily connect and disconnect different views to different spectrometers.

The poloidal array and one core-viewing fiber from the toroidal array are connected to a Kaiser Optical Systems Holospec f/1.8 short focal length spectrometer with a high dispersion, holographic transmission grating/prism combination with central wavelength 5175 Å. This same spectrometer was used for the initial LTX toroidal and poloidal system [33], and the grating was originally used in the NSTX Li-CHERS diagnostic [82]. The spectrometer covers the spectral range ∼5090-5190 Å, which contains several C II lines and the Li III n=7-5 transition line at 5166.89 Å. The spectrometer is connected to the views via a 7 m long, 17-channel, 600 μm 0.37 NA plastic-clad silica fiberbundle, though only 11 fibers are imaged. In the
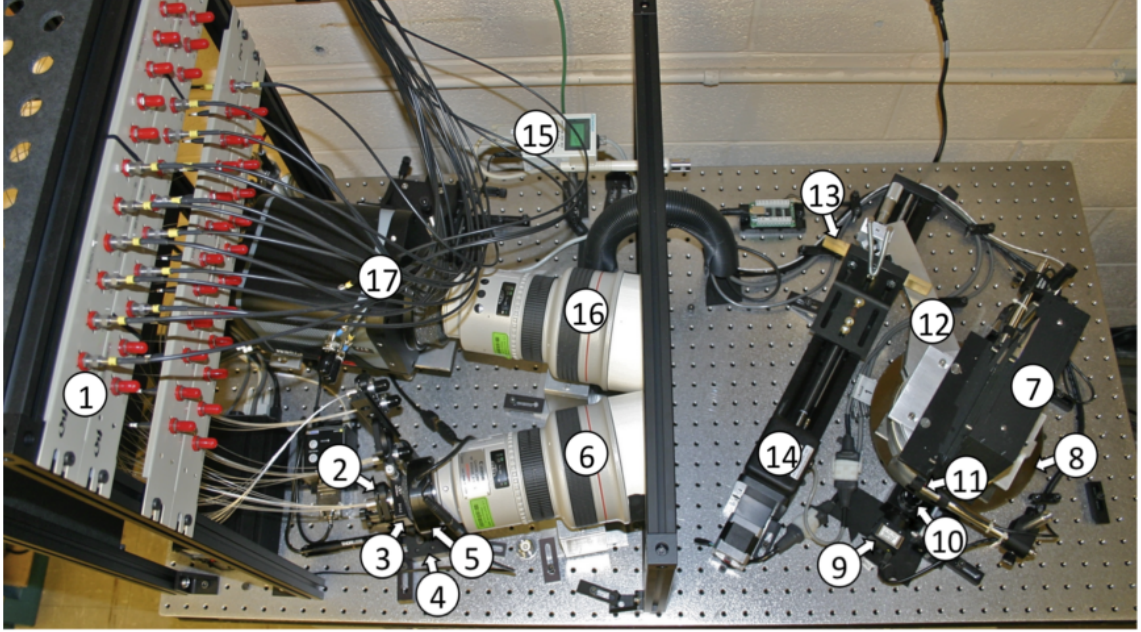
Figure 4.3: Overview of the HAL spectrometer. Components include (1) fiber optic patch panel, (2) fiber holder, (3) entrance slit, (4) translation stage for slit assembly, (5) lens controller, (6) collimating lens, (7) grating, (8) encoder disk, (9) encoder camera, (10) microscope objective and 45° mirror, (11) LED, (12) tangent arm, (13) pusher plate, (14) stepping motor and slide, (15) thermometer and barometer, (16) focusing lens, and (17) CCD camera. Figure and caption reproduced from [9].

initial LTX system the SMA-terminated ends of the fibers screwed directly into the individual collection lenses. In the present poloidal system they attach to the patch panel and then to the collection arrays via 15 m transfer fibers. The entrance slit is curved to correct for image curvature of the spectrometer, and its 75 μm width sets the instrumental width. At unity magnification, this corresponds to a FWHM in wavelength $\sim$0.9 Å or T_{Li} $\sim$35 eV.

The High-throughput, Accurate-wavelength, Lens-based (HAL) spectrometer was developed for NSTX [10, 91], but has been installed at LTX monitoring the toroidal array [9]. The entrance and exit optics are identical Canon 200 mm f/1.8 EF lenses. The spectra are resolved by a 128x154 mm plane ruled grating blazed at 5000 Å with a groove frequency of 2160 mm^{-1}. A stepping motor rotates the grating so the spectrometer can cover its effective range of 4000-8200 Å.

The HAL spectrometer uses a high-precision manually-adjustable straight entrance slit. The entrance slit is mounted on a linear stepping motor drive so it can be moved to the optimal focus when the spectrometer wavelength is changed, to correct for chromatic aberration of the lenses. Optical fibers are connected to the entrance slit with custom high-precision fiber holders that are held in place via magnets to within 1 μm. A fiber holder with thirteen 400 μm fibers was used for measurements on LTX.

A Visual Basic program controls the spectrometer, and includes procedures to calculate the proper stepper motor position for the grating rotation and slit focus given a requested central wavelength, and move the motors to that position [9]. It will automatically record these values before a discharge and write them to MDSplus. Automatic procedures also aid in the alignment and testing of the system in particular for wavelength calibration, slit focus calibration, slit width calibration, and reproducibility tests.

The Holospec and HAL spectrometers each use a Princeton Instruments ProEM 512 camera for high-efficiency, high-speed measurements. Each camera has a 512 x 512 CCD array of 16 x 16 μm pixels, is back-illuminated for high quantum efficiency, and thermoelectrically cooled to -70 °C to minimize thermal noise and dark current. Pixel readout is done after first shifting the image to an additional CCD array behind a light-blocking mask, allowing simultaneous analog to digital conversion (ADC) read out and exposure. Each row can be shifted in 450 ns, meaning 237.6 μs to shift the 512 rows and an additional 16 buffer rows. The CCD has on-chip binning so the $\sim$45 vertical pixels illuminated by each fiber can be binned into one line, improving signal levels and reducing total read out time. The camera has a 16-bit precision ADC with 3 different analog gain settings (1x, $\sim$2x, $\sim$4x) which can be operated at 5 MHz using a standard low noise readout or at 10 MHz with a electron multiplied readout (1-1000x gain). The low noise readout is typically used on the Holospec for

a total frame time of 2.25 ms, while the faster readout is used on HAL (typically without multiplication) for a frame time of 2.5 ms. The difference in readout time is due to the different on-chip binning configurations used in the different cameras. The Holospec has 11 fibers and 11 bins where the bins include the dark regions between the fibers. The HAL spectrometer has been used on LTX with 13 fibers and 27 bins, alternating the dark and illuminated regions to minimize crosstalk and noise (at the expense of speed). The timing of the cameras' readout are controlled by digital function generators, which are themselves triggered by the CAMAC Jorway timing modules that control timing for all of the LTX subsystems.

Each camera is connected via a Gigabit Ethernet connection to a PC running Win-Spec 32 software. A Visual Basic interface, originally developed to control cameras in the NSTX CHERS system, was modified to work alongside the HAL spectrometer Visual Basic program and control the HAL camera and function generator [9]. The interface was then further modified to control the Holospec camera (though not the function generator), as well as the other LTX-operated Princeton Instruments cameras in the TS system, LoWEUS, and HIGGS. The interface allows camera settings to be configured through WinSpec, waits for MDSplus events based on the shot cycle, acquires the data, and writes the data to the MDSplus tree. The HAL interface also loads the correct on-chip binning configuration for each of the different fiber holders.

4.3   Calibration of the spectroscopy system

The collection optics were focused and the spatial locations of the views were measured during an in-vessel calibration. The collections lenses and fibers were installed on the vessel, and the other end of the fibers were illuminated with a bright light source so that the sightlines were filled with a beam of light. A ruler was then put in the path of the beam, and the position and size of the beam was measured relative to known vessel

Figure 4.4: In vessel spatial calibration of toroidal views by illuminating fibers and photographing spots projected onto a ruler.

components. The toroidal views were first focused by back-illuminating the fibers and adjusting them in the fiber holder until each formed a sharp image on a ruler inserted in the DE radial port, perpendicularly bisecting the central sightline. The optics were then removed from the vessel in order to perform a LabSphere calibration, then reinstalled. The final spatial calibration was measured through the CD, DE, and EF midplane ports. As the upper and lower shell lips were not level with each other – or the bottom of the ports – a support was constructed to hold the ruler horizontal, which was verified with a bubble level. The poloidal views were focused to a distance corresponding to the nominal major radius and the illuminated spots were measured with a ruler inserted through the vertical 2-3/4" PA port (previously used for the initial poloidal views) and the vertical 3-3/8" PA port. The spots on the rulers were

photographed and ovals were fitted to them using ImageJ software in order to precisely determine their size and position. A geometric model was then used to calculate a best fit for the sightline paths based on the locations of the spots in the 3 different measurements and the location of lens.

The wavelength and instrumental width of the spectrometers were calibrated using neon and argon glow discharges. The vessel was filled with gas, and a glow discharge was created between the shells (which were grounded to the vessel) and a stainless steel probe inserted into the center of the shell volume. The discharge was powered by a 480 VAC supply with a ballast resistor that limited current to about 0.5 A.

Spectra (as well as dark frames with the vacuum window gate valve closed) were recorded with the Holospec, and at multiple wavelength settings with the HAL spectrometer, including the three used for the measurements in this work. The dark frames were subtracted, the multiple exposures were averaged, and the lines were fit in pixel space using a non-linear least squares fit to a single gaussian functions constrained so each line in a spectrum had the same width. The width of the gaussian function gave the instrumental width, as the Doppler broadening of lines in the relatively cold glow discharge was assumed to be negligible. The lines were identified using the NIST [52] and University of Kentucky [104] databases.

For the HAL spectrometer, these multiple wavelength calibrations were then fit with a function to interpolate these calibrations to intermediate wavelengths, based on a model of the optical elements in the spectrometer, their geometry, and the known temperature and pressure corrections to the grating line spacing and air refractive index. Details of this model were based on [10, 91] and beyond the scope of this work.

The absolute sensitivity of the camera, efficiency of the Holospec spectrometer, and throughput of the optics were calibrated all at once, including the vacuum windows (but not any in-vessel obstructions) using a LabSphere URS-600 Uniform Radi-

ance Standard. Because the LabSphere is Lambertian, the throughput is not dependent on angle or distance as long as the sightline is entirely within the aperture of the light source. As there were more total sightlines in the poloidal and toroidal arrays than could be connected to the Holospec at once, the calibrations were repeated for several different configurations of input fibers.

As the HAL spectrometer was not installed at LTX until after the optics were installed on LTX, the spectrometer was calibrated by illuminating a bare optical fiber (similar to those used in the arrays) with the LabSphere and sequentially attaching the fiber via the patch panels to each input fiber.

The full system Holospec measurements, as well as the bare fiber HAL measurements, were analyzed by first subtracting dark frames and averaging over multiple exposures, and then dividing the measured spectrum by the know spectral radiance curve of the LabSphere. Similar to the HAL wavelength calibration, the LabSphere calibrations performed with the HAL spectrometer at different wavelengths were fit with a function to interpolate these calibrations to intermediate wavelengths, based on a model of the optical elements in the spectrometer (including vignetting at the edges of the detector), their geometry, and the known temperature and pressure corrections to the grating line spacing and air refractive index. Details of this model were also based on [10, 91] and beyond the scope of this work.

As the bare fiber HAL calibrations did not include the effects of vignetting of the most outboard toroidal channels by in-vessel obstructions, an additional fiber-to-fiber correction was calculated based on in-vessel white plate calibrations using the HAL spectrometer to measure a compact, LED based light source. Throughput and transmission of the central toroidal view was assumed to be the same as the bare fiber. This calibration confirmed significant vignetting of the edge views, as well as some small discrepancies in calibrations of the innermost views, providing a more accurate photometric calibration for inverting profiles.
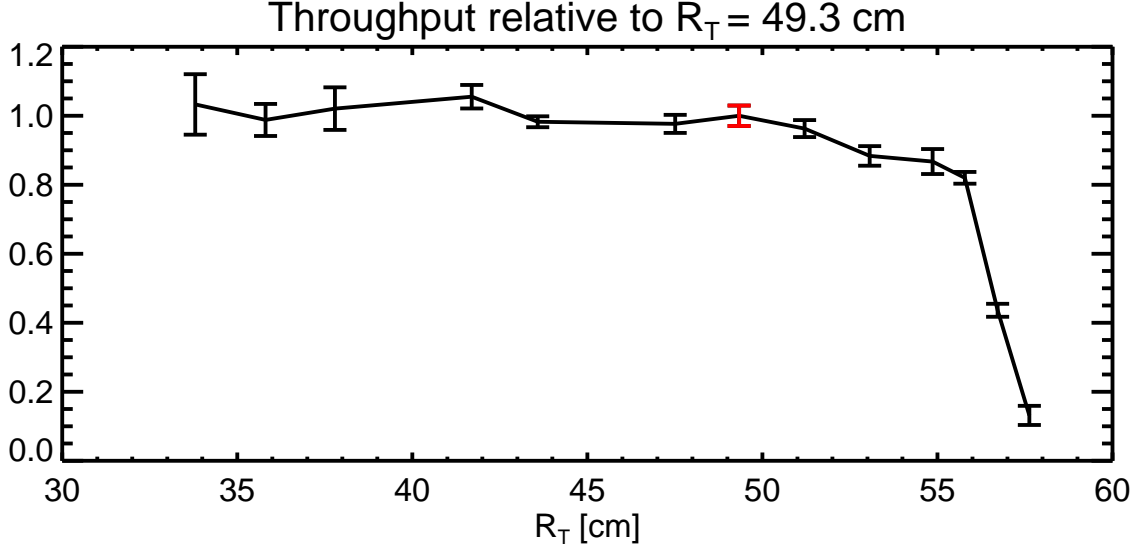
Figure 4.5: Throughput and uncertainty of each view relative to the view with tangency radius $R_T = 49.3$ cm (shown in red) from fiber-to-fiber calibration of toroidal array using the HAL spectrometer.

4.4 Analysis of the spectroscopic data

As the wavelength range monitored with the HAL spectrometer can be varied from 4000-8200 Å, it can observe a large number of different emission lines useful for analysis. Target lines for observation were selected based on the known gases, PFCs, and contaminants in the vessel, previous experience on plasma devices, and databases of emission lines from NIST [52], ADAS [98], and the University of Kentucky [104]. The accurate wavelength calibration of the HAL spectrometer simplified identification of lines that had not previously been characterized in LTX. The most commonly used wavelength setting covers the range from 4490-4670 Å in order to monitor Li III at 4500 Å and the C III triplet at 4650 Å, as well as C IV, Li I, Li II, and O II lines. The other key wavelengths used in this work are the C IV doublet at 5801 Å and the O V line at 6500 Å. Beyond the measurements presented in this work, the HAL spectrometer has also been used to look at H/D-α at 6563 Å, H-γ at 4340 Å, Li I at 6104 Å and 6708 Å, Li II at 5485 Å, Li III at 5167 Å (used by the ORNL Holospec), C
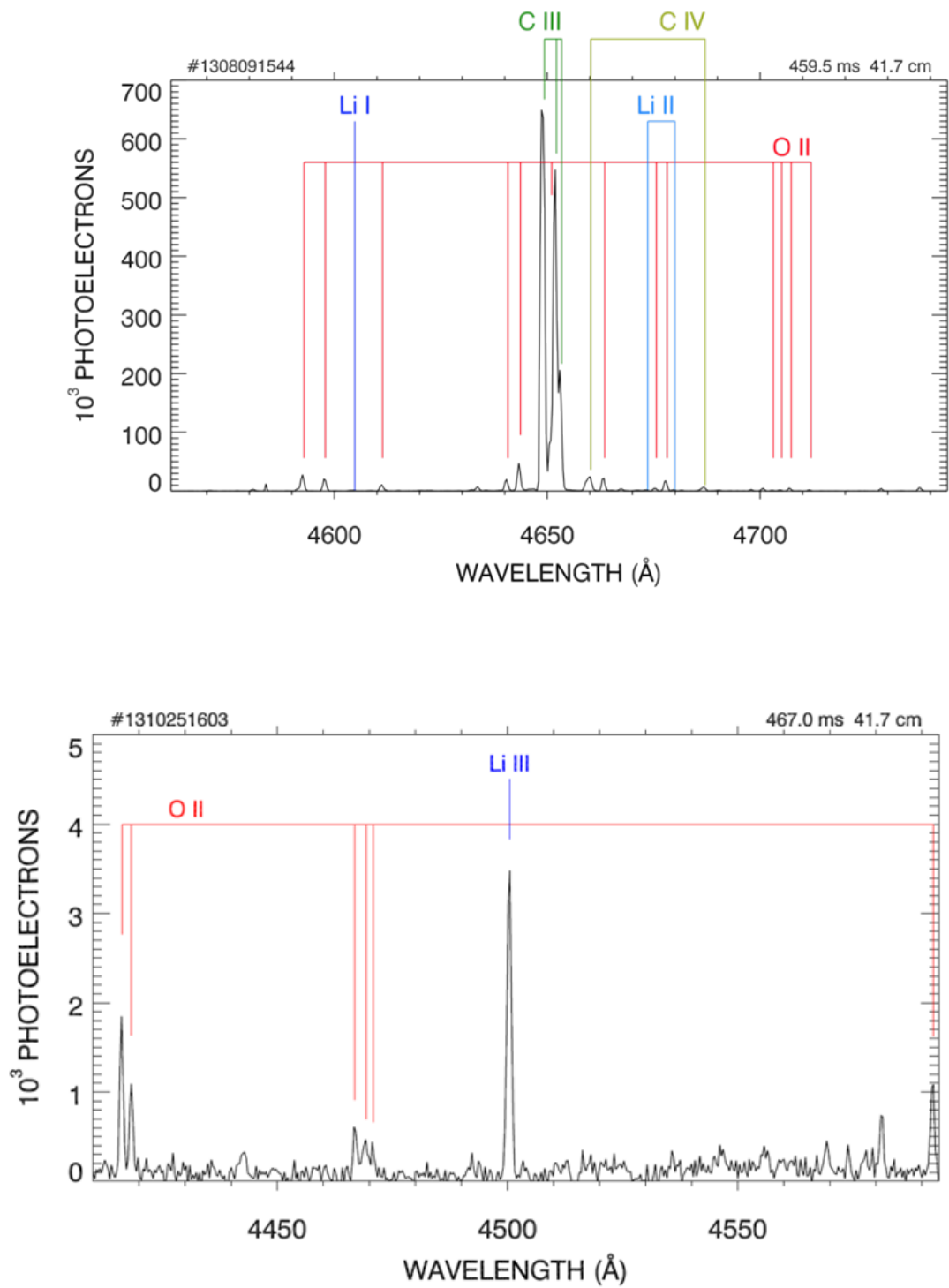
Figure 4.6: Plots of HAL spectra with line identifications showing C III at 4650 Å (top) and Li III at 4500 Å

II at 7120 Å, O III at 5592 Å, and Na I 5892 Å (Na is a trace impurity in Li). Many other lines have been observed but not identified, some have been sought but not observed, and no other impurities (besides N when a vacuum leak was temporarily present) have been definitively identified.

As described above, this work is based on measurement of Li III, C III, C IV, and O V impurity lines in order to determine impurity levels and understand impurity transport in LTX. Some of these are part of a multiplet structure and/or overlap with one or more other emission lines, and the lines of interest and the contaminating lines can also vary in relative intensity as a function of radius or plasma conditions. As a result, fitting each line of interest requires unique settings and methods based on the local spectrum. However, the overall procedure was mostly the same. For the discharges described in section 2.3, all of the raw spectra from different shots taken with the same settings were averaged in a similar method to the TS analysis in section 3.4, though without time averaging. Dark frames taken before and after the discharge were averaged and subtracted, and an algorithm based on [86] was used to remove the "smearing" effect caused by shifting the image behind the mask while continuing to expose the CCD to incoming light. The absolute intensity calibration based on the LabSphere measurements was applied and the spectrum as a function of pixel was fit to a sum of Gaussians convoluted with the instrument function. The fitting routine was a non-linear least-squares Levenberg-Marquardt algorithm, weighted by uncertainty propagated from the measurements and calibrations, and used settings optimized for the particular part of the spectrum being fit.

The fitting routine returned Gaussian amplitudes, central pixels, and widths, which were straightforwardly converted to profiles of line-integrated brightness, apparent velocity, and apparent temperature. To determine profiles of impurity density, local velocity, and local temperature, the fits were inverted based on methods described in [6, 7]. Inversion tends to amplify noise in a way that modest errors in edge

measurements can propagate to much larger errors in the core. Rather than inverting the raw profiles, uncertainty-weighted smoothing splines of the same type used in the TS analysis (section 3.5) were used to prevent random errors in each individual measurement point from having outsized effects.

Before smoothing and inversion, the brightness profiles were multiplied by the fiber-to-fiber correction, though the most heavily vignetted outer data points and fits with $> 20\%$ error were excluded from the smoothing-spline fits. The excluded outermost data points also suffered the greatest contamination by other edge impurity line emission, causing unrealistically high brightness and high apparent temperature. To ensure well behaved profiles near the edge, the smoothing splines were fit to the logarithm of the brightness and apparent temperature, including 3 additional points at R=66, 67, and 68 cm with brightness 5 orders of magnitude lower than the maximum and zero apparent temperature.

Despite the smoothing splines, each successive inversion step resulted in additional accumulated error, making the velocity and temperature measurements highly uncertain. There was also an unexplained offset in some of the absolute wavelength calibrations, which was corrected by shifting the wavelength arrays so that a neutral emission line, which was unlikely to be rotating, would be at its known rest wavelength. This correction made the velocity measurements more reasonable, though still uncertain.

In order to calculate the impurity density profiles from the emissivity profiles, the photoemissivity coefficients were calculated based on ADAS data and the spline smoothed, time interpolated, line-density corrected TS n_e and T_e profiles. The PEC data were read in from input files that gave values on a logarithmic $n_e - T_e$ grid, so the PEC profiles and their uncertainties were determined by bicubic interpolation of the logarithms of the TS values. Pre-calculate PECs for the O V line were not available directly from ADAS, so they were calculated using ADAS tools [80]. The
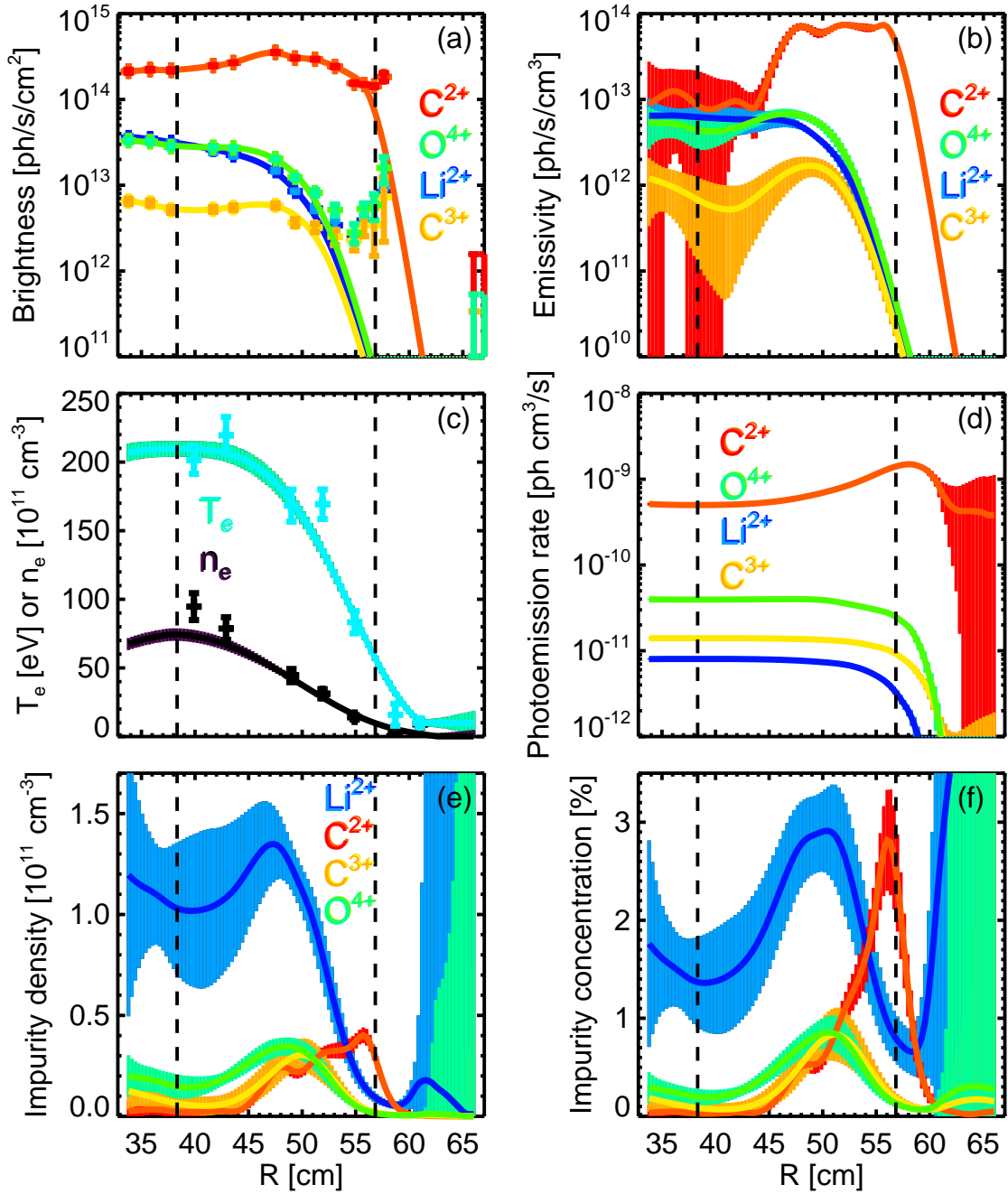
Figure 4.7: (a) Brightness profiles of Li^{2+} (blue), C^{2+} (red), C^{3+} (yellow/orange), and O^{4+} (green) from HAL measurements centered at t = 469.5 ms. Measurements are shown as + signs with error bars, error bars on the smoothing spline to log(Br) are too small to see. (b) Inverted emissivity profiles with error bands. (c) T_e (blue-green) and n_e (black, line-density corrected) profiles from the nearest average time, t = 469.75 ms. (d) Photoemissivity coefficients from ADAS averaged over the HAL measurement window using the spline smoothed, time interpolated, line-density corrected TS profiles. (e) Impurity density profiles. (f) Impurity concentration profiles.

76

PECs were averaged over the same time windows over which the HAL measurements were taken. The impurity density and concentration, and their uncertainties, were then calculated from the emissivity, PEC, and n_e profiles.

Chapter 5

Interperative modeling with TRANSP

While the density and concentration of impurities can be directly calculated from spectroscopy, Thomson scattering, and the ADAS database, additional measurements must be incorporated in order to assess the impurity transport, which can depend on other parameters such as the magnetic geometry. It is helpful to use an interpretive modeling code such as TRANSP [38] in order to integrate numerous diagnostics and physics concepts to build a plasma model that is as self-consistent as possible. TRANSP is a one-dimensional interpretive transport analysis code that determines power balance by solving the poloidal magnetic diffusion equation. In this work, TRANSP is used mainly as an input to the NCLASS [41] code to assess neoclassical transport, but development of the plasma model and analysis framework will enable future studies of many aspects of LTX.

Though TRANSP has been used previously in LTX for thermal transport studies [45], the present work makes numerous improvements. From an experimental point of view, it uses new experiments with improved wall conditions and discharge program-

ming. The measurements are also new and improved, both in terms of the diagnostic hardware and the data analysis.

5.1 Improved inputs relative to previous LTX TRANSP analysis

In comparison to LTX discharges previously analyzed with TRANSP [45], the discharges in the present study (described in section 2.3) were improved in several ways. The present experiments used e-beam evaporation in a well-conditioned vacuum vessel. In contrast, the earlier experiments used He-dispersed Li coatings (coatings in one set of experiments was considered only partial), and the vacuum vessel had not been as effectively conditioned to reduce water, both of which were associated with faster surface degradation. Furthermore, in this study improved programming of coil currents and fueling allowed longer discharges and an approximate flattop in plasma current.

The present analysis also benefited from a data set with improved measurements and diagnostic analysis, including some new capabilities that were not available in earlier work. In all LTX experiments, using repeated shots was necessary given the single-pulse limitation of the TS system. An analysis of repeated shots inherently studies a nominally "average" discharge rather than any one actual discharge, but using a large number of reproducible discharges reduced the effects of the variations in any one discharge. Therefore, even the most basic measurements were enhanced in the present study by using the most extensive data set available from LTX, with 55 reproducible discharges. Key inputs to TRANSP, including plasma current, loop voltage, and toroidal field were averaged over the data set, displaying only small variations, as seen in Figure 2.3.
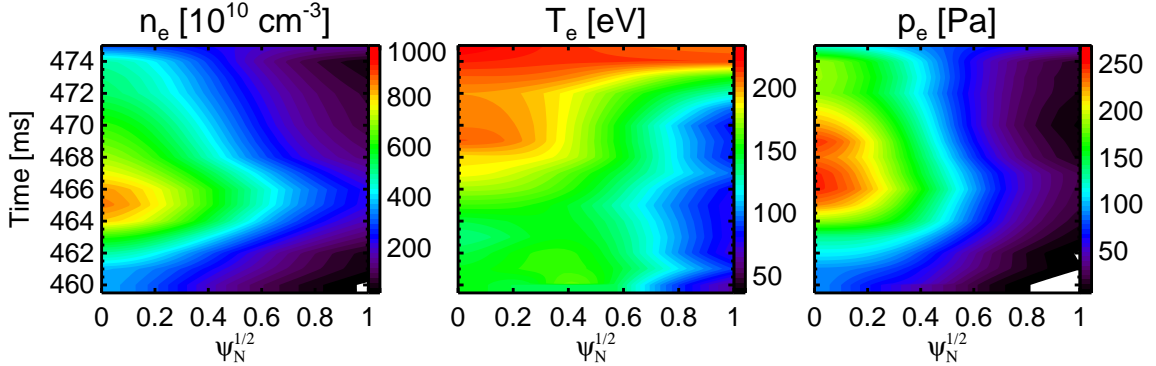
Figure 5.1: Contour plots of n_e, T_e, and p_e as input to TRANSP. The profiles were smoothed and interpolated as described in section 3.5 and mapped to flux coordinates by TRANSP. Following the large gas puff, the density peaked and then decayed after 465 ms and edge temperatures began rising after 472 ms, an indication of low-recycling.

The new data set also improved the quality of the TS data used in TRANSP, another crucial piece of the analysis. By taking more, longer discharges, it was possible to get data at 18 different time points at 1 ms intervals during the current flattop from 460-477 ms, and to repeat each time point 2-4 times. This is in contrast to the previous work [45], which used only 4-6 different time points over 3 ms periods without repeating time points. In order to further improve the measurements (particularly at low density at the beginning and end of the measurement range), not only were the repeated measurements at the same time averaged, but the neighboring time points were averaged in as well. As described in section 3.4, the TS measurements also benefited from improved calibrations and data fitting routines. Interferometer measurements, which were not directly available in the previously TRANSP analysis, were used to calibrate the n_e profiles, which were then found to match the reflectometer profiles.

Figure 5.1 shows contour plots of the TS density, temperature, and pressure profiles as a function of time and normalized magnetic flux. The density and pressure
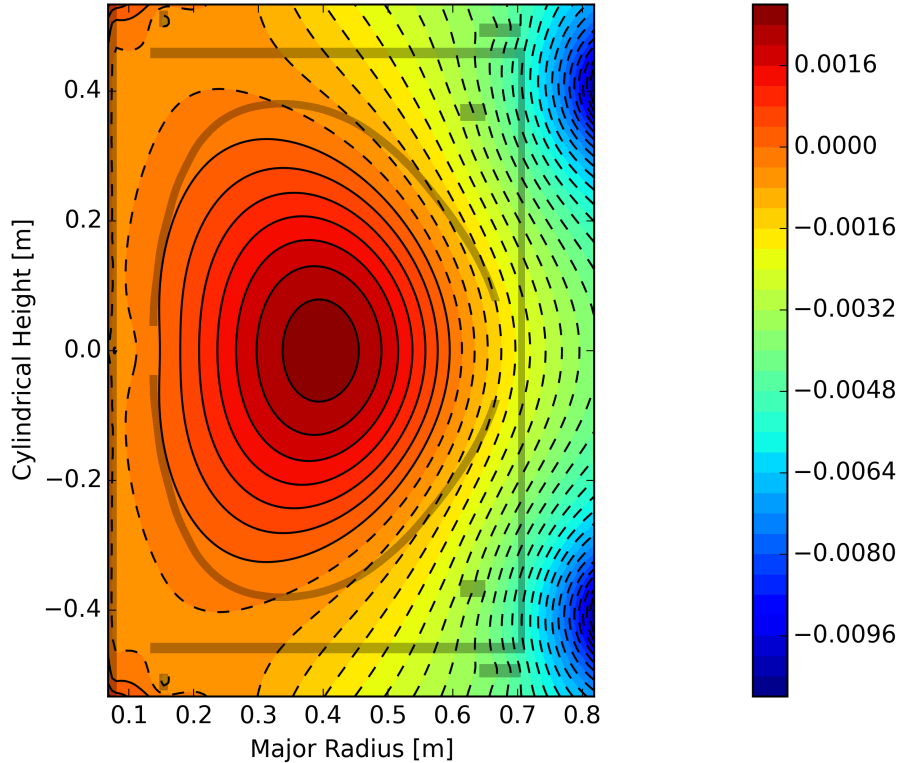
Figure 5.2: PSI-TRI magnetic equilibrium reconstruction at t = 463.2 ms. The contours and color bar show polodial flux (relative to the last closed flux surface) in units of weber/radian.

profiles were peaked throughout the discharge, and rose greatly during the large gas puff.

One notable result is that at late times in the discharge, after the gas puff when the density was decaying, the electron temperature profile became quite flat, remaining high all the way to the outboard last closed flux surface. This is notable as flat temperature profiles with high edge temperatures are one of the main predictions of the low-recycling regime [53, 108, 67]. One caveat is that due to the lower density, uncertainty was higher late in the discharge.

Among the most important additions in the present TRANSP analysis were the new magnetic equilibrium reconstructions, which set the basic geometry and were

therefore a very important part of the analysis. As described in section 2.2.1, the difficulty of producing reliable reconstructions meant that previous LTX TRANSP analysis did not actually use magnetic equilibria from the discharges being studied [45]. Equilibrium reconstructions were produced for the present discharges using the PSI-TRI code, introduced in section 2.2.1. The pressure profiles were constrained by the raw (not spline smoothed) TS measurements, with a multiplier of 1.3 to account for the unmeasured ion pressure contribution to the total plasma pressure. Equilibria were calculated at the mean times of the nearest neighbor time-averaged TS data, as well as midway between those times using interpolated pressure profiles. Converged, TS constrained equilibria were calculated for $t = 460$-475 ms, which set the TRANSP analysis interval.

Finally, the TRANSP analysis benefited in several ways from the new spectroscopic measurements. First, using the impurity densities and rate coefficients from ADAS, TRANSP could estimate the radiated power. Radiated power was not directly measured in LTX and could play an important role in power balance. The impurity density profiles also played a role in neoclassical models used by TRANSP to calculate bootstrap current and ion thermal transport. While measurements of the impurity concentrations allowed calculation of Z_{eff}, for this analysis TRANSP was set to allow Z_{eff} and q to vary in solving the magnetic diffusion equation, though not for other purposes. The impurity profiles were also the central piece in the impurity transport analysis, which are discussed in chapter 6.

While the HAL measurements were inverted to give ion velocity and temperature profiles, the insufficient quality of the fits yielded high uncertainties. Thus, velocity was neglected due to lack of external torques, while TRANSP was set to evolve the ion temperature profiles using neoclassical ion thermal transport, as previously done in LTX TRANSP [45].
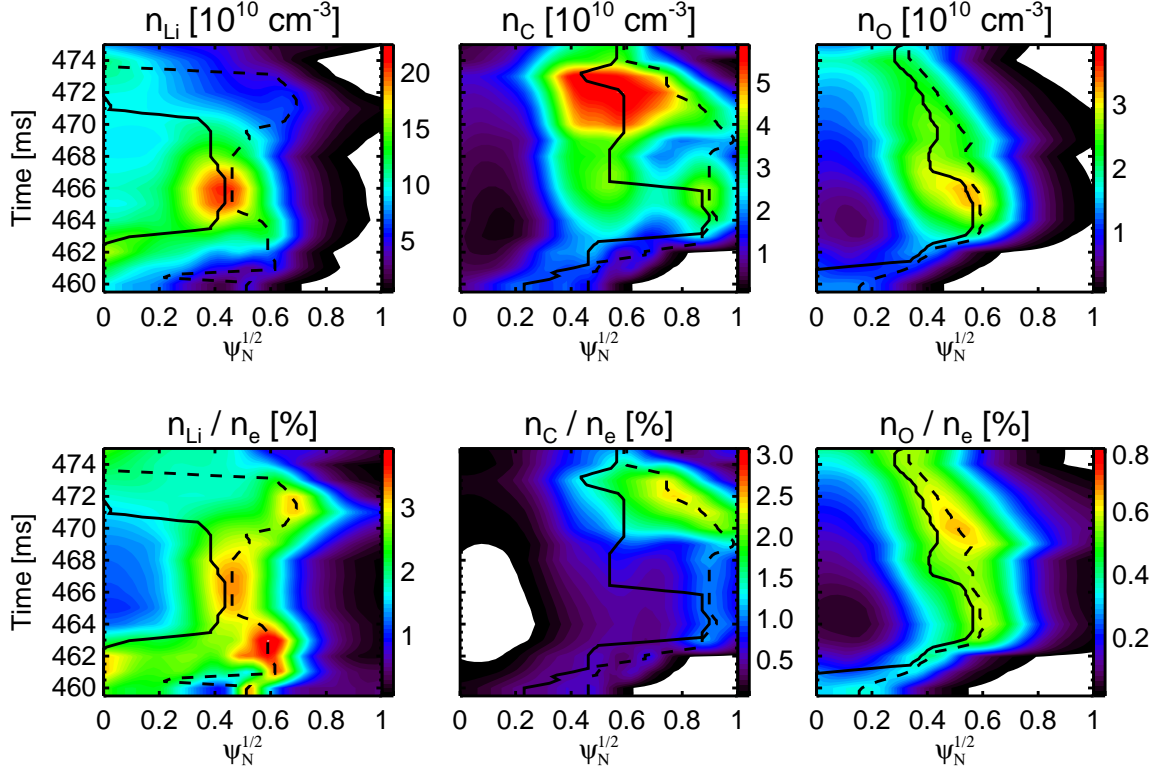
Figure 5.3: Contour plots of density and concentration of the measured charge states (Li^{2+}, C^{2+} + C^{3+}, O^{4+}) as a function of time and radial coordinate. Inside of the solid line indicating the maximum measured impurity density, the simple charge balance model holds the impurity density constant and fills in the gap with the next highest charge state. Outside of the dashed line indicating the maximum measured impurity concentration, the simple charge balance model holds the impurity concentration constant and fills in the gap with the next lowest charge state.

In the same way as the Thomson profiles in section 3.5, the impurity profiles were interpolated in time to a uniform timebase, with the contribution from each neighboring time point weighted by uncertainty. In order to further reduce noise, uncertainty, and (intermittent) spuriously high edge impurity concentrations due to contaminating emission lines, the interpolated HAL concentrations were smoothed in time using a Gaussian filter with $\sigma = 0.5$ ms, again weighted by uncertainty. The maximum width of the filter was 2.5 ms, equal to the HAL frame time, so that only profiles interpolated from the nearest neighbors in time were used in the smoothing. Figure 5.3 shows contour plots of the interpolated, smoothed profiles.

Importantly, the impurity profile measurements made with the HAL spectrometer did not cover all charge states of the impurities. Li was fully stripped in the core, and could not be measured with passive spectroscopy. The singly ionized states generally peaked in emissivity near or beyond the last closed flux surface, and thus could not be readily inverted. Finally, the other states did not have bright lines in the visible range observable by the HAL spectrometer.

Thus, modeling the profiles of the other impurity charge states was necessary to get a full picture of the impurities. In larger experiments operating in H-mode with $T_e > 1$ keV, light impurities can be assumed to be fully stripped within the edge pedestal. In LTX with $T_e \sim 200$ eV and low edge density, multiple charge states existed in a complicated balance of ionization, recombination, and transport. Determining this balance is in general a difficult problem requiring full knowledge of impurity transport of all charge states (including source terms) for use with an impurity transport code such as MIST [43] or STRAHL [21]. If impurity transport were known (or assumed) to be purely neoclassical, the missing states could be determined by iteratively calculating the transport coefficients of a given charge distribution, then calculating the charge distribution given the transport coefficients, until the charge distribution converges to match the known charge states. If there is additional anomalous impurity transport, either a functional form must be assumed or transport must be calculated with complex gyrokinetic codes. Calculations along these lines using NCLASS and MIST will be discussed in Chapter 6.

In any case, an initial guess for the missing states must be given before a transport model can be used. In this work, a simple model was used in which the the density of each impurity in the core was taken to be constant and equal to the maximum measured density, while the impurity concentration in the edge was taken to be constant and equal to the maximum measured concentration. As shown in Figure 5.3, density profiles of the measured impurity charge states were generally hollow, with a peak
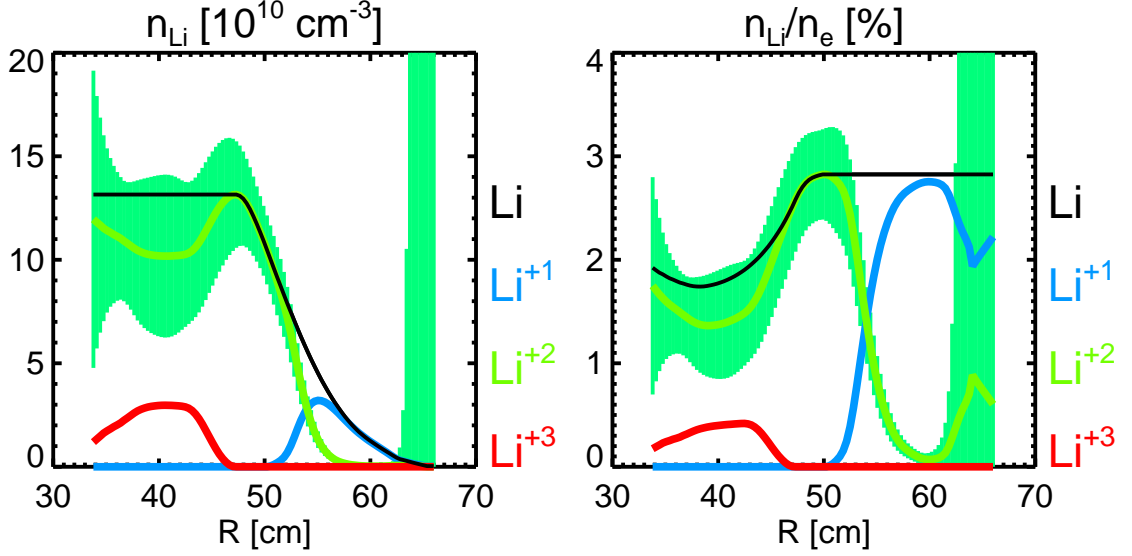
Figure 5.4: Profiles of impurity density (left) and concentration (right) for Li demonstrating the simple model for the unmeasured charge states. The measured Li^{2+} charge state is shown in green with error bands. The left figure shows how the model sets Li^{3+} (red) so that the total Li density (black) will be constant in the core and equal to the maximum measured density. The right figure shows how the model sets Li^+ (blue) so that the total Li concentration (black) in the edge will be constant and equal to the maximum measured concentration.

at mid-radii and usually decreasing monotonically in either direction away from the peak. There were some exceptions, where at certain times the profiles had an additional peak closer to the edge (often likely spurious due to emission from competing lines). However, the edge peaks were greatly reduced by the weighted time-smoothing of the profiles, due to the high uncertainty of the measurements that demonstrated edge peaks. As the electron density was monotonic in all cases, the peak impurity density occurred inward of the peak concentration. To estimate the unknown charge states, the radial location and magnitude of the maximum measured density and concentration was first determined for each measured impurity (Li^{2+}, $C^{2+} + C^{3+}$, O^{4+}). In the core, the density of the next highest charge state (Li^{3+}, C^{4+}, O^{5+}) was set to make the total impurity density equal to to maximum measured density, as shown in Figure 5.4 (left). In the edge, the concentration of the next lowest charge state (Li^+,

C^+, O^{3+}) was set to make the total impurity concentration equal to the maximum measured concentration, as shown in Figure 5.4 (right).

The assumption that these are the most important unknown charge states to model can be justified in a few different ways. First, Li^{3+} was the only charge state left in the core, but could not be observed without a neutral beam. Li^+ was observed easily but was un-invertible to determine a profile, as the emission was probably dominated by ions at the edge, beyond the outer tangency radius of the toroidal array. C^{4+} was not observed, likely due to its strongest emission lines being unmeasurable by the LTX diagnostic set. C^{4+} was, however, observed using different diagnostics in CDX-U under plasma conditions similar to those in LTX. C^+ was also easily observed but un-invertible, while both O^{5+} and O^{3+} were seen in LoWEUS spectra, though they were unresolved in time and space and not absolutely calibrated. O^+ and O^{2+} have also been observed, but assuming the edge state to be O^{3+} was most conservative in terms of avoiding underestimation of the effects of O. Finally, Section 6.3 will show that the modeled states were in fact the most important in MIST simulations that match the density profiles of the measured impurity charge states. However, the simulations also suggest that the densities of the unmeasured charge states could range from somewhat to significantly larger than predicted by the simple model. Therefore, the simple charge balance model could be considered a lower bound for total impurity density.

The simple model was chosen to fill in the unknown charge states in a reasonable way while making minimal assumptions that did not require transport or collisional-radiative models, did not add impurities beyond the maximum measured densities or concentrations, and took a middle ground between peaked and hollow density profiles. Alternate simple charge balance models could use only assumptions of fixed impurity concentration (based on the concentration at maximum impurity density and/or the maximum concentration) rather than fixed core impurity density. Using the concen-
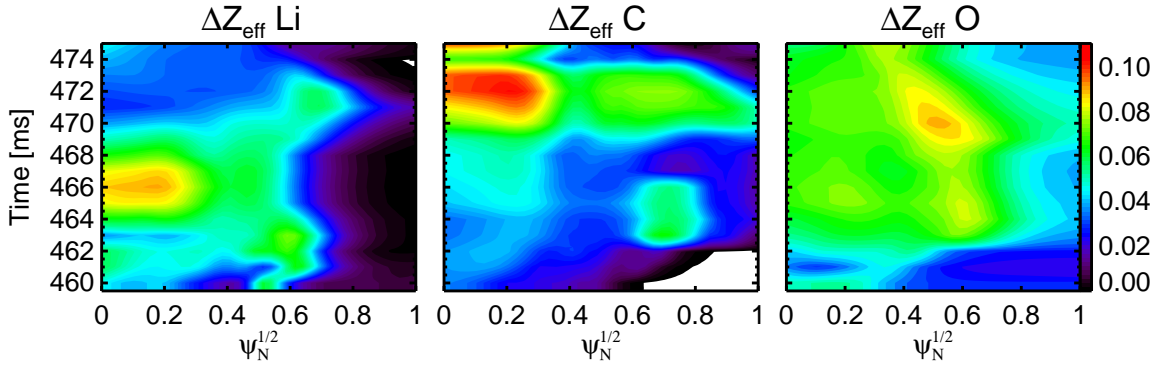
Figure 5.5: Contour plots of ΔZ_{eff} for Li, C, and O from measurements and the simple charge balance model as a function of normalized flux and time. The plots use a common color scale.

tration at maximum density throughout would often result in no lower charge states in the edge, where the concentration of the measured charge state(s) was often already larger than that at maximum density. Using the maximum concentration throughout would make the model often strongly dependent on the edge concentration peaks, many of which are presumed at least partly spurious. Using the first method in the core and the second (as done in the used model) in the edge would likely be the best compromise, and most similar to the present method, though it would imply (for better or worse) peaked impurity profiles with greater than measured densities. Models based on fixed charge density, charge fraction, or ΔZ_{eff} could also be used.

5.2 Results of TRANSP integrated plasma model

Once the measurements were processed and input, TRANSP calculated a wide variety of additional parameters relevant to understanding the behavior of impurities.

Using the simple charge balance model allowed calculation of the contribution from each impurity to Z_{eff} , shown in Figure 5.5. Unlike in NSTX, where C was by far dominant, contributing ΔZ_{eff} up to 3 by the latter half of the discharges [90], Li, C, and O all contributed roughly equally to Z_{eff}.
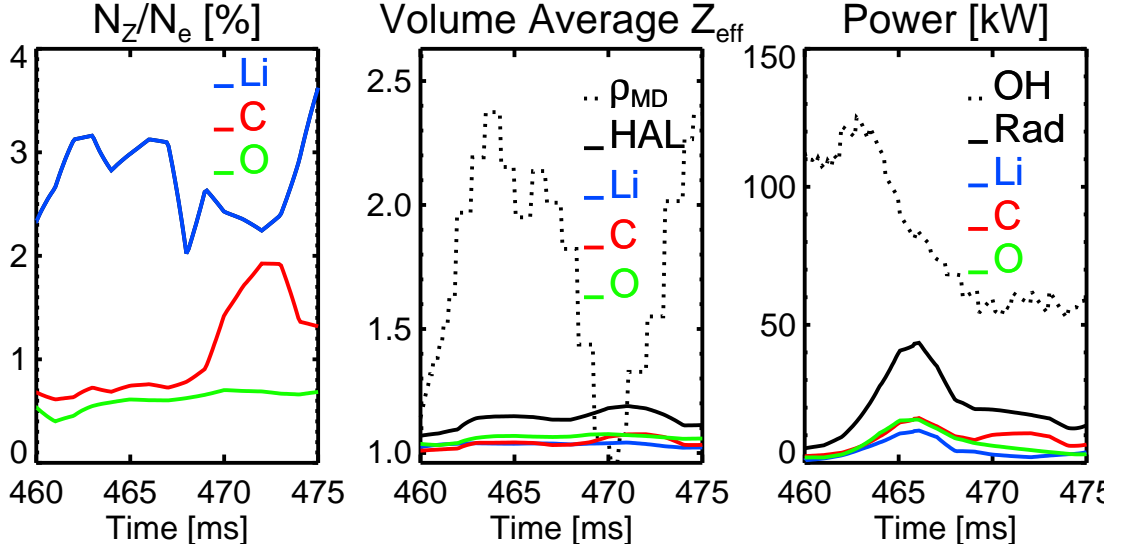
Figure 5.6: Time evolution of volume averaged impurity concentrations from measurements with the simple charge balance model (impurity inventories N_z / electron inventory N_e). Time evolution of volume averaged Z_{eff} calculated from the resistivity in the TRANSP poloidal magnetic diffusion equation, and from measurements with the simple charge balance model. Time evolution of ohmic heating power from TRANSP and radiated power from TRANSP based on ADAS and the impurity inputs.

TRANSP solved the poloidal magnetic diffusion equation to find the ohmic power balance, with I_p and V_{loop} fixed by the input files but allowing Z_{eff} and q to vary. Figure 5.6 shows the results of TRANSP's use of the ADAS database to calculate radiated power based on the given plasma and impurity model. At ∼466 ms, near the peak in density, total radiated power also peaked at about 60% of the input ohmic power, with the different impurities contributing roughly equally. Radiated power declined below 40% of the input power for the rest of the discharge, with the contribution C declining the least.

The radiated power calculations were uncertain due to their dependence on the assumed impurity charge balance model. Still, they indicated that while impurities may not have a major effect on resistivity, they are likely important to the power balance of a small ohmically-heated tokamak like LTX that does not reach high enough temperatures and densities to burn out light impurities.

In contrast to the experience with Li wall-coatings on C PFCs in NSTX [90], with high levels of C and negligible amounts of Li, the impurity concentrations in this LTX discharge can be characterized as low, but non-negligible, with the simple model for the charge balance yielding volume averaged concentrations of $\sim 2-4\%$ Li, $\sim 0.6-2\%$ C, and $\sim 0.4-0.7\%$ O. Maximum concentrations were slightly higher and concentrations at maximum impurity density generally slightly lower. Assuming the simple model, Z_{eff} was small compared to many tokamaks, though radiative losses still accounted for a large fraction of the ohmic heating power. The comparison of LTX and NSTX is of course not simply limited to the difference between applying Li to metal instead of carbon PFCs. Differences in impurity sources are driven not just by PFCs but by vastly different SOL plasma parameters and geometry. Furthermore, the LTX discharges were much shorter and more rapidly evolving than in NSTX. In the NSTX discharges, ΔZ_{eff} from C was in a similar range of $\sim 0.1-0.3$ for the first hundred ms or so, though this time is also not directly comparable due to the higher confinement times in NSTX. The importance of plasma transport, which can take into account some of these differences, is discussed in the next chapter.

Chapter 6

Impurity transport

6.1 Neoclassical impurity transport

Neoclassical transport is the irreducible minimum for transport in a toroidal device, caused only by collisions between particles and enhanced over classical transport by the variation in particle orbits caused by the inverse major radius dependence of the magnetic field. This is in contrast to so-called anomalous transport, caused by instabilities that lead to more rapid turbulent mixing of the plasma. In all tokamaks to date, electrons are dominated by anomalous transport, but in certain low aspect-ratio tokamaks like NSTX, the ion transport is well described by neoclassical theory [50, 90]. The aspect-ratio (or its inverse $\epsilon = r/R$) is an important quantity in neoclassical theory, as it describes the deviation of the magnetic fields from the ideal, uniform fields in classical transport.

Neoclassical transport includes several different effects, and depending on plasma parameters can be dominated by effects in one of the three neoclassical "regimes": the highly-collisional Pfirsch-Schluter regime, the intermediate plateau regime, and the low-collision banana regime. These regimes are separated by a parameter called collisionality, defined in the large-aspect ratio limit as $\nu^* = \frac{\nu Rq}{v_T \epsilon^{3/2}}$ where ν is the
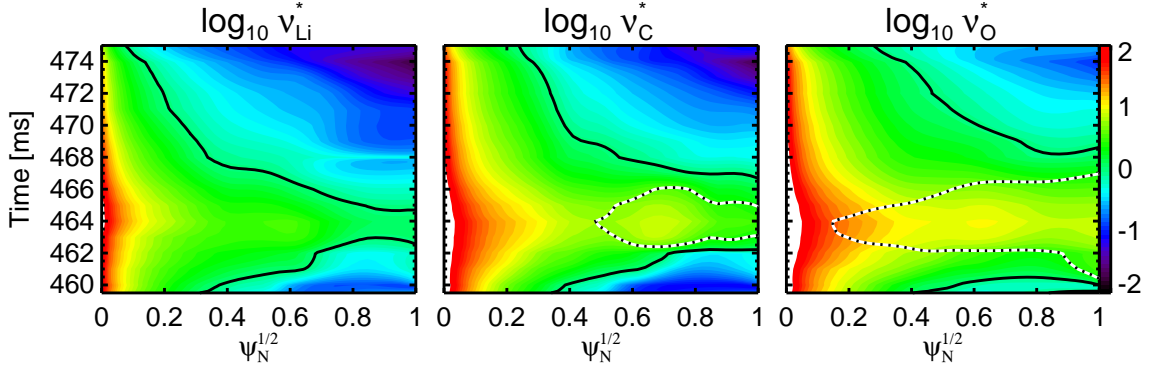
Figure 6.1: Contour plots of $\log \nu^*$ for Li, C, and O as a function of normalized flux and time. The plots use a common color scale. Overlaid are the $\nu^* = 1$ (solid) and the $\nu^* = \epsilon^{-\frac{3}{2}}$ (dotted) contours showing where and when banana and Pfirsch-Schluter transport are dominant.

particle collision frequency, q is the safety factor, v_T is the thermal velocity, ϵ is the inverse aspect ratio, with the dominant mechanisms given by $\nu^* < 1$: banana, $1 < \nu^* < \epsilon^{-\frac{3}{2}}$: plateau, $\nu^* > \epsilon^{-\frac{3}{2}}$: Pfirsch-Schluter.

Without collisions, the polodial field symmetrizes the ∇B and curvature drifts so there is no net drift over a toroidal circuit. In the Pfirsch-Schluter regime, particles on average collide before completing a single toroidal circuit. Thus transport is enhanced over classical because the particle is displaced from the field line by the drift motion as opposed to only the gyro-motion of classical diffusion.

When particles collide much less than once per toroidal orbit, Pfirsch-Schluter transport is greatly diminished and other neoclassical mechanisms become more important. In the banana regime, particles in the velocity distribution with sufficient perpendicular velocity relative to parallel become mirror trapped as they follow field lines from the low field side to the high field side. Thus they bounce back and forth while the ∇B and curvature drift cause the orbit to be at larger radius going in the one direction than the other, creating a banana shaped orbit. If a trapped particle undergoes a collision, it can therefore be displaced by a distance similar to the banana width rather than just a gyro-radius.

Figure 6.1 shows contour plots of ν^* for the different impurity species in the TRANSP model described in chapter 5. Though the large aspect-ratio estimate for the effective connection length is inaccurate near the low-aspect ratio boundary of LTX, it is still sufficient for this qualitative discussion. ν is calculated based on the outputs from TRANSP using a version of the Braginskii formula [105] $\nu_{ab} = \frac{16\sqrt{\pi}n_b e^4 Z_a^2 Z_b^2 \log\Lambda}{3m_a^2 v_{T_a}^3}$ for $m_a < m_b$, $\nu_{aa} = \nu_{ab}/\sqrt{2}$ for $m_a = m_b$, and $\nu_{ab} = \nu_{ba}(m_b n_b/m_a n_a)$ for $m_a > m_b$ and summing $\nu_a = \sum_b \nu_{ab}$. Overlaid in Figure 6.1 are the $\nu^* = \epsilon^{-\frac{3}{2}}$ contours (dotted lines) showing where and when Pfirsch-Schluter transport is dominant. As expected, the plasma is most collisional during the large gas puff (see Figure 2.3) when the density increases and in the core where the ion and impurity densities are highest and the impurities are in their highest charge states. The Z dependence of collisionality is also evident in the overall increasing collisionality from Li to C to O. The Pfirsch-Schluter regime is dominant during the gas puff in the outer part of the plasma for C and O but never for Li. Before and well after the puff, the banana regime dominates in the low-density edge and into the mid-radii, though O barely enters the banana regime before the puff.

While neoclassical theory describes many different effects and transport of heat, current, and momentum, here we focus on transport by and of impurities. One key parameter in determining the importance of impurities in driving transport is impurity strength, defined as $\alpha_Z = n_Z Z_Z^2/n_H$. This is plotted in Figure 6.2 for the different impurities in LTX assuming the simple charge balance model, while Figure 6.3 shows a comparison for NSTX [90]. In LTX, at time t=469.5 ms, the impurity strengths were similar with $\alpha < 0.15$, and even when taken all together the impurities were less than half as strong as the main ions ($\alpha = 1$). These ratios vary with time but no impurity was ever more than a few times stronger than any other, and even when combined the impurities are never stronger than the main ions. By contrast, C
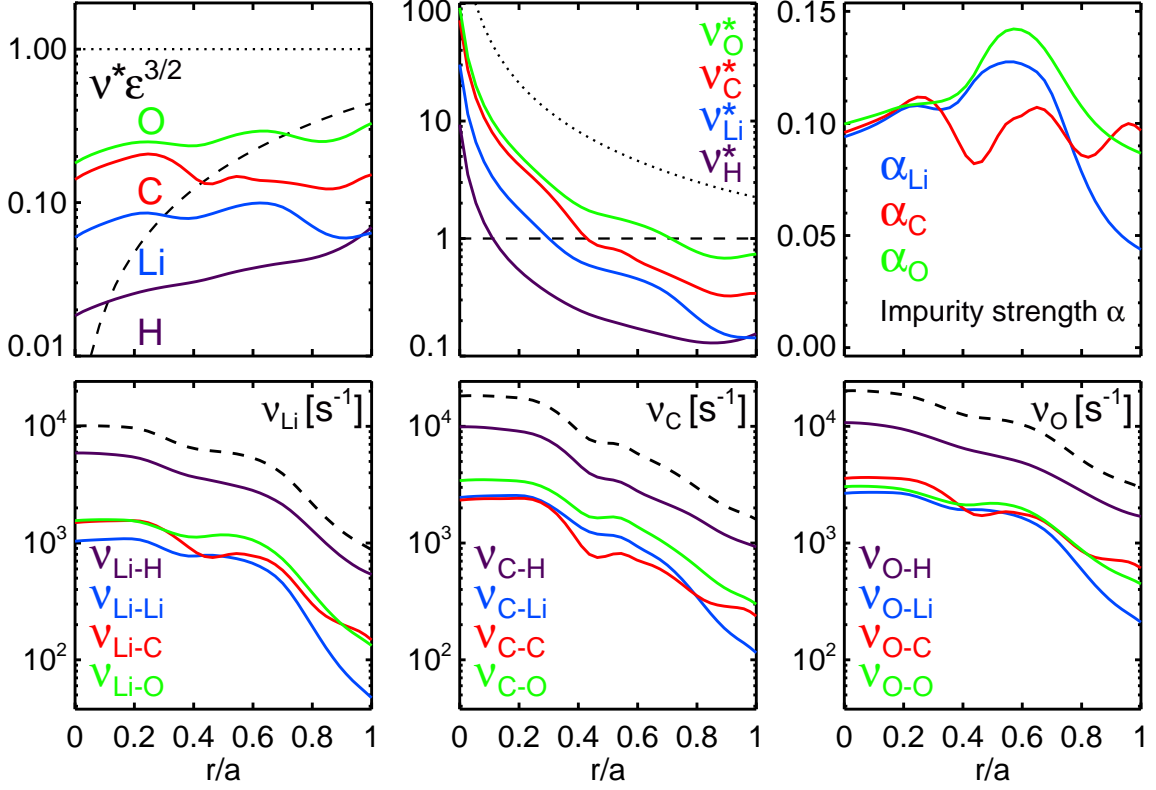
Figure 6.2: Profiles of normalized collisionalities $\nu^* \epsilon^{3/2}$ and ν^*, impurity strengths α, and ion-ion collision rates for at t = 469.5 ms. Li is shown in blue, C in red, O in green, and the main H ions in black. In the collisionality plots the Pfirsch-Schluter regime is above the dotted lines, the banana regime is below the dashed lines, and the plateau regime is between. In the ion-ion collision plots the dashed lines are the total collision rates for the ion.

dominated over the main ions in NSTX and Li was negligible, orders of magnitude weaker.

Figure 6.2 shows the collision frequencies between each impurity and each ion, as well as the total collision frequency, both again assuming the simple charge balance model. In LTX, collisions with the main H ions dominated over all three impurities, though the impurities drove about as many collisions as H when taken all together. Unlike NSTX, C never dominated, and Li and C were quite similar in terms of driving collisions rather than orders of magnitude apart.
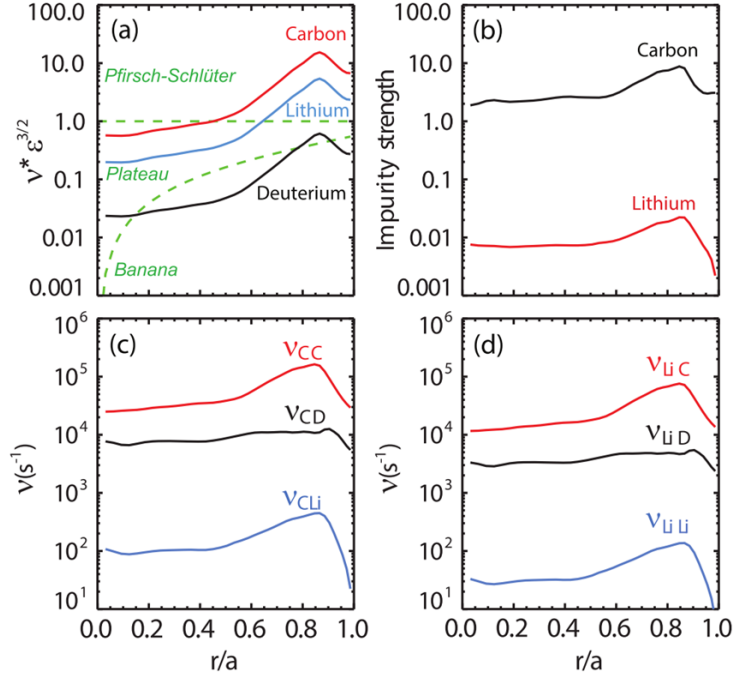
Figure 6.3: Profiles of normalized collisionalities $\nu^* \epsilon^{3/2}$, impurity strengths α, and ion-ion collision rates for NSTX shot 130725, reproduced from [90].

6.2 Neoclassical transport analysis with NCLASS

In order to calculate the neoclassical transport in these discharges, the output from TRANSP was fed into the standalone NCLASS [40] code using a Jython driver as done in [90]. NCLASS uses the Hirshman-Sigmar [39] formulation of neoclassical theory with a multi-species fluid model valid for arbitrary shape, aspect ratio, and collisionality. NCLASS calculates flux surface averaged 1D profiles of neoclassical transport properties.

Transport can be modeled as a convective-diffusive process, where diffusion acts to flatten gradients and convection moves particles (or heat, momentum, etc.) through a bulk flow. In terms of the impurity transport, the key outputs of an NCLASS computation were the flux surface averaged particle diffusivity D and convective velocity v for the different impurity species. 1D profiles of these were calculated by NCLASS
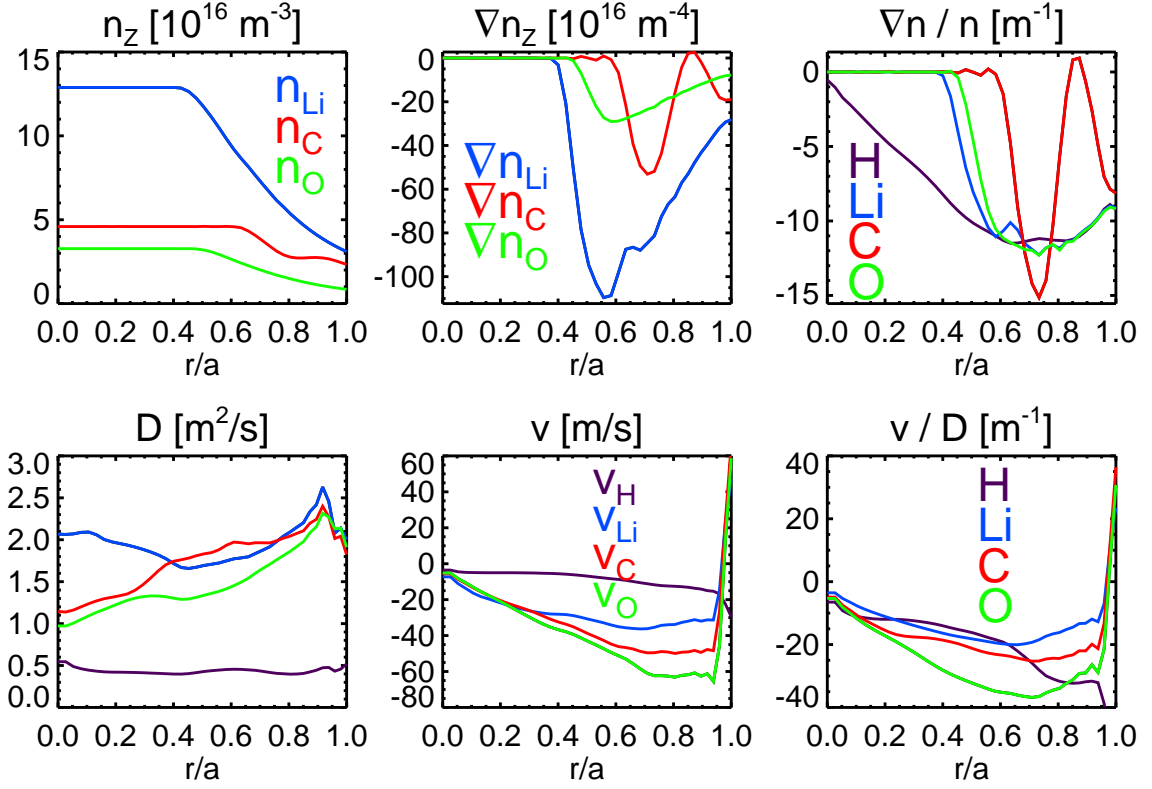
Figure 6.4: Profiles used by NCLASS based on measurements and the simple charge balance model (top row) and calculated by NCLASS (bottom row) of impurity density n_Z, impurity density gradient n_Z, inverse gradient scale lengths n_Z, diffusivity D, convective velocity v, and transport equilibrium peaking factor v/D. Li is shown in blue, C in red, O in green, and the main H ions in black. Profiles are in terms of normalized volumetric radius $r_{vol} = \sqrt{V/2\pi R_0}$.

on a uniform $\sqrt{\psi}$ grid. Figure 6.4 shows the NCLASS inputs and outputs at t=469.5 ms.

In general, impurity diffusivities and inward absolute velocities rose from core to edge. D_C was a bit more than half as large as D_{Li} at the magnetic axis, but a bit higher at mid-radii and essentially the same at the edge. D_O was mostly lower, but within $\sim 50\%$ of D_{Li} and D_C, and also essentially the same at the edge. Convective velocities were inward throughout the plasma volume and similar among species in the core. Toward the edge, inward absolute velocity showed a positive dependence on impurity atomic number, with $|v_{Li}|$ about half $|v_O|$.
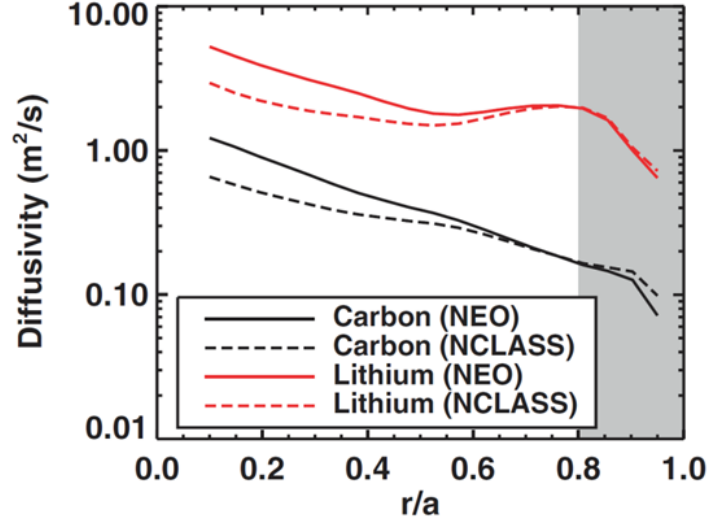
Figure 6.5: NEO and NCLASS calculation of radial transport coefficients for carbon and lithium on NSTX. Figure and caption reproduced from [90].

A similar dependence on impurity atomic number was seen when calculating the impurity peaking factor implicit from the transport coefficients, $L_Z^{-1} = |v|/D$. This is plotted in Figure 6.4, and corresponds to the impurity density inverse scale length $L_n^{-1} = |\nabla n|/n$ in a steady state, source free region. All three showed a hollow profile with a peak at the mid radii. However, as the total impurity density gradient profiles were fixed more by the charge balance model than the measurements, it is not particularly useful to compare the neoclassical transport peaking factor to the inverse scale lengths.

In general, these NCLASS calculations are dependent on the assumed charge balance model, so strong conclusions shouldn't be drawn from small differences in the neoclassical profiles. Rather it is more notable that the D and v profiles for the different impurities are similarly shaped and within $\sim 50\%$ of each other in LTX. This is in contrast to NSTX, where Li diffusivity was an order of magnitude larger than C as seen in Figure 6.5.

6.3 Impurity transport analysis with MIST

In order to determine if transport in LTX is well described by neoclassical theory, it is necessary to use an impurity transport code such as STRAHL [20, 21] or MIST[43]. Here, the neoclassical transport coefficients calculated with NCLASS were input to MIST in order to see if the impurity profiles are consistent. Given transport coefficients and a plasma model in a 1D cylindrical geometry, MIST numerically simulates transport of the various charge states of an impurity species, including ionization and recombination using ADPAK rates [43, 84].

MIST was run time-independent with both the SOL and wall radius set equal to the LCFS and the same transport coefficients used for all charge states of a given impurity. Both the transport coefficients and plasma model were directly extracted from the NCLASS output (with a small correction applied to transform coordinates from normalized flux to volumetric radius) and input to MIST in separate runs for each impurity. The electron density and temperature profiles, as well as on axis magnetic field and major radius, were the experimental values as input to NCLASS. The impurity density on axis was also input to MIST, though this only serves to scale the entire profile by a constant.

Figure 6.6 shows the results of the MIST simulated impurity density profiles for each impurity element and charge state, as well as the impurity density profiles from measurements and the simple charge balance model for comparison. These results are shown at t = 469.5 ms, though the results were essentially the same at several other times in the discharge. It is clear that the simulated charge state profiles bore little resemblance to either the measured impurity species or the simple model, meaning that the impurity transport was not well characterized by neoclassical theory in these LTX discharges, the time-independent MIST simulations did not fully capture the transport, and/or the simple charge balance model did not properly estimate the other charge states.
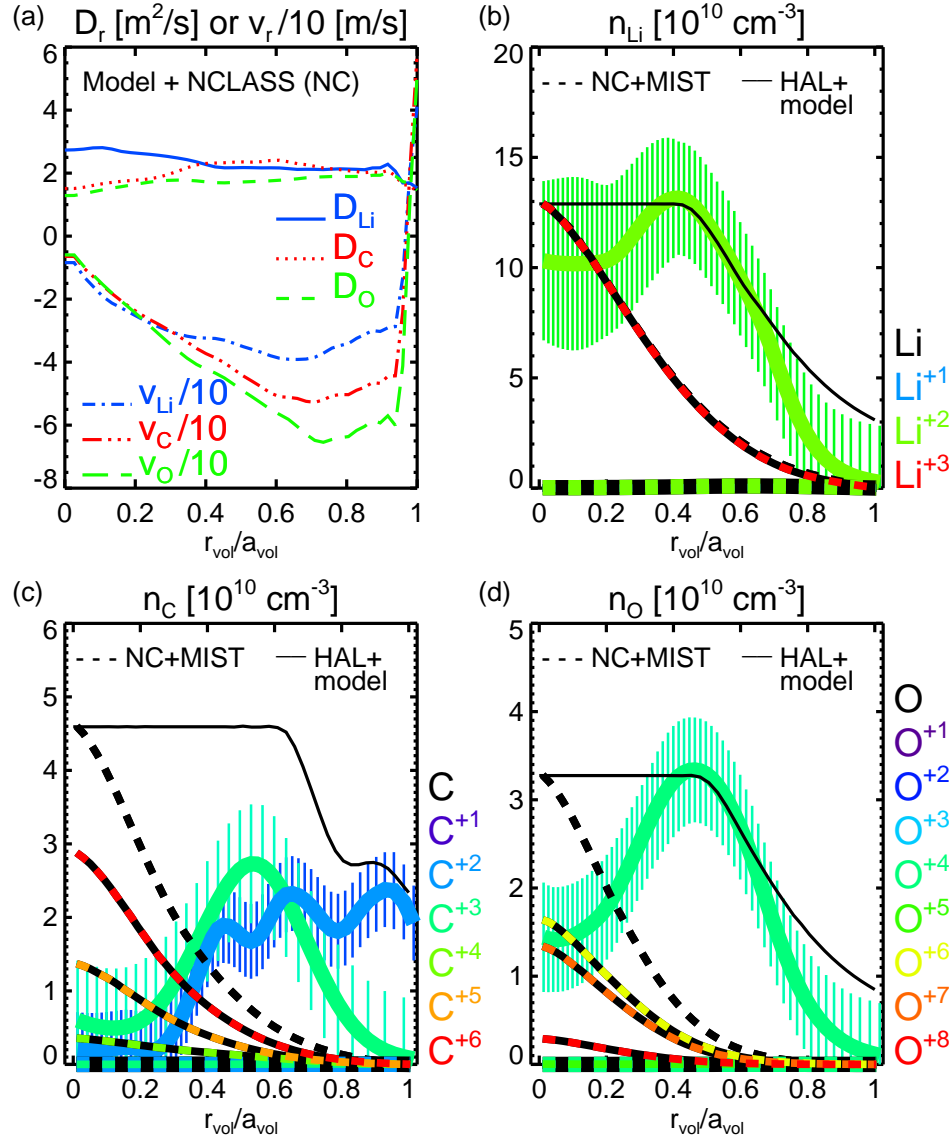
Figure 6.6: (a) Radial profiles of transport coefficients D and v from NCLASS based on the outputs of TRANSP at t=469.5 ms (as in Figure 6.4). Comparisons of radial profiles of (b) n_{Li}, (c) n_C, and (d) n_O from the MIST simulations using the NCLASS coefficients (dashed lines) and from HAL measurements and the simple charge balance model (solid lines). The black lines are total densities; the colored lines are the different charge states, increasing in charge from blue to green to red. The measured charge states are shown with thicker lines and the HAL profiles are shown with error bars. Core density of the MIST simulation was set to match the maximum of the HAL measurements. The MIST simulations show nearly all the impurities in higher charge states than observed with the HAL spectrometer.

In order to better assess the impurity transport in LTX, it was necessary to do further MIST simulations where D and v were adjusted such that the simulated impurity profiles actually matched the measured profiles. An IDL program was written to read the data from NCLASS, apply variations to the transport coefficients, run MIST, and compare the resulting impurity profiles to the measurements. Specifically, the program would vary the core impurity density for each impurity species individually, and apply the same adjustments to the transport coefficients of all three impurities. A Levenberg-Marquardt non-linear least squares fit algorithm was used to automate the fit between the MIST output profiles and the measured profiles with uncertainties as originally input to TRANSP. Different variations were performed with the parametrization $D = D_0 + c_D D_{NCLASS}$ and either $v = v_0 + c_v v_{NCLASS}$ or $v = v_0 + c_{v,n_e} L_{n_e} D$, including holding one or more of the various parameters fixed at 0, 1, or other values.

Exploring the parameter space, it was found that the measured charge state profiles could not be matched without $D > 10\text{-}15$ m^2/s. Beyond this constraint, however a variety of D and v profiles could match the data reasonably well with reduced $\chi^2 \sim 1$. Matching fits included constant $D \sim 16$ m^2/s and $v = 0$, many fits with $v > 0$ indicating outward convection in contrast to the inward convection from NCLASS, and other fits with implausibly large D and/or v. These various simulations yielded varying density profiles of the unmeasured charge states, some of which were within $\sim 50\%$ of the simple charge balance model, others which were several times larger.

For several of these simulations, the charge-resolved impurity density profiles output by MIST were then input back into NCLASS to recalculate the neoclassical transport coefficients. While the transport coefficients in many cases increased, they did not increase enough to meet the $D > 10\text{-}15$ m^2/s criterion needed to match the measurements. Indeed, when the recalculated neoclassical transport coefficients
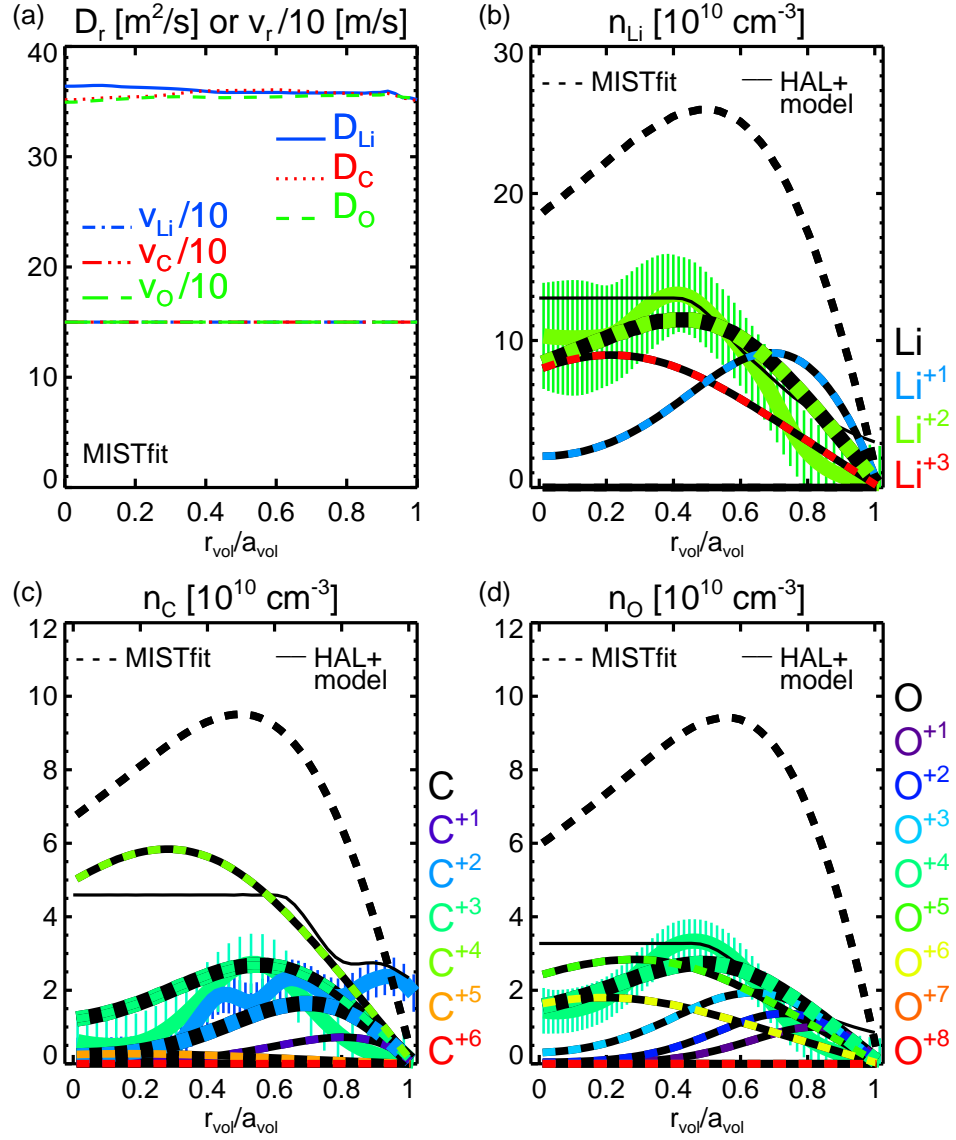
Figure 6.7: (a) Radial profiles of transport coefficients $D = D_0 + D_{NCLASS}$ and $v = v_0$ used in MIST after varying D_0 to fit the measured charge state profiles at t=469.5 ms. This simulation used fixed $v_0 = 150$ m/s and $D_0 \approx 34$ m^2/s gave the best fit. Comparisons of radial profiles of (b) n_{Li}, (c) n_C, and (d) n_O from the best fit MIST simulations (dashed lines) and from HAL measurements and the simple charge balance model (solid lines). The black lines are total densities; the colored lines are the different charge states, increasing in charge from blue to green to red. The measured charge states are shown with thicker lines and the HAL profiles are shown with error bars.

100
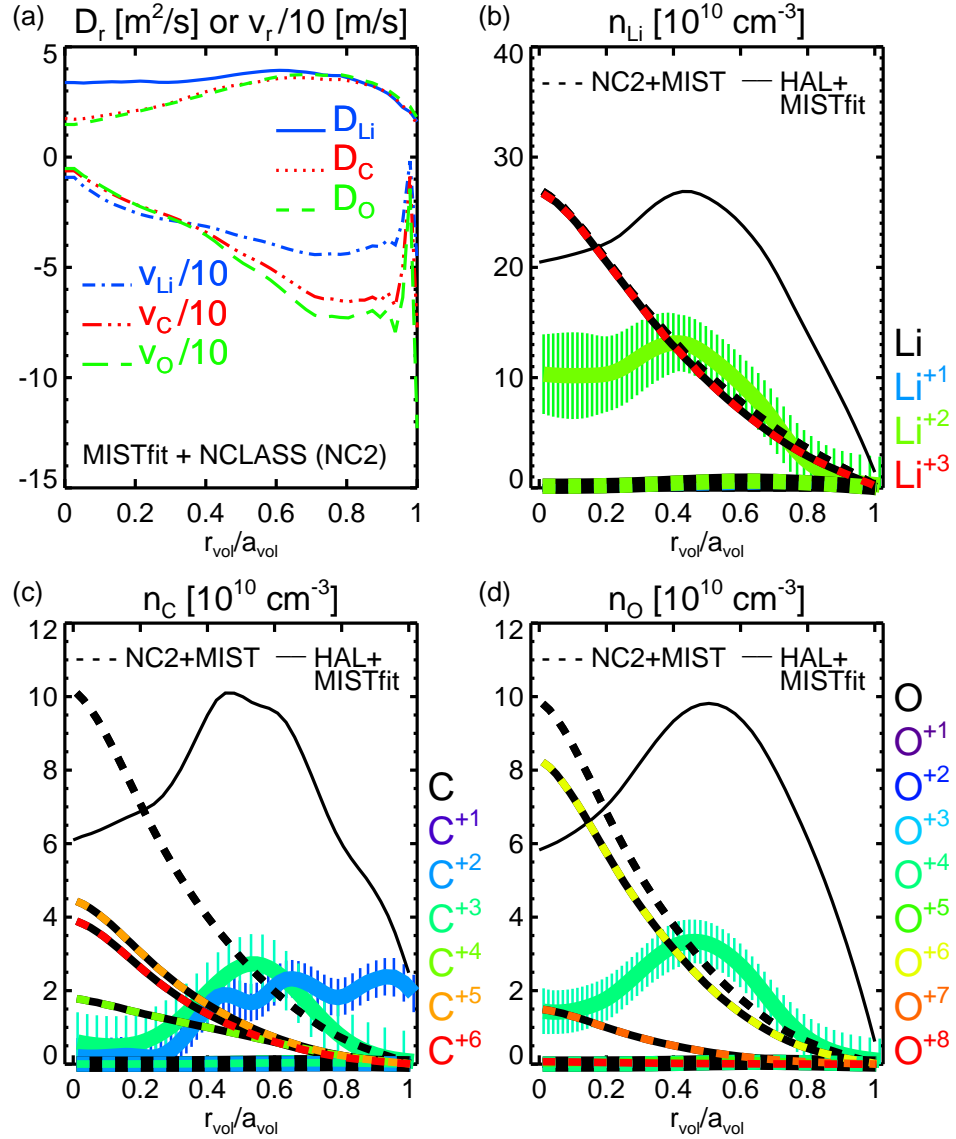
Figure 6.8: (a) Radial profiles of transport coefficients D and v at t=469.5 ms from rerunning NCLASS based on the best fit MIST simulated density profiles in Figure 6.7. Comparisons of radial profiles of (b) n_{Li}, (c) n_C, and (d) n_O from MIST simulations using the recalculated NCLASS coefficients (dashed lines) and from HAL measurements and the best fit MIST simulations (solid lines). The black lines are total densities; the colored lines are the different charge states, increasing in charge from blue to green to red. The measured charge states are shown with thicker lines and the HAL profiles are shown with error bars. Core density of the MIST simulations using the recalculated NCLASS coefficients were set to match the maximum of the best fit MIST simulations. As in Figure 6.6, the MIST simulations show nearly all the impurities in higher charge states than observed with the HAL spectrometer.

were put back into MIST, the simulated profiles matched the measurements similarly poorly to those with the original neoclassical transport coefficients.

Based on these calculations, it can be concluded that neoclassical transport was not the dominant impurity transport mechanism in these LTX discharges. Values of D at least several times higher than those calculated with NCLASS were needed to match the measurements, and v was often in the opposite direction, convecting outward rather than inward.

One caveat to the conclusion that transport was not neoclassical is that the MIST simulations were time independent, while the plasma and impurity profiles were evolving throughout the discharge. However, using time dependent simulations would have its own pitfalls in terms of path dependency, making profiles at later times dependent on choice of initial conditions and compounding of small errors in the transport coefficients. Another caveat is that the choice of parameters to vary in searching for a match to the measured profiles was fairly arbitrary, without any strong theoretical basis.

It remains inconclusive whether or not the simple charge balance model was a good estimate of the unmeasured charge states, but it certainly remained plausible as some simulations were reasonably close to the model. The simulations that matched the measurements generally showed the same unmeasured charge states to be most important. Also, even if one of the simulations that matched the measurements but were most different from the simple model were the most accurate representation of the charge balance, the main conclusions drawn in this work using the simple model would almost all remain. The conclusions that the various effects of the three main impurities, Li, C, and O, were of the same order of magnitude would not be affected. The maximum impurity densities and concentrations would be somewhat higher than with the simple model, with corresponding increases in Z_{eff}, P_{rad}, impurity strength α, ν^*, and neoclassical transport. However, as impurity transport is mainly driven

by collisions with the main H ions, impurity levels moderately higher than expected would not have a large effect, as shown by the iterated NCLASS-MIST simulations.

6.4 Evaluation of impurity transport analysis

Based on the TRANSP model (including a simple charge balance model) described in Chapter 5 and Thomson scattering, impurity spectroscopy, and other measurements described in Chapters 2-4, several complimentary approaches were taken to understand the impurity transport. Simple parameters including collisionality, impurity strength, and collision rate with other ion species were calculated for the different impurity species and compared. These parameters further developed the basic point that the effects of impurities in LTX should be considered modest, but still significant, and that despite measurable differences between the Li, C, and O impurities, they followed broadly similar dynamics. All showed similar evolution of collisionality profiles throughout the discharge, though the positive dependence of collisionality on Z meant only C and O entered the Pfirsch-Schluter regime while Li did not. The main H ions were dominant in causing collisions with the impurities, and the impurity strengths were all < 0.2 throughout the discharge, meaning that H was the dominant species for driving impurity transport.

Going beyond the simple parameters, a more complete picture of the neoclassical impurity transport was developed by using NCLASS to calculate transport coefficients. Again, broad similarity was found between the species in terms of the shapes and magnitudes of the D and v profiles. However, when input to time independent MIST simulations, impurity profiles calculated using the NCLASS output did not match the measured profiles. By allowing the D and v profiles used in the MIST simulations to vary, reasonably good matches to the measured profiles were found. These MIST results led to the conclusion that impurity transport in LTX is not

well described by neoclassical theory, and in fact anomalous transport is likely more important.

6.5 Comparison with impurity transport in NSTX

All of these approaches show a marked difference in impurity transport in LTX versus NSTX. In NSTX [90], C dominated the main ions in driving impurity transport, while Li was negligible. This had the effect of creating very different dynamics for Li and C transport, with order of magnitude differences in density, collisionality, and diffusivity, though both were mostly well described by neoclassical theory. In LTX, the opposite was found; the Li, C, and O impurities were similar in having small but significant concentrations that led to similar neoclassical transport, though overall impurity transport was not neoclassical.

It is unlikely that these major differences in impurity transport between LTX and NSTX were solely, or even mainly due to the different PFCs on to which Li is applied. NSTX is bigger, hotter, and denser, with steady-state, beam-driven, diverted H-mode discharges where strong shear at the edge suppresses ion scale turbulent transport, making it more likely neoclassical ion transport would dominate.

Chapter 7

Conclusions and future work

7.1   Summary of results

In Chapter 1 of this dissertation, the main purpose of fusion as an energy source was introduced, as well as some of the major challenges and approaches to achieving pratical fusion energy. Further background on specific topics including plasma-facing materials, impurities, and the use of lithium in tokamaks was given in order to motivate and explain the present work. Specifically, previous work studying Li on C surfaces at NSTX [90] motivated and inspired the analytic methods for this effort to improve understanding of impurity levels and transport in a tokamak with full Li coatings on all-metal surfaces.

It was therefore valuable to study impurities in the LTX facility, discussed in Chapter 2. The experimental capabilities and diagnostic set were discussed to explain the present work, and also serve to motivate future work in section 7.4.2. The key diagnostic systems for this work, the Thomson scattering and visible impurity spectroscopy systems, were discussed in Chapters 3 and 4, respectively. In both cases, the systems were described including the basic concepts, hardware, and calibrations. In the case of the Thomson scattering system, work to refurbish the existing hard-

ware and improve the existing analysis software were also described. For the impurity spectroscopy system, development of the new analysis software was described.

These data were integrated into a fairly complete plasma model using TRANSP, as described in Chapter 5. The new experiments used for this study were described, including improvements in vacuum and Li-wall conditioning and programming of the coil power supplies and gas fueling. The incorporation of measurements that were new and improved relative to prior use of TRANSP on LTX[45] was discussed. Key for this analysis was choice of a charge balance model to fill in unmeasured charge states. A simple model was chosen that sets the core density and edge concentration of each impurity to be constant, with the values set by the maximum measured density and concentration and the difference between the measured and modeled density filled in by the next highest and next lowest charge states. Based on this model, volume averaged impurity concentrations were low but non-negligible, with $\sim 2 - 4\%$ Li, $\sim 0.6 - 2\%$ C, and $\sim 0.4 - 0.7\%$ O. This corresponded to $Z_{eff} < 1.2$, with Li, C, and O contributing roughly equally. With the ADAS component of TRANSP, it was determined that radiated power reached a significant fraction of the input ohmic heating power.

In chapter 6, several approaches were taken to use the TRANSP model to analyze and understand the impurity transport. The basics of neoclassical transport were discussed, and simple parameters including collisionality, impurity strength, and collision rate with other ion species were calculated for the different impurity species and compared. All showed similar evolution of collisionality profiles throughout the discharge, though the positive dependence of collisionality on Z meant only C and O entered the Pfirsch-Schluter regime while Li did not. The main H ions were dominant in causing collisions with the impurities, and the impurity strengths were < 0.2 and summed to < 0.5 , low enough to mean that H was always the dominant species for driving impurity transport. A more complete picture of the neoclassical impurity

transport was developed by using NCLASS to calculate transport coefficients. The shapes and magnitudes of the neoclassical D and v profiles were similar for the different impurity species, with inward convection and both D and $|v|$ increasing from core to edge. Impurity profiles calculated with time independent MIST simulations using the NCLASS transport coefficients did not match the measured profiles. The simulated profiles were much more peaked and biased to higher charge states not observed with spectroscopy. By allowing the D and v profiles used in the MIST simulations to vary, reasonably good matches to the measured profiles were found. These had D at least a few times the neoclassical value and v often in the opposite direction from the neoclassical prediction, indicating outward convection.

7.2   Physics implications

Based on these results, several conclusions can be drawn. First, experiments performed during the course of this work provided further evidence that Li is a promising method to improve plasma performance, as already demonstrated in other work including on TFTR [69] and NSTX [70], and specifically on metal PFCs, as on CDX-U [68] and prior LTX work [88]. Though they are not discussed here, the first tokamak experiments fully surrounded by liquid lithium were performed in the course of this dissertation. In a general sense, a number of improvements in operations and understanding of lithium in tokamaks were also made in the course of this work, which built a large data set for future study.

The flat electron temperature profiles measured at the end of the discharge are intriguing results, which imply a low recycling boundary in which cold neutrals at the edge are greatly reduced and are not significantly cooling the edge. It is also notable that it occurs only after fueling is terminated, as the fueling during the discharge acts similarly to a recycling source in cooling the edge. Furthermore, as the temperature

stayed high, the density profile correspondingly dropped rapidly (as was confirmed by the reflectometer) to maintain a smooth pressure profile compatible with MHD equilibrium. Achieving this regime is one of the major motivations for using Li PFCs and for the research program at LTX in particular [67].

The impurity density profiles have several implications. First, they are the only measurements of Li and other impurity profiles in a tokamak with Li on all-metal PFCs. In FTU, $Z_{eff} < 1.5$ has been measured in discharges using a liquid lithium limiter with molybdenum and stainless steel PFCs, though the lithium limiter covered only a small area and impurity profiles have not been reported [3, 72]. In HT-7, Z_{eff} has been measured in experiments with Li coatings on molybdenum PFCs, though Z_{eff} was high at low density and only uncalibrated impurity emission measurements have been reported [18]. Thus, it is especially notable that LTX shows fairly low levels of impurities, with concentrations $\sim 2 - 4\%$ Li, $\sim 0.6 - 2\%$ C, $\sim 0.4 - 0.7\%$ O, and $Z_{eff} < 1.2$. In contrast, with Li on C PFCs, ELM-free H-mode plasmas in NSTX had up to 10% C and $Z_{eff} = 3 - 4$ [90], necessitating impurity mitigation.

While there are limitations to the data and their extensibility to other devices, at this point only positive implications for the future of Li in all-metal devices are evident. There are still open questions, however, that limit the ability to make definitive predictions about impurity concentrations in future devices or even that other LTX discharges with Li coatings on metal PFCs will be similarly low. The core transport is still not fully understood, let alone the impurity source terms and SOL transport.

What does seem likely in future devices with Li coatings on all-metal PFCs is that C will no longer be the dominant impurity, and that Li will be as or more important. Having three impurity species with fairly similar concentrations and contributions to Z_{eff} is a stark contrast to NSTX after the introduction of Li, where C impurities tripled Z_{eff} (due to ELM suppression) while Li was negligible.

Integration of the various measurements with TRANSP led to the result that radiated power from light impurities in LTX can be a significant portion of the input power, which will have significant impacts in the interpretation and analysis of old and new data, and be important in designing new LTX experiments and diagnostics. However, it should be noted that in larger fusion devices, light impurities are fully stripped in the core and losses from line radiation are only important at the plasma edge.

The impurity transport results lead to some conclusions that reinforce those from the impurity profiles. In NSTX, C was so dominant that Li transport was an order of magnitude higher than C. In contrast, in LTX the parameters that drive transport and the neoclassical transport coefficients were, as with the density profiles, mostly similar. Relatively equal transport across impurity species would have mixed, but overall probably positive implications for future tokamaks with Li on all-metal walls. Though they may lose the benefit of C pushing out Li impurities, the C impurity is much more harmful and preventing its accumulation is much more important.

7.3   Technical achievements

Next, in the course of this work two major diagnostics, the Thomson scattering and visible spectroscopy systems, were greatly improved and made useful for routine operation. Good electron temperature and density profiles are essential for almost any analysis. The quality of these measurements are underscored by the good match of the density profiles to the reflectometer. Impurity density profiles are also very important, as shown in this work, and in principle ion temperature and toroidal rotation profiles can be extracted from the spectra as well. Again, they are the first measurements of Li and other impurity density profiles in a tokamak with Li on all-metal PFCs. Beyond the measurements used in this analysis, measurements were made

under many of the different conditions described above and in Chapter 2 and will allow similar analysis under those and future conditions. The improved Thomson and new spectroscopy software also include numerous features which are not yet fully developed and will provide opportunity for further improvement.

Furthermore, the integration of new and improved measurements to TRANSP is important in setting up a suitable framework for analysis of LTX discharges. This builds on previous work [45] and also incorporates the new magnetic reconstructions and will be useful for many different kinds of analyses. New analysis tools were added to this LTX framework as well, adapting Jython scripts used in [90] to run NCLASS and calculate neoclassical transport based on TRANSP runs, then save them as language independent netCDF files. Additionally, IDL scripts were adapted and written to incorporate MIST into this analysis, both based solely on the NCLASS output and allowing transport coefficients to vary in order to match measured profiles. These tools will enable future studies of neoclassical and impurity transport, and are also easily extensible to enhance the present study.

7.4 Future research directions

7.4.1 Further, more detailed analysis of the experiment in this work

The present impurity analysis begins with an assumed charge balance model based on measured profiles, which after several intermediate steps are used in the MIST impurity transport code to adjust transport coefficients to best match the measured profiles.

The next major steps in the future to build on this analysis will be to add additional spectroscopic measurements to more fully tie down the charge balance and then to feed those profiles back into the beginning of the analysis and iterate to make

the analysis more fully self-consistent. The lower charge states at the edge may not be invertible but the uninverted brightness profiles can still be compared to synthetic profiles calculated from the charge balance and plasma model. Even the LoWEUS measurements of the EUV spectrum (which are integrated over the entire discharge duration) may be useful in constraining the higher charge states (especially oxygen). Measurements with the filterscopes and Holospec spectrometer may also be of use. Future improvements to this work will also include further refinements to the profiles, including post-calibration of the TS, and incorporation of other diagnostics like the reflectometer and Langmuir probes. Error propagation will include sensitivity scans and Monte Carlo runs of the transport codes. TRANSP can be run using different settings, for example holding Z_{eff} fixed to the measured value, which will also affect the current and ohmic heating profiles and power balance and thermal transport. It will also be useful to make use of the time-dependent capabilities of MIST and more thoroughly explore the transport coefficient parameter space.

These improvements are not expected to change the conclusions of this work, which are based on broad trends and not small differences, but will make the analysis more accurate, precise, and self-consistent, and more formally quantify uncertainty. This will allow a more detailed determination of the anomalous transport, which may give insight into its nature. It may also give a sense of the magnitude of the impurity source terms which would be useful to compare to simple estimates of sputtering and penetration. More accurate impurity profiles will also give more accurate radiated power profiles, which will be important for understanding the thermal transport. Thermal transport is of particular interest given the predictions of reduced edge losses, hotter edge temperatures, and improved confinement with low-recycling, and the observation here of flat temperature profiles.

7.4.2 Analysis of other LTX experiments and other physics topics

As described earlier, beyond the value and novelty of the improved physics understanding, this work sets a clear path for future efforts. Experiments under a wide variety of conditions were performed, and additional data from other diagnostics were collected. The analysis framework assembled in this work can be used to incorporate these additional diagnostics and study these additional experiments, and can be further expanded for different kinds of analyses.

LTX has been operated in a wide variety of conditions, and the framework developed in this work will be a valuable tool for understanding these experiments – some of them going back several years. Experiments have been performed with shell temperatures ranging from room temperature to ∼270 °C, including with repeated shots as the temperature is scanned over a wide range, increasing and decreasing, and over a narrow range just above and below the melting point of lithium. Studying these experiments, especially with the new framework, will give insight into the behavior of impurities as the temperature of the lithium coatings changes. This will be valuable for future experiments on LTX and other devices where the effects of liquid Li are important.

Beyond changes in temperature, the surface conditions also varied as experiments were conducted with coatings of various thickness and age. Evaporation techniques and procedures evolved, coatings were deposited on top of previous coatings, and lithium re-evaporated from shells kept hot for long periods of time. The coated shells sat in base vacuum for various amounts of time before experiments, and with differing vacuum conditions including pump oil and air leaks, glow discharge cleaning, and vessel bakeouts. Again, understanding impurities in these conditions will be important for the operation of LTX and future devices.

Finally, experiments were performed over a wide variety of plasma conditions, using different programming for coil currents and fueling (including operation with D instead of H), and achieving different plasma current, stored energy, and density. This analysis framework will be useful for understanding how impurity transport changes as the plasma conditions change. While MAPP was no longer installed at LTX for the experiments discussed in this work, it will also be useful to correlate surface measurements to core impurity measurements made under various conditions when both were available.

This framework also creates uniform data structures useful for constructing databases that can be used for data mining and finding trends as various external parameters are varied. They may also be useful to create a simple plasma model that can estimate temperature and density profiles in shots without sufficient TS data.

7.4.3   Future LTX diagnostics

Beyond a framework and data set for analyzing past LTX experiments, this work informs choices for future LTX work. The fundamental importance of the Thomson scattering measurements motivates upgrades to the diagnostic. A new camera has been purchased which can acquire a background frame microseconds before the laser fires, which will greatly reduce fitting issues due to light emission from the plasma. Rather than simply replacing the current camera, it may be worthwhile to add a second spectrometer and increase the number of sightlines measured. Adjustments to the optics in the current spectrometer may also improve its performance. LTX also has polychromators meant for the edge channels that will finally come online and further enhance the system.

A new visible spectrometer has been acquired that can measure lines in the UV, visible, and IR, and has gratings of different dispersion optimized for either wide surveying or finer resolution for temperature and velocity measurements. Spectroscopy

will be fundamentally different, with the addition of a neutral beam making true CHERS possible, and new viewing optics will need to be designed. The work done here underscores the need to extend views past the LCFS, and so re-entrant optics may be necessary. A new grating for the Holospec may be desirable, perhaps covering the same Li III / C III wavelength range used by the HAL spectrometer, or perhaps optimized for a charge exchange line such as C VI.

Additional diagnostics planned for LTX and informed by this work are a time resolved LoWEUS, using a faster camera to read multiple EUV spectra per shot, as well as a re-entrant bolometer (and Lyman-alpha) array, to directly measure radiated power profiles (and recycling). Another upgrade worth considering would be to give the Phantom camera a wider view of the plasma, perhaps with an re-entrant view and a fiber bundle, and/or a filter wheel to easily switch between high-speed measurements of recycling, impurity sources, and core emission.

These new and improved diagnostics can be readily incorporated into the framework used in this work.

7.4.4   Future LTX experiments

Future experiments in the upgraded LTX can also build on the present work. The main upgrades to LTX will be doubling the ohmic capacitor bank and the toroidal field strength and adding a neutral beam. This will allow longer discharges with a true flattop and higher current, as well as additional heating, fueling, and torque from the beam. The framework used here will be valuable for studying transport in these new experiments, especially with the planned enhancements to the analysis and diagnostics. Neutral beam fueling will be important in studying the low-recycling regime. Upgrades are also planned for the high field side gas puffer, Li evaporation system, and vacuum conditioning.

Having a more comprehensive diagnostic set available from the beginning will not only help initial breakdown and discharge development, but allow better analysis of discharges during the commissioning stages on bare stainless walls and as Li is gradually introduced, giving better insight into the specific impacts of wall conditioning. Spectral surveys will be useful to find charge states not measured in the current analysis and rule out high Z impurities. Longer, steady state discharges will be useful with the analysis framework, and help determine if impurities accumulate with time. Perturbative impurity injections may also be useful, especially if hotter electrons lead to fully stripped impurities over most of the plasma volume, making the charge state profiles only dependent on the v/D ratio. Deliberate, controlled impurity doses to the Li coatings may even be of interest. Future measurements of surface conditions will also be important to connect to this powerful framework for study of core impurity (and other) transport.

Bibliography

[1] M.A Abdou, The APEX TEAM, A Ying, N Morley, K Gulec, S Smolentsev, M Kotschenreuther, S Malang, S Zinkle, T Rognlien, P Fogarty, B Nelson, R Nygren, K McCarthy, M.Z Youssef, N Ghoniem, D Sze, C Wong, M Sawan, H Khater, R Woolley, R Mattas, R Moir, S Sharafat, J Brooks, A Hassanein, D Petti, M Tillack, M Ulrickson, and T Uchimoto. On the exploration of innovative concepts for fusion chamber technology. *Fusion Engineering and Design*, 54(2):181–247, feb 2001.

[2] T. Abrams, M.A. Jaworski, M. Chen, E.A. Carter, R. Kaita, D.P. Stotler, G. De Temmerman, T.W. Morgan, M.A. van den Berg, and H.J. van der Meiden. Suppressed gross erosion of high-temperature lithium via rapid deuterium implantation. *Nuclear Fusion*, 56(1):016022, 2016.

[3] M.L. Apicella, G. Mazzitelli, V. Pericoli Ridolfini, V. Lazarev, A. Alekseyev, A. Vertkov, and R. Zagórski. First experiments with lithium limiter on FTU. *Journal of Nuclear Materials*, 363-365:1346–1351, jun 2007.

[4] M J Baldwin, R P Doerner, S C Luckhardt, and R W Conn. Deuterium retention in liquid lithium. *Nuclear Fusion*, 42(11):1318–1323, nov 2002.

[5] R. Behrisch and W. Eckstein, editors. *Sputtering by Particle Bombardment: Experiments and Computer Calculations from Threshold to MeV Energies*. Springer Berlin Heidelberg, 2007.

[6] Ronald E Bell. Inversion technique to obtain an emissivity profile from tangential line-integrated hard x-ray measurements. *Review of Scientific Instruments*, 66(1):558, 1995.

[7] Ronald E Bell. An inversion technique to obtain full poloidal velocity profiles in a tokamak plasma. *Review of Scientific Instruments*, 68(2):1273, 1997.

[8] Ronald E Bell. Exploiting a transmission grating spectrometer. *Review of Scientific Instruments*, 75(10):4158, 2004.

[9] Ronald E Bell. Development and operation of a high-throughput accurate-wavelength lens-based spectrometer. *Review of Scientific Instruments*, 85(11):11E404, nov 2014.

[10] Ronald E Bell and Filippo Scotti. High-throughput accurate-wavelength lens-based visible spectrometer. *Review of Scientific Instruments*, 81(10):10D731, oct 2010.

[11] L Berzak, A D Jones, R Kaita, T Kozub, N Logan, R Majeski, J E Menard, and L E Zakharov. Magnetic diagnostics for equilibrium reconstructions in the presence of nonaxisymmetric eddy current distributions in tokamaks (invited). *Review of scientific instruments*, 81(10):10E114, oct 2010.

[12] L Berzak, R Kaita, T Kozub, R Majeski, and L E Zakharov. Magnetic diagnostics for the lithium tokamak experiment. *Review of scientific instruments*, 79(10):10F116, oct 2008.

[13] Laura Florence Berzak. *Plasma Start-up in a Spherical Tokamak with Close-fitting Conducting Walls*. PhD thesis, Princeton University, 2010.

[14] James Bialek, Allen H. Boozer, M. E. Mauel, and G. A. Navratil. Modeling of active control of external magnetohydrodynamic instabilities. *Physics of Plasmas*, 8(5 II):2170–2180, 2001.

[15] T. M. Biewer, R. E. Bell, R. Feder, D. W. Johnson, and R. W. Palladino. Edge rotation and temperature diagnostic on the National Spherical Torus Experiment. *Review of Scientific Instruments*, 75(3):650, 2004.

[16] N Bretz, D Dimock, V Foote, D Johnson, D Long, and E Tolnas. Multichannel Thomson scattering apparatus. *Applied Optics*, 17(2):192–202, 1978.

[17] J. N. Brooks, J. P. Allain, R. Bastasz, R. Doerner, T. Evans, A. Hassanein, R. Kaita, S. Luckhardt, R. Maingi, R. Majeski, N. B. Morley, M. Narula, T. Rognlien, D. Ruzic, R. Stubbers, M. Ulrickson, C. P C Wong, D. Whyte, and A. Ying. Overview of the ALPS program. *Fusion Science and Technology*, 47(3):669–677, 2005.

[18] Yingjie Chen, Zhenwei Wu, Xiaoju Liu, Dongsheng Wang, Yanmin Duan, Wei Gao, Ling Zhang, Juan Huang, Zhen Sun, Yinxian Jie, and Junyu Zhao. Investigation of Z_eff and impurity behaviour in lithium coating experiments with full metallic first wall in HT-7 tokamak. *Plasma Physics and Controlled Fusion*, 57(2):025012, feb 2015.

[19] C. De Michelis and M. Mattioli. Soft-X-ray spectroscopic diagnostics of laboratory plasmas. *Nuclear Fusion*, 21(6):677–754, 1981.

[20] R Dux, A.G Peeters, A Gude, A Kallenbach, R Neu, and Asdex Upgrade Team. Z dependence of the core impurity transport in ASDEX Upgrade H mode discharges. *Nuclear Fusion*, 39(11):1509–1522, nov 1999.

[21] Ralph Dux. STRAHL User Manual. *IPP Report*, 2006.

117

[22] T E Evans, R a Moyer, P Thomas, J G Watkins, T H Osborne, J A Boedo, E J Doyle, M E Fenstermacher, K. Finken, R J Groebner, M Groth, J. Harris, R. La Haye, C J Lasnier, S. Masuzaki, N. Ohyabu, D. Pretty, T. L. Rhodes, H. Reimerdes, D L Rudakov, M J Schaffer, G. Wang, and L. Zeng. Suppression of Large Edge-Localized Modes in High-Confinement DIII-D Plasmas with a Stochastic Magnetic Boundary. *Phys. Rev. Lett.*, 92(23):235003, jun 2004.

[23] A R Field, P G Carolan, R J Akers, E R Arends, K Axon, R J Buttery, N J Conway, G F Counsell, G Cunningham, S J Fielding, M Gryaznevich, A Kirk, I P Lehane, B Lloyd, M A McGrath, H Meyer, C Ribeiro, A Sykes, A Tabasso, M R Tournianski, M Valovic, M J Walsh, H R Wilson, and the MAST and NBI Teams. H-mode plasmas in the MAST spherical tokamak. *Plasma Physics and Controlled Fusion*, 44(5A):A113–A121, may 2002.

[24] S. J. Fielding, J. Hugill, G. M. McCracken, J. W. M. Paul, R. Prentice, and P. E. Stott. High-density discharges with gettered torus walls in DITE. *Nuclear Fusion*, 17:1382–1385, 1977.

[25] C B Forest, G Greene, and M Ono. CDX-U two-dimensional scanning microwave system. *Review of Scientific Instruments*, 61(10), 1990.

[26] Tom Fredian, Josh Stillerman, Gabriele Manduchi, Giulio Flor, and Ken Klare. MDSplus.

[27] Jeffrey P Freidberg. *Plasma Physics and Fusion Energy*. Cambridge University Press, 2007.

[28] Bill Gates. More Energy.

[29] D A Gates and L Delgado-Aparicio. Origin of tokamak density limit scalings. *Physical review letters*, 108(16):165004, apr 2012.

[30] D. S. Gelles. Microstructural examination of several commercial ferritic alloys irradiated to high fluence. *Journal of Nuclear Materials*, 104(C):975–979, 1981.

[31] R J Goldston, R Myers, and J Schwartz. The lithium vapor box divertor. *Physica Scripta*, T167:014017, feb 2016.

[32] Erik Michael Granstedt. *The Low-Recycling Lithium Boundary and Implications for Plasma Transport*. PhD thesis, Princeton University, 2013.

[33] T K Gray, T M Biewer, D P Boyle, E M Granstedt, R Kaita, R. Maingi, and R. P. Majeski. Spectral emission measurements of lithium on the lithium tokamak experiment. *Review of Scientific Instruments*, 83(10):10D537, 2012.

[34] C M Greenfield, K H Burrell, J C DeBoo, E J Doyle, B. W. Stallard, E. J. Synakowski, C. Fenzi, P Gohil, R J Groebner, L L Lao, M. a. Makowski, G R Mckee, R a Moyer, C. L. Rettig, T. L. Rhodes, R. I. Pinsker, G. M. Staebler, and W P West. Quiescent Double Barrier Regime in the DIII-D Tokamak. *Phys. Rev. Lett.*, 86(20):4544–4547, may 2001.

[35] Chris J Hansen, T. Benedett, A. Hossack, T. Jarboe, J. Levesque, and J. Schmitt. MHD Simulations of Plasma Dynamics in Devices with Non-Axisymmetric Boundaries. In *Exploratory Plasma and Fusion Research Workshop*, Auburn, AL, 2016.

[36] Christopher James Hansen. *MHD Modeling in Complex 3D Geometries: Towards Predictive Simulation of SIHI Current Drive*. PhD thesis, University of Washington, 2014.

[37] Zachary S Hartwig and Yuri A Podpaly. *Magnetic Fusion Energy Formulary*. Massachusetts Institute of Technology, Cambridge, MA, november edition, 2011.

[38] R. J. Hawryluk. An Empirical Approach to Tokamak Transport, 1981.

[39] S. P. Hirshman and D.J. Sigmar. Neoclassical transport of impurities in tokamak plasmas. *Nuclear Fusion*, 21(9):1079, 1981.

[40] W. A. Houlberg, K. C. Shaing, S. P. Hirshman, and M. C. Zarnstorff. Bootstrap current and neoclassical transport in tokamaks of arbitrary collisionality and aspect ratio. *Physics of Plasmas*, 4(9):3230, 1997.

[41] W A Houlberg and H Shirai. The NCLASS Module in the TOPICS Analysis Code. Technical report, JAERI-Naka, 2000.

[42] J D Huba. *NRL Plasma Formulary*. The Office of Naval Research, Washington, DC, 2007.

[43] Russell A. Hulse. Numerical Studies of Impurities in Fusion Plasmas. *Fusion Science and Technology*, 3(2):259–272, 1983.

[44] Ian H Hutchinson. *Principles of Plasma Diagnostics*. Cambridge University Press, 2002.

[45] Craig Michael Jacobson. *Electron transport in plasmas with lithium-coated plasma-facing components*. PhD thesis, Princeton University, 2014.

[46] M. A. Jaworski, J. Kallman, R. Kaita, H. Kugel, B. Leblanc, R. Marsala, and D. N. Ruzic. Biasing, acquisition, and interpretation of a dense Langmuir probe array in NSTX. *Review of Scientific Instruments*, 81(10):2014–2017, 2010.

[47] M A Jaworski, A Khodak, and R Kaita. Liquid-metal plasma-facing component research on the National Spherical Torus Experiment. *Plasma Physics and Controlled Fusion*, 55(12):124040, dec 2013.

[48] Michael Andrew Jaworski. *Thermoelectric magnetohydrodynamic and thermocapillary driven flows of liquid conductors in magnetic fields*. PhD thesis, University of Illinois at Urbana-Champaign, 2009.

[49] A Kallenbach, M Bernert, R Dux, L Casali, T Eich, L Giannone, A Herrmann, R McDermott, A Mlynek, H W Müller, F Reimold, J Schweinzer, M Sertoli, G Tardini, W Treutterer, E Viezzer, R Wenninger, and M Wischmeier. Impurity seeding for tokamak power exhaust: from present devices via ITER to DEMO. *Plasma Physics and Controlled Fusion*, 55(12):124041, 2013.

[50] S.M Kaye, F.M Levinton, D Stutman, K Tritz, H Yuh, M.G Bell, R.E Bell, C.W Domier, D Gates, W Horton, J Kim, B.P LeBlanc, N.C Luhmann, R Maingi, E Mazzucato, J.E Menard, D Mikkelsen, D Mueller, H Park, G Rewoldt, S.A Sabbagh, D.R Smith, and W Wang. Confinement and local transport in the National Spherical Torus Experiment (NSTX). *Nuclear Fusion*, 47(7):499–509, jul 2007.

[51] M. Kotschenreuther, P.M. Valanju, S.M. Mahajan, and E.A. Schneider. Fusion-Fission Transmutation Scheme-Efficient destruction of nuclear waste. *Fusion Engineering and Design*, 84(1):83–88, jan 2009.

[52] A. Kramida, Yu. Ralchenko, J. Reader, and NIST ASD Team. NIST Atomic Spectra Database (ver. 5.2), 2014.

[53] S I Krasheninnikov, L E Zakharov, and G V Pereverzev. On lithium walls and the performance of magnetic fusion devices. *Phys. Plasmas*, 10(5):1678, 2003.

[54] S. Kubota, X. V. Nguyen, W. A. Peebles, L. Zeng, E. J. Doyle, and A. L. Roquemore. Millimeter-wave reflectometry for electron density profile and fluctuation measurements on NSTX. *Review of Scientific Instruments*, 72(1):348, 2001.

[55] J. Laszlo and W. Eckstein. Sputtering and reflection from lithium, gallium and indium. *Journal of Nuclear Materials*, 184(1):22–29, 1991.

[56] B. LeBlanc, R. Bell, D. Dimock, P. A. Duperrex, J. Felt, R. Palladino, and E. Tolnas. The PBX-M Thomson scattering system. *Review of Scientific Instruments*, 61(10):2906, 1990.

[57] J K Lepson, P Beiersdorfer, J Clementson, M F Gu, M Bitter, L Roquemore, R Kaita, P G Cox, and A S Safronova. EUV spectroscopy on NSTX. *Journal of Physics B: Atomic, Molecular and Optical Physics*, 43(14):144018, jul 2010.

[58] M. Lucia, R. Kaita, R. Majeski, F. Bedoya, J. P. Allain, D. P. Boyle, J. C. Schmitt, and D. a. St. Onge. Development progress of the Materials Analysis and Particle Probe. *Review of Scientific Instruments*, 85(11):11D835, 2014.

[59] M. Lucia, R. Kaita, R. Majeski, F. Bedoya, J.P. Allain, T. Abrams, R.E. Bell, D.P. Boyle, M.a. Jaworski, and J.C. Schmitt. Dependence of LTX plasma performance on surface conditions as determined by in situ analysis of plasma facing components. *Journal of Nuclear Materials*, 463:907–910, 2015.

[60] Matthew James Lucia. *Material Surface Characteristics and Plasma Performance in the Lithium Tokamak Experiment.* PhD thesis, Princeton University, 2015.

[61] Daniel Patrick Lundberg. *Fueling studies on the lithium tokamak experiment.* PhD thesis, Princeton University, 2012.

[62] H. Lütjens, A. Bondeson, and A. Roy. Axisymmetric MHD equilibrium solver with bicubic Hermite elements. *Computer Physics Communications*, 69(2-3):287–298, 1992.

[63] H. Lütjens, A. Bondeson, and O. Sauter. The CHEASE code for toroidal MHD equilibria. *Computer Physics Communications*, 97(3):219–260, 1996.

[64] R Maingi, C S Chang, Seunghoe Ku, T Biewer, R Maqueda, M Bell, R Bell, C Bush, D Gates, S Kaye, H Kugel, B LeBlanc, J Menard, D Mueller, R Raman, S Sabbagh, V Soukhanovskii, and the NSTX Team. Effect of gas fuelling location on H-mode access in NSTX. *Plasma Physics and Controlled Fusion*, 46(5A):A305–A313, may 2004.

[65] R. Majeski. Liquid metal walls, lithium, and low recycling boundary conditions in tokamaks. *AIP Conference Proceedings*, 1237(2010):122–137, 2010.

[66] R. Majeski, T. Abrams, D. Boyle, E. Granstedt, J. Hare, C. M. Jacobson, R. Kaita, T. Kozub, B. LeBlanc, D. P. Lundberg, M. Lucia, E. Merino, J. Schmitt, D. Stotler, T. M. Biewer, J. M. Canik, T. K. Gray, R. Maingi, A. G. McLean, S. Kubota, W. A. Peebles, P. Beiersdorfer, J. H. T. Clementson, and K. Tritz. Particle control and plasma performance in the Lithium Tokamak eXperiment. *Physics of Plasmas*, 20(5):056103, 2013.

[67] R Majeski, L Berzak, T Gray, R Kaita, T Kozub, F M Levinton, D.P. Lundberg, J Manickam, G V Pereverzev, K. Snieckus, V A Soukhanovskii, J Spaleta, D Stotler, T Strickler, J Timberlake, J. Yoo, and L E Zakharov. Performance projections for the lithium tokamak experiment (LTX). *Nuclear Fusion*, 49(5):055014, may 2009.

[68] R Majeski, R. P. Doerner, T Gray, R Kaita, R Maingi, D K Mansfield, V A Soukhanovskii, J Spaleta, J Timberlake, and L E Zakharov. Enhanced Energy Confinement and Performance in a Low-Recycling Tokamak. *Physical Review Letters*, 97(7):075002, 2006.

[69] D K Mansfield, K W Hill, J D Strachan, M G Bell, S. D. Scott, R Budny, E S Marmar, J. A. Snipes, J L Terry, S. Batha, R E Bell, M Bitter, C E Bush, Z Chang, D. S. Darrow, D. Ernst, E D Fredrickson, B. Grek, H. W. Herrmann, A Janos, D. L. Jassby, F. C. Jobes, D W Johnson, L. C. Johnson, F M Levinton, D R Mikkelsen, D Mueller, D. K. Owens, H. K. Park, A. T. Ramsey, A L Roquemore, C H Skinner, T. N. Stevenson, B C Stratton, E. J. Synakowski, G Taylor, A. von Halle, S. von Goeler, K. L. Wong, and S. J.

Zweben. Enhancement of Tokamak Fusion Test Reactor performance by lithium conditioning. *Phys. Plasmas*, 3(5):1892, 1996.

[70] D K Mansfield, H W Kugel, R Maingi, M G Bell, R E Bell, R Kaita, J Kallman, S M Kaye, B P LeBlanc, and D Mueller. Transition to ELM-free improved H-mode by lithium deposition on NSTX graphite divertor surfaces. *Journal of Nuclear Materials*, 390-391:764–767, 2009.

[71] G F Matthews, M Beurskens, S Brezinsek, M Groth, E Joffrin, A Loving, M Kear, M-L Mayoral, R Neu, P Prior, V Riccardo, F Rimini, M Rubel, G Sips, E Villedieu, P de Vries, and M L Watkins. JET ITER-like walloverview and experimental programme. *Physica Scripta*, T145:014001, dec 2011.

[72] G. Mazzitelli, M.L. Apicella, D. Frigione, G. Maddaluno, M. Marinucci, C. Mazzotta, V. Pericoli Ridolfini, M. Romanelli, G. Szepesi, and O. Tudisco. FTU results with a liquid lithium limiter. *Nuclear Fusion*, 51(7):073006, 2011.

[73] G.M. McCracken and P.E. Stott. Plasma-surface interactions in tokamaks. *Nuclear Fusion*, 19:889–981, 2011.

[74] R. M. McDermott, B. Lipschultz, J. W. Hughes, P. J. Catto, A. E. Hubbard, I. H. Hutchinson, R. S. Granetz, M. Greenwald, B. Labombard, K. Marr, M. L. Reinke, J. E. Rice, and D. Whyte. Edge radial electric field structure and its connections to H-mode confinement in Alcator C-Mod plasmas. *Physics of Plasmas*, 16(5), 2009.

[75] J. Menard, B. Davis, and D. Mastrovito. Homepage for the LRDFIT code.

[76] Jonathan Edward Menard. *High-harmonic fast wave coupling and heating experiments in the CDX-U spherical tokamak*. PhD thesis, Princeton University, 1998.

[77] D. Mueller. The physics of tokamak start-up. *Physics of Plasmas*, 20(5):058101, 2013.

[78] T. Munsat and B. LeBlanc. A low-cost multichannel Thomson scattering system for CDX-U. *Review of Scientific Instruments*, 70(1):755, 1999.

[79] Tobin Leo Munsat. *Transient Transport Experiments in the CDX-U Spherical Torus*. PhD thesis, Princeton University, 2001.

[80] J. M. Munoz Burgos. Personal Communication.

[81] R A Pitts, A Kukushkin, A Loarte, A Martin, M Merola, C E Kessel, V Komarov, and M Shimada. Status and physics basis of the ITER divertor. *Physica Scripta*, T138:014001, dec 2009.

[82] M. Podestà, R.E. Bell, A. Diallo, B.P. LeBlanc, and F. Scotti. Measurements of core lithium concentration in a Li-conditioned tokamak with carbon walls. *Nuclear Fusion*, 52(3):033008, mar 2012.

[83] L. Porte, C. L. Rettig, W. a. Peebles, and X. Ngyuen. Design and operation of a low cost, reliable millimeter-wave interferometer. *Review of Scientific Instruments*, 70(1):1082, 1999.

[84] D E Post, R V Jensen, C B Tarter, W H Grasberger, and W A Lokke. Steady state radiative cooling rates for low-density high-temperature plasmas. Technical report, PPPL, jul 1977.

[85] Christian H. Reinsch. Smoothing by Spline Functions. *Numerische Mathematik*, 10:177–183, 1967.

[86] Wim Ruyten. Smear correction for frame transfer charge-coupled-device cameras. *Optics Letters*, 24(13):878–880, 1999.

[87] J C Schmitt, T Abrams, L R Baylor, L Berzak Hopkins, T Biewer, D Bohler, D Boyle, E Granstedt, T Gray, J Hare, C M Jacobson, M Jaworski, R Kaita, T Kozub, B Leblanc, D P Lundberg, M Lucia, R Maingi, R Majeski, E Merino, A Ryou, E Shi, J Squire, D Stotler, C E Thomas, K Tritz, and L Zakharov. Results and future plans of the Lithium Tokamak eXperiment (LTX). *Journal of Nuclear Materials*, 438:S1096–S1099, jan 2013.

[88] J. C. Schmitt, R. E. Bell, D. P. Boyle, B. Esposti, R. Kaita, T. Kozub, B. P. LeBlanc, M. Lucia, R. Maingi, R. Majeski, E. Merino, S. Punjabi-Vinoth, G. Tchilingurian, A. Capece, B. Koel, J. Roszell, T. M. Biewer, T. K. Gray, S. Kubota, P. Beiersdorfer, K. Widmann, and K. Tritz. High performance discharges in the Lithium Tokamak eXperiment with liquid lithium wallsa). *Physics of Plasmas*, 22(5):056112, may 2015.

[89] F. Scotti, V.A. Soukhanovskii, R.E. Bell, S. Gerhardt, W. Guttenfelder, S. Kaye, R. Andre, A. Diallo, R. Kaita, B.P. LeBlanc, M. Podesta, and the NSTX Team. Core Transport of Lithium and Carbon in ELM-free Discharges with Lithium Wall Conditioning in NSTX. *Nuclear Fusion*, 53(8):083001, aug 2013.

[90] Filippo Scotti. *Modifications of impurity transport and divertor sources by lithium wall conditioning in the National Spherical Torus Experiment.* PhD thesis, Princeton University, 2014.

[91] Filippo Scotti and Ronald E Bell. High accuracy wavelength calibration for a scanning visible spectrometer. *Review of Scientific Instruments*, 81(10):10D732, oct 2010.

[92] A.C. Selden. Simple analytic form of the relativistic Thomson scattering spectrum. *Physics Letters A*, 79(5):405–406, 1980.

[93] W. M. Solomon, P. B. Snyder, A. Bortolon, K. H. Burrell, A. M. Garofalo, B. A. Grierson, R. J. Groebner, A. Loarte, A. W. Leonard, O. Meneghini, R. Nazikian, T. H. Osborne, C. C. Petty, and F. Poli. Exploration of the Super

H-mode regime on DIII-D and potential advantages for burning plasma devices. *Physics of Plasmas*, 23(5):056105, may 2016.

[94] V A Soukhanovskii, M Finkenthal, H. W. Moos, D Stutman, T Munsat, B Jones, D. E. Hoffman, Robert Kaita, and R Majeski. Observation of neoclassical impurity transport in Ohmically heated plasmas of CDX-U low aspect ratio tokamak. *Plasma Physics and Controlled Fusion*, 44(11):2339–2355, nov 2002.

[95] V A Soukhanovskii, D Stutman, M Finkenthal, H. W. Moos, Robert Kaita, and R Majeski. Compact collimated vacuum ultraviolet diagnostics for localized impurity measurements in fusion boundary plasmas. *Review of Scientific Instruments*, 72(8):3270, 2001.

[96] Peter C Stangeby. *The Plasma Boundary of Magnetic Fusion Devices*. Institute of Physics Publishing, Bristol, 2000.

[97] T Strickler, R Majeski, R Kaita, and B P LeBlanc. The Thomson scattering system on the lithium tokamak experiment. *Review of Scientific Instruments*, 79(10):10E738, oct 2008.

[98] H. P. Summers. The ADAS User Manual, version 2.6, 2004.

[99] C. N. Taylor, B. Heim, S. Gonderman, J. P. Allain, Z. Yang, R. Kaita, A. L. Roquemore, C. H. Skinner, and R. A. Ellis. Materials analysis and particle probe: A compact diagnostic system for in situ analysis of plasma-facing components (invited). *Review of Scientific Instruments*, 83(10), 2012.

[100] Kathreen E Thome. *H-mode access and characteristics at near-unity aspect ratio on the pegasus toroidal experiment*. PhD thesis, The University of Wisconsin - Madison, 2016.

[101] J Titheridge. The real height analysis of ionograms: A generalized formulation. *Radio Science*, 23(5):831–849, 1988.

[102] K. Tritz, D. J. Clayton, D. Stutman, and M. Finkenthal. Compact diode-based multi-energy soft x-ray diagnostic for NSTX. *Review of Scientific Instruments*, 83(10):1–4, 2012.

[103] Kevin Tritz, Ronald E Bell, Peter Beiersdorfer, Dennis Boyle, Joel Clementson, Michael Finkenthal, Robert Kaita, Tom Kozub, Shigeyuki Kubota, Matthew Lucia, Richard Majeski, Enrique Merino, John Schmitt, and Dan Stutman. VUV/XUV measurements of impurity emission in plasmas with liquid lithium surfaces on LTX. *Plasma Physics and Controlled Fusion*, 56:125014, 2014.

[104] Peter van Hoof. Atomic Line List v2.04.

[105] K.W. Wenzel and D.J. Sigmar. Neoclassical analysis of impurity transport following transition to improved particle confinement. *Nuclear Fusion*, 30(6):1117–1127, 1990.

[106] J. Wesson. *Tokamaks*. Clarendon Press, 3 edition, 2004.

[107] K Widmann, P Beiersdorfer, E W Magee, D P Boyle, R Kaita, and R Majeski. High-resolution grazing-incidence grating spectrometer for temperature measurements of low-Z ions emitting in the 100-300 Å spectral band. *Review of Scientific Instruments*, 85(11):11D630, nov 2014.

[108] L E Zakharov, N Gorelenkov, R White, S I Krasheninnikov, and G V Pereverzev. Ignited spherical tokamaks and plasma regimes with LiWalls. *Fusion Engineering and Design*, 72(1-3):149–168, nov 2004.

[109] H Zohm. Edge localized modes (ELMs). *Plasma Physics and Controlled Fusion*, 38(2):105–128, 1996.